On the Process–Structure–Property Relationships of Poly(Lactic Acid)-Based Nanocomposites

Vom Fachbereich Maschinenbau und Verfahrenstechnik

der Technischen Universität Kaiserslautern

zur Verleihung des akademischen Grades

Doktor-Ingenieur (Dr.-Ing.)

genehmigte

Dissertation

von

Frau

M.Sc. Praphakorn Saiprasit

aus Saraburi, Thailand

Datum der mündlichen Prüfung: 28.10.2021

Dekan: Prof. Dr.-Ing. Tilmann Beck

Prüfungsvorsitzender: Prof. Dr.-Ing. Eberhard Kerscher

1. Berichterstatter: Prof. Dr.-Ing. Alois K. Schlarb

2. Berichterstatter: Prof. Dr.-Ing. Christian Bonten

D 386

Acknowledgement

Kaiserslautern, October 2021   Praphakorn Saiprasit

Table of Contents

Abstract

The concept of bioplastics as sustainable and environmentally friendly materials has become increasingly interesting in both academia and industry. Consequently, many researchers have made great effort in developing bioplastic materials. As new challenging materials, there is still a lack of in-depth understanding of the process–structure–property relationships, especially in multi-phase component nanocomposites. In this thesis, the bioplastics – poly(lactic acid) (PLA)/polybutylene adipate-co-terephthalate (PBAT)-based nanocomposites containing nano-SiO_2 particles – are examined. Various processing procedures are carried out to investigate their effect on the structure–property relationships of the nanocomposites. The selective location of the nanoparticles is observed with respect to the processing sequence. The differences in nanoparticle location have a tremendous impact on the rheological, thermal, and mechanical properties of the PLA/PBAT-based nanocomposites. Furthermore, a numerical simulation of the temperature distribution during the injection molding process is applied to corroborate the effect of the injection molding conditions on the final properties. By understanding the working mechanism and behavior of the phase morphology of the studied nanocomposites, the desirable properties can be optimized and adjusted for proper applications.

Kurzfassung

Das Interesse an Biokunststoffen nimmt in Wissenschaft und Industrie stetig zu, da diese eine nachhaltige und umweltfreundliche Werkstoffgruppe darstellen. Die Entwicklung von Biokunststoffen wird daher mit großem Forschungsaufwand vorangetrieben. Eine Herausforderung stellt dabei der lückenhafte Kenntnisstand über die Prozess–Struktur–Eigenschaftsbeziehungen dieser Materialien dar, insbesondere, wenn sie als Komponente in mehrphasigen Nanokompositen verwendet werden. Die vorliegende Arbeit befasst sich mit derartigen Nanokompositen, bestehend aus Polylactid (polylactic acid, PLA), Polybutylenadipat-terephthalat (PBAT) und SiO_2-Nanopartikeln. Die Werkstoffe wurden mit mehreren unterschiedlichen Verfahren verarbeitet, um prozessbedingte Einflüsse auf Struktur und Eigenschaften identifizieren zu können. In Abhängigkeit von der Prozessführung wurde eine selektive räumliche Verteilung der Nanopartikel beobachtet. Diese hat wiederum erhebliche Auswirkungen auf die rheologischen, thermischen und mechanischen Eigenschaften der PLA/PBAT-Nanokomposite. Ergänzend wurde eine numerische Simulation der Temperaturverteilung während des Spritzgießprozesses durchgeführt, um den Einfluss der Spritzgießparameter auf die Formteileigenschaften zu ergründen. Das so gewonnene tiefgreifende Verständnis für die Entstehung und die Auswirkungen der Phasenmorphologie der untersuchten Nanokomposite ermöglicht es, Werkstoffeigenschaften gezielt und anwendungsgerecht zu optimieren.

Table of Figures

Table of Tables

List of Abbreviations and Symbols

Abbreviations

CH_2I_2	Diiodomethane
CNCs	Cellulose nanocrystals
CNTs	Carbon nanotubes
CO_2	Carbon dioxide
DI water	Deionized water
DSC	Differential scanning calorimetry
EVA	Poly(ethylene-co-vinyl acetate)
Flash DSC	Fast scanning or Flash differential scanning calorimetry
FIB	Focused ion beam
Gn.	Granular sample
HDT	Heat deflection temperature
HMDS	Hexamethyldisilazane
H_2O	Dihydrogen monoxide or water
ID	Injection direction
Ir	Iridium
LCST	Lower critical solution temperature
MB	Masterbatch
MMT	Montmorillonite clay
MWCNTs	Multi-walled carbon nanotubes
Nano-SiO$_2$	Silicon dioxide or silica nanoparticles
N_2	Nitrogen
OMMT	Organically modified montmorillonite
PA	Polyamide

PA6	Polyamide 6
PA11	Polyamide 11
PBAF	Poly(butylene adipate-co-furandicarboxylate)
PBAT	Poly(butylene adipate-co-terephthalate)
PBS	Poly(butylene succinate)
PCL	Polycaprolactone
PE	Poylyethylene
PEF	Poly(ethylene furanoate)
PET	Poly(ethylene terephthalate)
PHA	Polyhydroxyalkanoate
PIB	Polyisobutylene
PLA	Poly(lactic acid)
PLLA	Poly(L-lactic acid)
PDLA	Poly(D-lactic acid)
PLOM	Polarized light optical microscope
PP	Polypropylene
PP-g-MA	Polypropylene-grafted maleic anhydride
PTT	Poly(trimethylene terephthalate)
PTFE	Polytetrafluoroethylene
PS	Polystyrene
SAN	Poly(styrene-co-acrylonitrile)
SEM	Scanning electron microscope
Si-OH	Silanol group
TD	Transverse direction
TiO_2	Titanium dioxide
TPU	Thermoplastic polyurethane
TPS	Thermoplastic starch

UCST   Upper critical solution temperature

vol.%   Volume percent

wt.%   Weight percent

Symbols

$A_{i,PB}$ $[nm^2]$ Area i of PBAT droplet

A_{PB} $[nm^2]$ Area of cross-sectional PBAT droplet

A_T $[nm^2]$ Total observed area

$A_{Si,i}$ $[\%]$ Area proportion of nano-SiO_2 located in polymer i to the total observed area of polymer i

a $[nm]$ Radius of a spherical particle

$a_{i,j}$ $[nm^2]$ Area i of agglomerate nano-SiO_2 located in polymer j

a_n $[kJ/m^2]$ U-notched impact strength

b $[mm]$ Sample width

C $[collision/s]$ Frequency of collisions

Ca $[-]$ Capillary number

Ca_{cr} $[-]$ Critical capillary number

D_n $[\mu m, nm]$ Number average diameter

D_v $[\mu m, nm]$ Volume average diameter

D_0 $[nm^2/s]$ Diffusion coefficient of a spherical particle

D_i $[\mu m, nm]$ Equivalent diameter

d $[-]$ Droplet size dispersity

d $[\mu m, nm]$ Average diameter of the rubber polymer

d_γ/dT $[mJ/m^2K]$ Temperature coefficient

$\dot{\varepsilon}$ $[s^{-1}]$ Strain rate

F_{max} $[N]$ Maximum separating force

f $[-]$ Mass fraction

G' $[Pa]$ Storage modulus

G''	[Pa]	Loss modulus
G^*	[Pa]	Complex modulus
ΔG_m	[J/mol]	Gibbs free energy
h	[mm]	Sample height
ΔH_{cc}	[J/g]	Cold crystallization enthalpy
ΔH_c	[J/g]	Crystallization enthalpy
ΔH_m	[J/g]	Melting enthalpy
	[J/mol]	Mixing enthalpy
ΔH_m^o	[J/g]	Heat of fusion of 100% crystallized polymer
k	[−]	Geometric constant
	[min^{-1}]	Overall crystallization rate constant
k_B	[J/K]	Boltzmann's constant
M_w	[kDa]	Molecular weight
n	[−]	Avrami index
n_d	[−]	Dimensionality index
n_n	[−]	Time dependence of nucleation
η	[Pa·s]	Viscosity
η_m	[Pa·s]	Viscosity of matrix
η_d	[Pa·s]	Viscosity of dispersed phase
η_r	[−]	Viscosity ratio
η_s	[Pa·s]	Liquid viscosity
η^*	[Pa·s]	Complex viscosity
θ	[°]	Contact angle
ϕ	[−]	Volume fraction
ϕ_r	[−]	Volume fraction of rubber polymer
P	[Pa]	Pressure
Pe	[−]	Peclet number

Q	[W/g]	Heat flow
Q_t	[W/g]	Heat flow generated at time t
Q_∞	[W/g]	Heat flow generated at an infinite time t_∞ or a complete crystallization time
R	[μm]	Radius of undeformed droplet
Ra	[μm]	Surface roughness
$\dot{\gamma}$	[s^{-1}]	Shear rate
γ_{ij}	[mJ/m^2]	Interfacial energy/tension between component i and j
γ_i	[mJ/m^2]	Surface energy/tension of component i
γ_i^d	[mJ/m^2]	Surface energy/tension of component i with dispersive contribution
γ_i^p	[mJ/m^2]	Surface energy/tension of component i with polar contribution
ΔS_m	[J/K mol]	Mixing entropy
T	[K, ^{o}C]	Temperature
T_{cc}	[^{o}C]	Cold crystallization temperature
T_c	[^{o}C]	Crystallization temperature
T_g	[^{o}C]	Glass transition temperature
$T_{\sim g}$	[^{o}C]	Measured temperature at about glass transition temperature
T_m	[^{o}C]	Melting temperature
T_0	[^{o}C]	Initial temperature
t	[min, s]	Time
t_D	[s]	Required time for a particle to diffuse as much as its radius
$t_{\sim g}$	[s]	Cooling time to reach glass transition temperature
$t_{1/2}$	[min]	Half-time of crystallization
$t_{1/2,exp.}$	[min]	Half-time of crystallization obtained from experiment
$t_{1/2,cal.}$	[min]	Half-time of crystallization obtained from calculation

τ	[nm]	Interparticle distance or matrix ligament thickness
τ_c	[nm]	Critical interparticle distance
$\tan \delta$	[−]	Loss or damping factor
V	[cm^3]	Molecular volume
υ_r	[cm^3]	Interacting segment volume
W	[J]	Impact energy absorbed by sample
ω	[rad/s]	Angular frequency
ω	[−]	Wetting parameter
$x_{50,2}$	[nm]	Average agglomerate size
X_c	[%]	Degree of crystallinity
X_t	[−]	Relative crystallinity
χ_{12}	[−]	Flory-Huggins interaction parameter
μ	[J/mol]	Chemical potential
δ	[°]	Phase angle
δ	[(J/cm^3)$^{1/2}$]	Solubility parameter

1 Introduction

1.1 Background

With a steady increase in plastic waste pollution and CO_2 emission, bioplastics have emerged as a new challenging material for substituting or reducing the dependence on conventional or petroleum-based plastics. Bioplastics can represent not only sustainable but also eco-friendly materials. As a result, the research and development of bioplastic materials are growing in several fields of application (i.e., food packaging, medical applications, agriculture [1–4]). During the last several decades, poly(lactic acid) (PLA) has become one of the most widely developed commercial biopolymers. It serves as a bio-based, biodegradable, and biocompatible polymer [5]. However, PLA exhibits inherent brittleness and slow crystallization rates, which limit its use in many applications. PLA modifications, therefore, play an important role in extending the use of PLA polymers. Many strategies have been proposed for improving the properties of PLA, such as copolymerization, polymer blend, and filler incorporation [5–10].

The polymer blend is a practical and economical approach to improve the material properties by combining two or more polymers with the desired properties and creating a new material. Furthermore, this approach can reduce the complexity and expense of modifying the material properties. As to the fact that PLA suffers from its brittleness, blending PLA with a flexible polymer is a considerable choice to obtain synergetic properties. Several flexible biopolymers have been blended with PLA, for example, poly-caprolactone (PCL), poly(butylene succinate) (PBS), and poly(butylene adipate-co-terephthalate) (PBAT) [5,6,8]. The blending of PLA with a flexible biopolymer promises an enhancement in ductility. However, the stiffness and strength of the blend are diminished.

The incorporation of fillers, especially in the nano-scale, has been introduced in a polymer blend not only for achieving a balance between stiffness and toughness but also for stabilizing the phase morphology in the blend system [5,11–15]. Generally, the nanofillers can be classified into three categories in terms of their geometries: (i) sheet-like nanofillers (1D, i.e., nanoclays, graphene sheets), (ii) fiber or tube nanofillers (2D, i.e., carbon nanotubes (CNTs), cellulose nanocrystals (CNCs)), and (iii) spherical nanofillers (3D, i.e., silicon dioxide (SiO_2)) [13,16]. As the nanofillers have a diameter with at least one dimension in the range of 1–100 nm, that produces an ultra-large interfacial area per unit

volume, the superior performance of the polymer blend nanocomposites can consequently be achieved at very low nanofiller loadings [11,13].

Furthermore, most of the polymer blends have phase-separated morphology. Hence, the nanofillers always have their preferential location in one phase of the polymers and/or at the interface in the immiscible blends [5,14,15,17]. The driving forces in selecting the location of the nanofillers can be attributed to either their thermodynamic effects (affinity of the nanofillers) or kinetic aspects, such as processing sequence, processing time, and viscosity ratio [18–20]. As a result, the nanofillers location can be an important feature to control the final performance (i.e., physical and mechanical properties) of the polymer materials.

1.2   Objective of the Study

As stated above, it is of great interest to investigate how the processing procedures affect the structures and properties of the bioplastic-based nanocomposites. Therefore, the main objectives of the work are the following:

- To prepare a novel bioplastic-based nanocomposite consisting of PLA as a polymer matrix, PBAT as a dispersed polymer, and nano-SiO_2 as dispersed nanofillers with various processing procedures using a co-rotating twin-screw extruder and an injection molding machine.
- To characterize the influence of the processing procedures on the morphology, rheological, thermal, and mechanical properties of the studied nanocomposites.
- To understand the in-depth mechanism and behavior of how the preferential location of nanofillers can behave differently in the different process and material conditions.
- To investigate the role of the dispersed nanofillers and polymer size and distribution on the rheological, thermal, and mechanical properties.
- To evaluate the relationships between the process–structure–property of the obtained nanocomposites.
- To analyze the effect of nanofiller loading on the morphology, thermal, and mechanical properties of the PLA/PBAT-based nanocomposites.

2   State of the Art

2.1   An Overview of Plastics

It is well known that most of the basic products in our modern life are produced from plastics, for instance, food packaging, automotive parts, and medical devices. They play an essential role in plastic products for preserving, protecting, delivering, etc. [21]. Moreover, due to their versatile performance and lightweight design, many researchers have attempted to replace materials like metal with filler reinforced plastics in many applications [22,23]. Consequently, plastic consumption has increased around the world. Based on the statistical data, global plastic production rose from 2 million tonnes in 1950 to 380 million tonnes in 2015, as shown in Figure 2.1 [24]. As a result, plastic pollution has also increased tremendously and has led to a serious environmental concern. In addition, plastics are mainly made from petroleum-based polymers that are produced from crude oil and natural gas. Therefore, plastic production and marketing are strongly dependent on oil and gas resources, which are declining from nature [2,25].
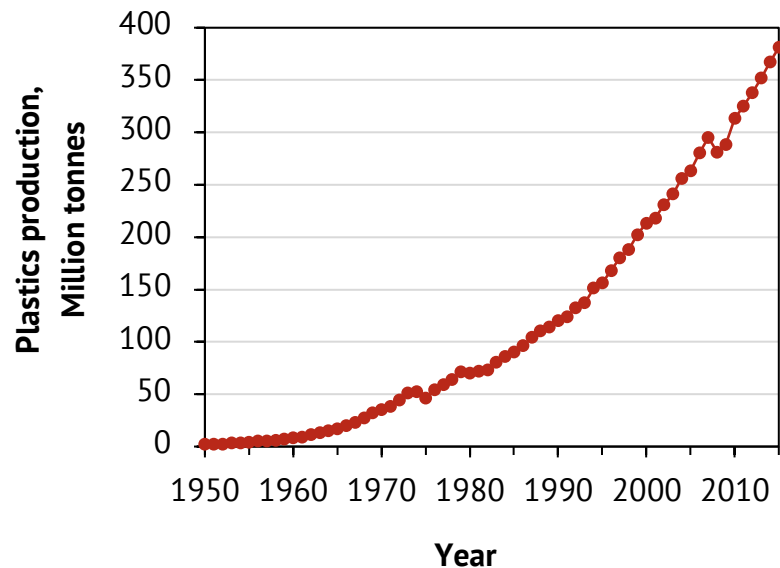
Figure 2.1:   Global plastic production (resins and fibers) from 1950 to 2015 (adapted and modified from [24]).

2.2   Bioplastics

As awareness of environmental sustainability has increased, bioplastics have become more attractive in plastic industries in the past decade [6,21,26]. They reduce not only the dependence on limited crude oil and natural gas but also the greenhouse effect or CO_2 emission and plastic waste pollution [25,27]. Therefore, bioplastics are inspiring materials for replacing conventional or petroleum-based plastics in their corresponding applications. According to European Bioplastics, the term "bioplastics" can be separated into three different types [28]. Figure 2.2 illustrates the bioplastics and conventional plastics coordinate system. The figure shows four possible groups of plastics or polymers:

Group 1. Bio-based and biodegradable polymers (i.e., poly(lactic acid) (PLA), polyhydroxyalkanoate (PHA));

Group 2. Bio-based but non-biodegradable polymers (i.e., bio-based polyethylene (PE), bio-based poly(ethylene terephthalate) (PET));

Group 3. Petroleum-based but biodegradable polymers (i.e., poly(butylene adipate-co-terephthalate) (PBAT), polycaprolactone (PCL));

Group 4. Petroleum-based and non-biodegradable polymers (i.e., PE, polypropylene (PP)).
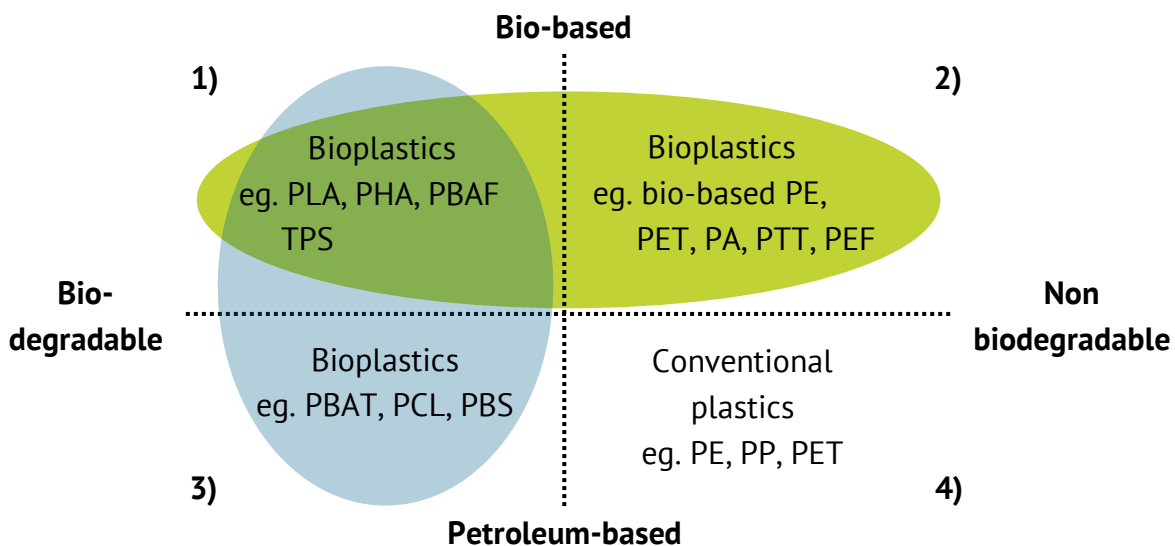
Figure 2.2:   Schematic representation of the bioplastics and conventional plastics coordinate system (adapted and modified from [28]).

Plastics are sorted either by the natural resources or the ability to biodegrade the polymer. Bio-based polymers are made from renewable resources, such as corn starch, soybean protein, and cellulose, while petroleum-based polymers, as mentioned before, are produced from crude oil and natural gas [6,29,30]. Biodegradable polymers are materials that can be re-transformed to nature [30]. The plastic groups 1−3 can be defined as "bioplastics", whereas group 4 is called "conventional plastics". In addition, bio-based polymers do not necessarily mean biodegradable and vice versa.

In 2019, bioplastics comprised only about 2.11 million tonnes of the 380 million tonnes of plastic produced globally, as shown in Figures 2.1 and 2.3. However, with the growing environmental awareness, bioplastics have been increasingly in demand in the plastic industry [31]. To serve more specific applications as well as expanding the bioplastic market, the research and development of bioplastics or biopolymers has risen continuously [6,32]. In this thesis, particular attention is devoted to bio-based and biodegradable polymers in groups 1 and 3, as listed in Figure 2.2.
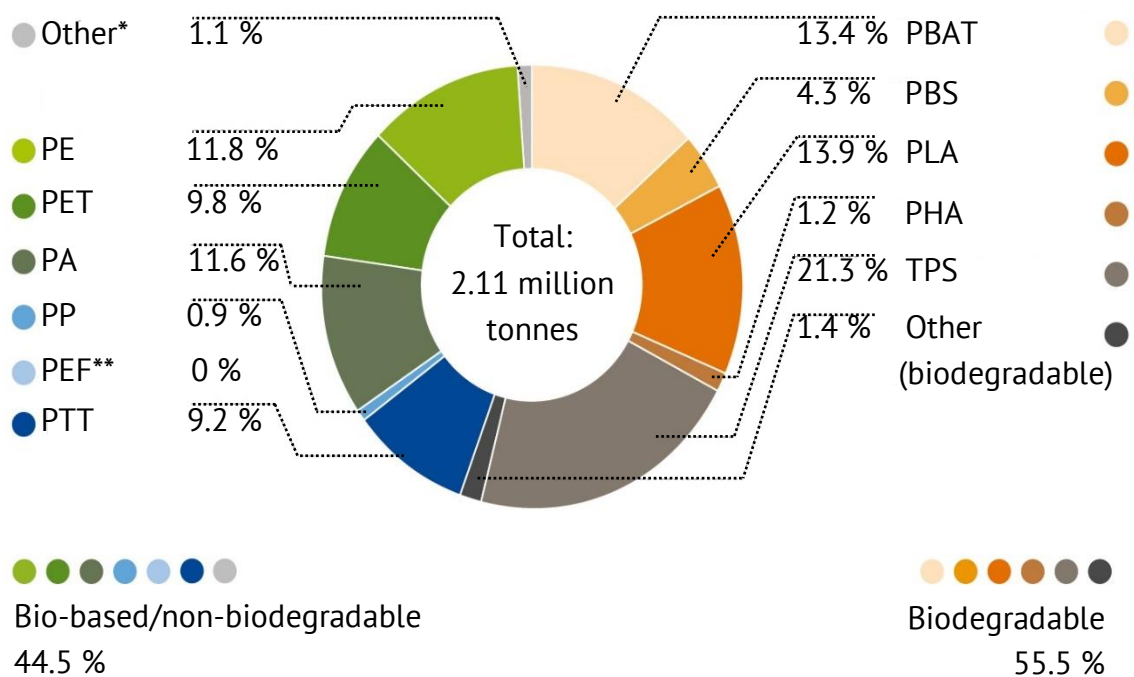
Figure 2.3:   Global production capacities of bioplastics in 2019 (by material type) (adapted and modified from [31]).

2.2.1   Poly(Lactic Acid)

Among bio-based and biodegradable polymers, PLA is one of the most promising candidates due to its 100 % renewable resources, mechanical performance, and large scale production. As a consequence, the research studies and reports about PLA have risen dramatically in the past few decades [2,6,7,33,34].

PLA is a bio-based and biodegradable aliphatic polyester that is produced from corn sugar, potato, and sugar cane. Figures 2.4 and 2.5 illustrate the production steps starting from the raw materials to the PLA resin. Dextrose is extracted from the raw materials and converted to lactic acid via fermentation. Afterward, PLA is industrially produced by polycondensation of lactic acid and/or ring-opening polymerization of lactide. Typically, the lactic acid monomer exists as two stereoisomers: L- and D-lactic acid. PLA with more than 93 % L-lactic acid is a semi-crystalline polymer [6].

Synthesis of lactic acid (monomer)
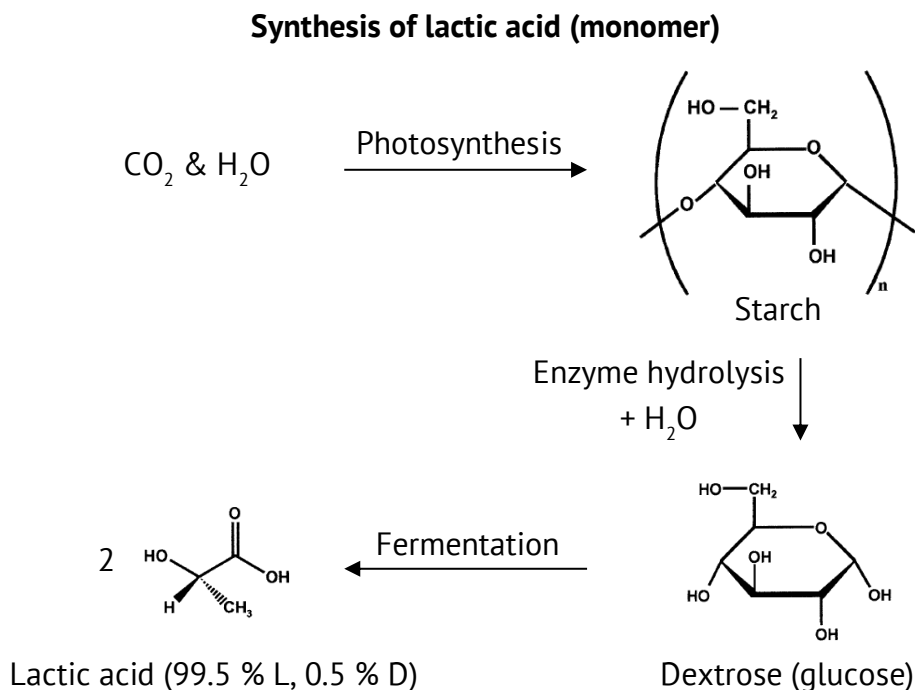
Figure 2.4:   PLA production: Synthesis of lactic acid (monomer) (adapted and modified from [6,35]).

PLA exhibits favorable transparency, biocompatibility, high strength, and high stiffness when compared to the petroleum-based commodity polymers such as PP, PET, and polystyrene (PS), as seen in Table 2.1. Various types of melting processes are generally used to produce PLA products, for instance, extrusion, injection molding, blow molding, cast

film extrusion, fiber spinning, and thermoforming [2,6]. For the reasons stated, PLA has been used in various fields of application, such as textiles, packaging, plasticulture, and medical devices. Table 2.2 shows selected examples of products made from PLA in the market.

Synthesis of PLA polymer
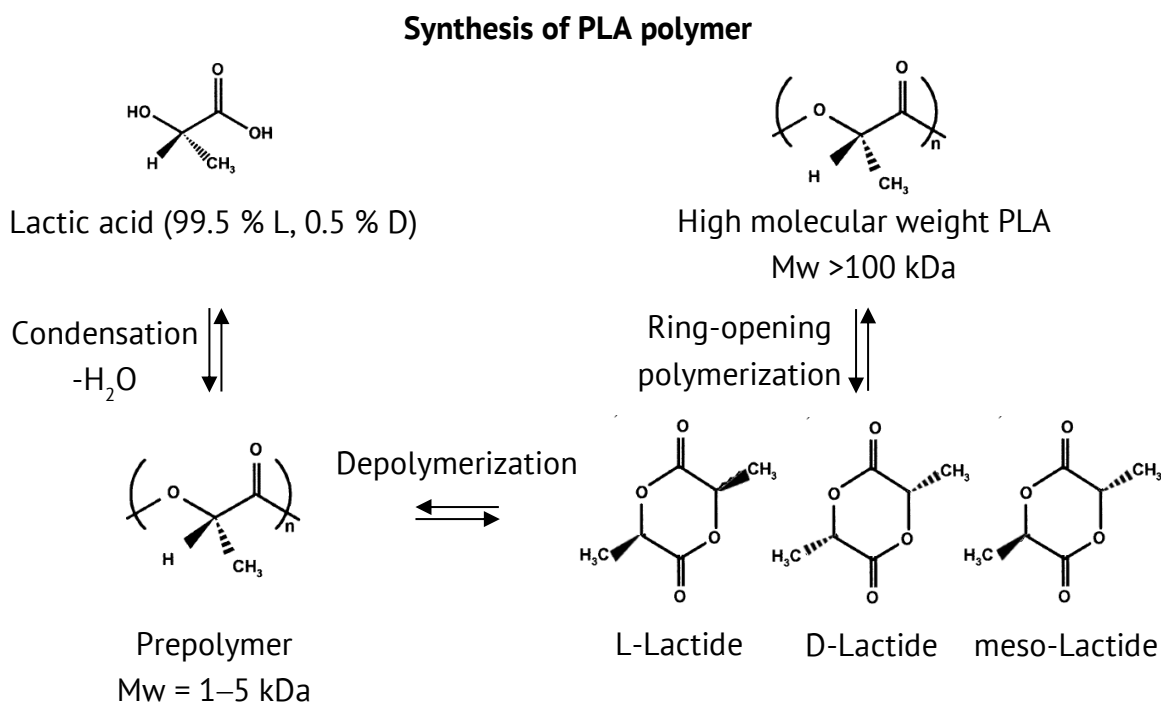
Figure 2.5:   PLA production: Synthesis of PLA polymer (adapted and modified from [2,6,35]).

Table 2.1:   Comparative mechanical properties of PLA, PP, PET, and PS

Properties	PLA	PP	PET	PS
Tensile strength (MPa)	73.6	25–40	55–80	30–55
Young's modulus (GPa)	3.7	1.3–1.8	2.1–3.1	3.1–3.3
Elongation at break (%)	4.8	>50	50–130	1.5–7.0

PET and PS characteristic data are adapted from [7,36].

Besides the above advantages, PLA has suffered from shortcomings related to its inherent brittleness, slow crystallization rate, low melt strength, and low service temperature or heat deflection temperature (HDT) [5,6,37]. To overcome these limitations, the properties of PLA can be enhanced through several strategies such as copolymerization, polymer

blending, and filler incorporation [5–10]. In this work, particular attention is given to the polymer blending and filler incorporation.

Table 2.2: Selected examples of products made from PLA in the market

Trademark/Commercialized brand	Applications	Ref.
PURALACT®, Corbion, Netherlands	Serviceware	[38]
Polenghi LAS, Italy	Lemon juice bottle	[39]
Activia®, Danone, Germany	Yogurt cup	[40]
PLA mulch film, Xinchuang Bio, China	Mulch film	[41]
XD collection, XINDAO®, China	Coffee mug/tumbler	[42]
Bio interfix screw, Tulpar medical solutions, Turkey	Interference screw	[43]

2.2.2 Poly(Lactic Acid)-Based Blends

Despite its good potential to replace petroleum-based polymers, PLA has limitations (especially low toughness) that restrict its usage in many applications. Tailoring the PLA properties by blending with a flexible and biodegradable polymer is, therefore, a practical approach in the industry because it is inexpensive and no chemicals are involved. Many research studies have extensively reported the blending of PLA with polycaprolactone (PCL), poly(butylene succinate) (PBS), poly(butylene adipate-co-terephthalate) (PBAT), etc. [5,6,8]. In principle, the mentioned flexible polymers exhibit a rubbery behavior, which has a glass transition temperature (T_g) of 20 °C below the service temperature [6].

Jiang et al. [44] reported that the addition of a small ratio of PBAT (5–20 wt.%) dramatically improves the toughness of PLA. However, the deterioration of the stiffness and tensile strength was observed owing to the flexibility of the added polymer. A similar behavior is also reported for other flexible polymers in the literature [45,46]. To optimize the mechanical properties of the PLA-based blends, an inclusion of nanofillers has been proposed, which will be discussed in the next section.

2.2.3 Poly(Lactic Acid)-Based Blend Nanocomposites

The incorporation of nanofillers has been introduced to the PLA-based blends for optimizing the final properties [5,14,15,18,47]. Typically, PLA blended with other biodegradable polymers are immiscible due to the difference in interfacial energy between the polymer pair [18]. As a consequence, the added nanofillers are most likely to have a preferential location and, thereby, play an important role in controlling the properties of the nanocomposites.

Various types of nanofillers have been reported for incorporating in the PLA-based blends, for instance, nanoclays [14,47–49], carbon nanotubes (CNTs) [14,50], cellulose nanocrystals (CNCs) [51], graphene [48], and silicon dioxide nanoparticles (nano-SiO_2) [15,52]. Shahlari and Lee [47] investigated blends of PBAT/PLA filled with nano-sized layered silicates (nanoclays) and reported that the nanoclays were mainly located at the interface between the two polymers. They also reported that the incorporation of nanoclays not only increased the modulus of the nanocomposites but also reduced the size of the dispersed polymer phase. However, the elongation properties were diminished with the presence of nanoclays. Urquijo et al. [50] studied PLA/PBAT blends containing CNTs and found that CNTs were selectively located in the minor PBAT phase due to their greater compatibility. As a result, the shape of the PBAT phase developed from spherical to elongated shapes, leading to the formation of a co-continuous morphology. This phenomenon resulted in a significant improvement in toughness. However, they also observed that the Young's modulus remained unchanged, whereas the yield strength decreased with the addition of CNTs. Moreover, a study by Dil et al. [15] reported that the assembly of nano-SiO_2 into PLA/PBAT blends had an effect of stabilizing the co-continuous morphology without the deterioration of all the mechanical properties at a suitable loading of the PLA/PBAT ratio and nano-SiO_2.

It is interesting to point out that the final properties of PLA-based blend nanocomposites are strongly dominated by the presence of nanofillers. Furthermore, the type and content of nanofillers have played an essential role in improving and balancing the nanocomposite properties.

2.3 Polymer Blends

Polymer blends have been recognized as the most practical and economical approach to create new polymeric materials that combine all of the desired properties and even obtain

synergetic properties [36,53]. Polymer blends consist of two or more existing polymers with the properties in demand to usually produce multiphase materials for more complex applications. Furthermore, the utility of polymer blends can diminish the complexity and expense for developing a new polymer for a specific application. Generally, the blend properties can be tailored not only by altering the polymer components but also by adjusting the compositions of the blends [8]. As a result, the number of publications, patents, and PhD theses in this field has increased tremendously in the past several decades [54].

In principle, the polymer blends can exhibit miscibility, immiscibility (phase separation), or partial miscibility, which has decisive domination of the blend properties [8,54]. Miscibility is considered to be a single and homogenous phase material, whereas immiscibility is the phase-separated materials comprised of at least one dispersed polymer and a coherent polymer or matrix. Partial miscibility is indicated by a sufficient fraction of one polymer that can dissolve with another polymer at the molecular level while maintaining phase separation [55].

2.3.1   Thermodynamics of Polymer Blends

The most important feature of a polymer blend is its phase behavior, which can be described as the miscibility of two (or more) polymers [54]. The basic thermodynamic relationship can be applied to explain the miscibility through the Gibbs free energy (ΔG_m), which is defined by the following equation [56]:

$$\Delta G_m = \Delta H_m - T\Delta S_m \tag{2.1}$$

where ΔH_m and ΔS_m are the enthalpy and entropy of mixing, respectively, and T is the absolute temperature. For miscibility to occur, the ΔG_m must be a negative value ($\Delta G_m < 0$). This contribution is a sufficient requirement for low molecular weight mixtures (e.g., liquid–liquid and polymer–solvent mixtures). For higher molecular weight components such as polymer blends (polymer–polymer mixtures), the additional requirement for miscibility is given by the following relationship:

$$\left(\frac{\partial^2 \Delta G_m}{\partial \phi_i^2}\right)_{T,P} > 0 \tag{2.2}$$

where ϕ_i is the volume fraction of component i.

According to the relationship in equation (2.1), an increase in temperature generates better miscibility of the blend, as the term $T\Delta S_m$ increases and ΔG_m becomes more negative. This assumption correlates well with the low molecular weight components. However, for higher molecular weight components (polymer blends), the $T\Delta S_m$ term generally plays a small role compared with other factors (e.g., the contribution of non-combinatorial entropy and temperature-dependent ΔH_m values) [54]. Therefore, the latter factors lead to a decrease in miscibility with increasing temperature. Figure 2.6 illustrates the phase diagram of temperature versus composition for polymer blends that shows three distinct regions of different degrees of miscibility: a stable single-phase region, an unstable phase-separated region, and a metastable phase-separated region in between. The diagram also shows the behaviors of the lower and upper critical solution temperatures (LCST and UCST), including two critical points (marked as the crossing symbol). Even though polymer blends usually exhibit the LCST behavior as described earlier, in some cases, however, the blends can also show either both LCST and UCST behaviors or only the UCST behavior [54,57].
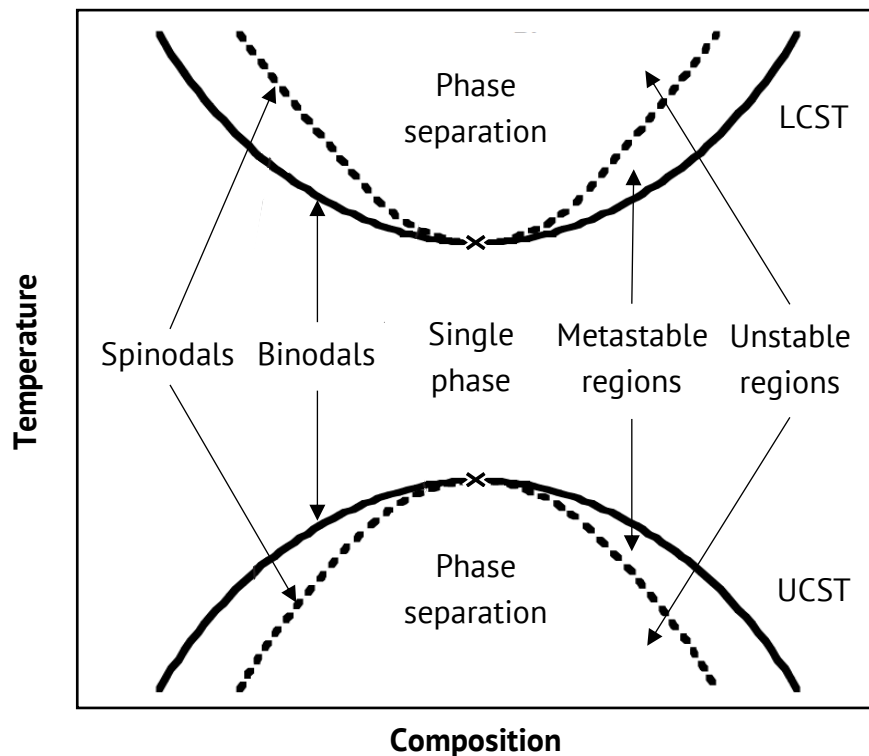
Figure 2.6: Phase diagram of temperature versus composition for polymer blends (adapted and modified from [54]).

Under certain thermodynamic conditions, two main mechanisms, which separate a single-phase and phase-separated polymer blend, are the binodal and spinodal mechanisms (see Figure 2.6).

The binodal curve is the boundary between a single-phase and phase-separated regions of the polymer blends and can be expressed by the following equations:

$$\Delta\mu_1^a = \Delta\mu_1^b \tag{2.3}$$

$$\Delta\mu_2^a = \Delta\mu_2^b \tag{2.4}$$

where 1, 2 and a, b are defined for polymers 1 and 2 and phases a and b, respectively. μ is the chemical potential of a component, which can be determined by the change in Gibbs free energy to the change in the number of moles of a component (n_i) [54,57].

$$\Delta\mu_i = \left(\frac{\partial\Delta G_m}{\partial n_i}\right)_{T,P,n_j} \tag{2.5}$$

The spinodal curve is basically defined as the boundary between the unstable and meta-stable phase-separated regions. The spinodal condition is thermodynamically determined from the following relationships:

$$\left(\frac{\partial^2\Delta G_m}{\partial\phi_i^2}\right)_{T,P} = 0 \tag{2.6}$$

The intersection between the binodal and spinodal curves is called the critical point, which is defined by the following relationship:

$$\left(\frac{\partial^3\Delta G_m}{\partial\phi_i^3}\right)_{T,P} = 0 \tag{2.7}$$

The Flory–Huggins theory established the relationships to access the miscibility of polymer blends and to calculate the Gibbs free energy [58,59]. The Flory–Huggins equation is shown as the following [54,58–60]:

$$\Delta G_m = kTV \left[\frac{\phi_1}{V_1} \ln \phi_1 + \frac{\phi_2}{V_2} \ln \phi_2 \right] + \phi_1 \phi_2 \chi_{12} kTV / \upsilon_r \tag{2.8}$$

where k = Boltzmann's constant, V = total volume, V_i = molecular volume of component i, χ_{12} = Flory–Huggins interaction parameter, and υ_r = interacting segment volume (a repeat unit volume) or reference volume. From equation (2.8), the enthalpy and entropy of mixing are, thus related, to equations (2.9) and (2.10), respectively [54].

$$\Delta H_m = \phi_1 \phi_2 \chi_{12} kTV / \upsilon_r \tag{2.9}$$

$$-T\Delta S_m = kTV \left[\frac{\phi_1}{V_1} \ln \phi_1 + \frac{\phi_2}{V_2} \ln \phi_2 \right] \tag{2.10}$$

The Flory-Huggins interaction parameter can be determined by the relationships of the solubility parameter of each component (δ_i) [53,54]:

$$\chi_{12} = \frac{V}{kT} (\delta_1 - \delta_2)^2 \tag{2.11}$$

As discussed earlier, the entropy contribution is rather small for polymer blends. Therefore, the significant parameter for directly accessing miscibility depends on the Flory–Huggins interaction parameter (χ_{12}). To achieve the miscibility at the molecular level, the difference in the solubility parameter of each component needs to be less than $\delta_1 - \delta_2 < 0.2$ (J/cm^3)$^{1/2}$ [53,61].

2.3.2 Phase Morphology of Immiscible Blends

It is well known that most of the polymer blends generally exhibit immiscibility or phase separation without further treatment (i.e., compatibilization) [54]. Regardless of the limitation in miscibility, the phase morphology of the immiscible polymer blends can be designed and developed into the desired properties. The phase morphology of the immiscible blends has the diversity in shape, size, and distribution of one phase to another depending on the material parameters (i.e., material composition, viscosity ratio, interfacial tension) and the processing conditions (i.e., temperature, time, shear rate, mixing strategy) [53,62]. Figure 2.7 shows a schematic of different morphologies of immiscible polymer

blends, which present droplet, double-emulsion, laminar, fiber, co-continuous, and or-
dered-microphase morphologies. As a result of the given morphologies, the prediction of
the possible performance, such as high toughness, high toughness and stiffness, good
barrier properties, and high flow properties, is allowed.

Droplet or sea-island

(toughness,
surface modification)

Double emulsion

(toughness and stiffness)

Laminar

(barrier)

Fibers

(strength,
thermal expansion)

Co-continuous

(high flow, electrical
conductivity,
toughness, stiffness)

Ordered microphases
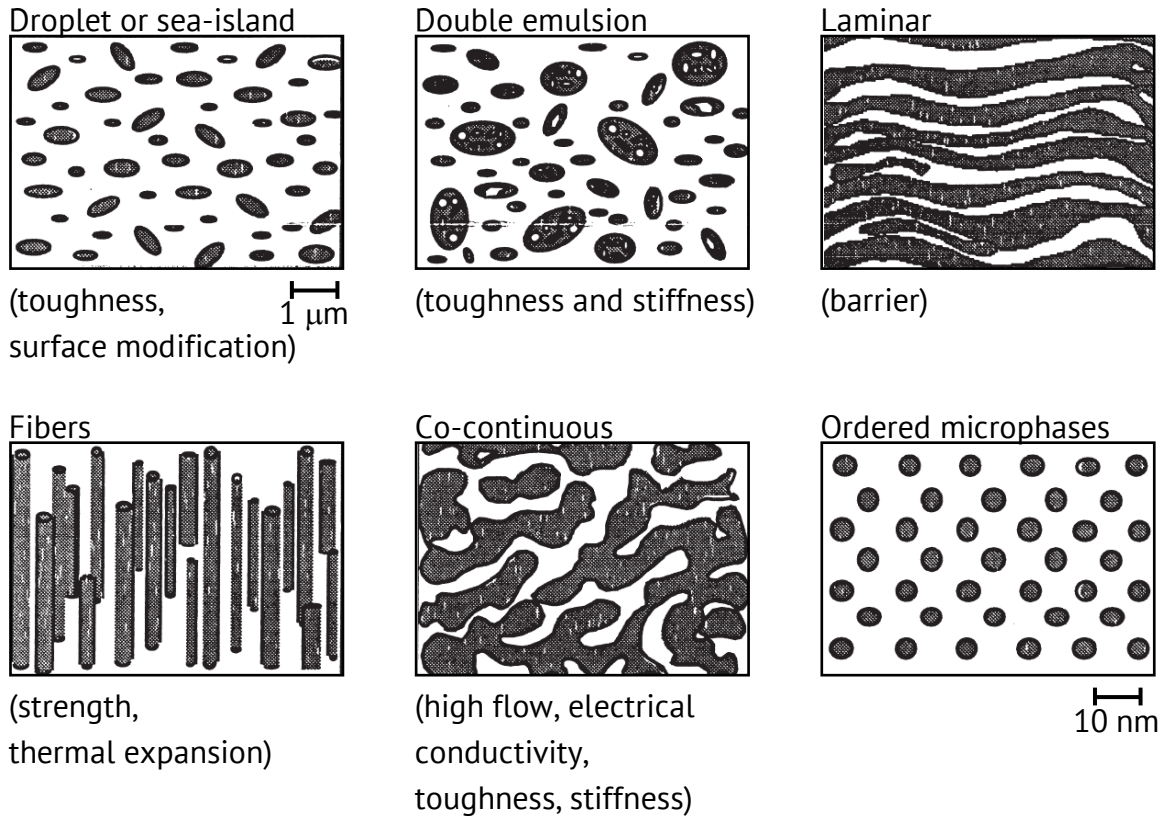
Figure 2.7:   Schematic of different morphologies of immiscible polymer blends based
on their end properties (adapted and modified from [63]).

However, from the viewpoint of a typical and broader classification, the phase morpho-
logy can be divided into two main categories: (i) a dispersed/matrix morphology (i.e.,
droplet or sea-island) and (ii) a co-continuous morphology [53]. The dispersed/matrix
morphology is attributed to the immiscible blends with a discrete phase structure of at
least one minor component surrounded by a continuous phase structure or the matrix. In
the case of the co-continuous morphology, the coexistence of at least two continuous
phase structures throughout the whole blend volume in multiple interpenetrated net-
works can be defined [53,64]. Figure 2.8 demonstrates the morphology development from
the dispersed/matrix morphology to the co-continuous morphology to the dispersed/
matrix morphology as a function of the polymer composition. The small spherical droplets

are formed at a low composition of a minor or dispersed phase. When the composition of the dispersed phase increases, the droplet coalescence plays an important role, resulting in an increase in the dispersed domain size with an ellipsoid shape; in some cases, an elongated fibrous structure might occur depending on the material and processing conditions [62,65,66]. At a particular composition, the phase inversion is promoted to a co-continuous morphology. However, the co-continuous morphology is inherently unstable; therefore, the break-up of the continuous phase into droplets can be seen in the final morphology [53,67,68]. The co-continuous morphology may remain if the blend is quenched rapidly. The phase inversion takes place again when the composition of the dispersed polymer increases and becomes a major component acting as a matrix.
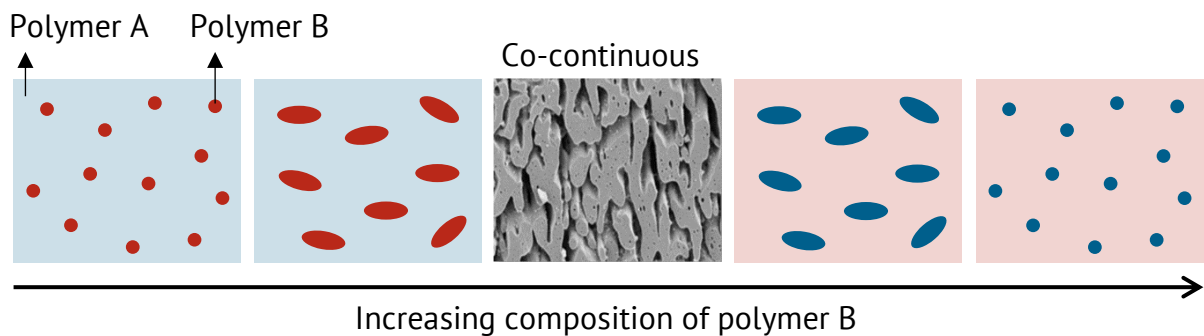
Figure 2.8:   Morphology development as a function of polymer composition (adapted and modified from [69,70]).

Li et al. [65] studied the morphology development of PLA/PBAT blends with various blending ratios. As a result, three distinct morphologies were observed. An increase in PBAT content created the transformation of the phase morphology from a spherical droplet (PBAT $\leq$ 20 wt.%) to a fibrous structure (~30 wt.% $\leq$ PBAT $\leq$ ~50 wt.%) to a co-continuous structure morphology (~50 wt.% $\leq$ PBAT $\leq$ 70 wt.%). Finally, the phase morphology reverted to the spherical droplet morphology at a PBAT content > 70 wt.%.

As already stated, the phase morphology is a key to determine the properties (i.e., mechanical, optical, rheological, and barrier properties) of immiscible polymer blends [53]. In general, polymer blends are usually processed by melt mixing of twin-screw extrusion, single-screw extrusion, or twin-rotor batch mixer (research purpose). Therefore, the phase morphology is defined during the mixing process. Initially, the polymer granulates in a solid form are heated and sheared inside the mixing or compounding machine (i.e., ex-

trusion) and then softened and eventually melted. During the melting process, the granulates are stretched into a sheet form. Subsequently, the phase inversion might take place. If a minor polymer (lower composition) melts first, it becomes a continuous phase. Then, when a major polymer (higher composition) melts with a sufficient concentration, the phase inversion occurs from the continuous phase to a dispersed phase and vice versa. However, when the major polymer melts before the minor one, the phase inversion will not happen [53]. In addition, the co-continuous morphology can also occur at around the phase inversion point [71].

Scott and Macosko [72,73] proposed the mechanism of morphology development of the dispersed phase during the melt mixing, as shown in Figure 2.9. The dispersed phase transforms from sheet or ribbon to fiber and then breaks into droplets during the melting process. At a droplet concentration higher than 1 %, the coalescence process is generated unless the compatibilizer is applied to stabilize the morphology [63]. Finally, the final morphology is a result of the competition of simultaneous break-up and coalescence processes during melt mixing [62,72,74,75].
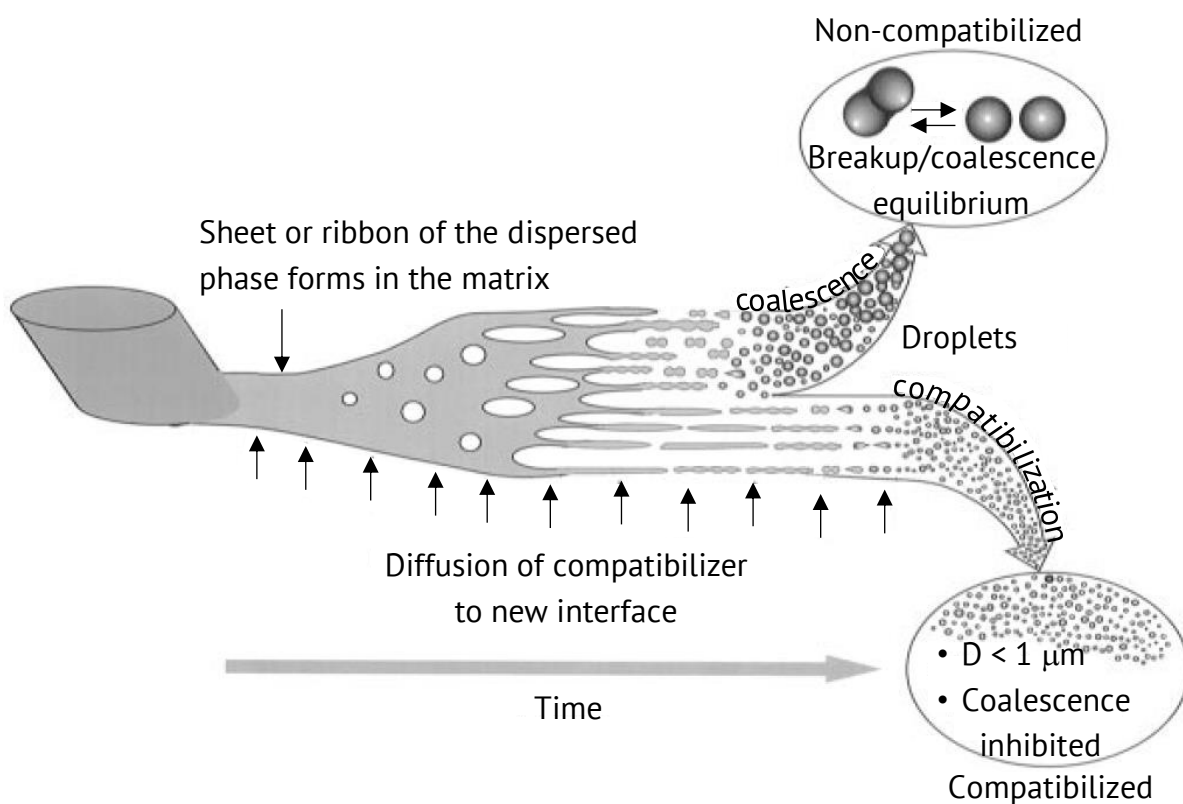
Figure 2.9:   Morphology development in an immiscible polymer blend as proposed by Scott and Macosko (adapted and modified from [72,73]).

As a result, a decrease in the dispersed phase takes place during the first few minutes of the melt-mixing from the millimeter-sized granulates to the micrometer- or even nanometer-sized dispersed domains [76].

2.3.2.1 Droplet Break-Up Mechanism

The droplet break-up has been studied rather intensively by Taylor [77], in particular of a single Newtonian drop in a simple shear field [62]. The capillary number (Ca) is applied to describe the change in geometry of the dispersed phase. It is a relationship between the hydrodynamic stresses (viscosity of the matrix, η_m) and the interfacial tension between the phases, γ_{12}, as expressed by the following equation [53,77]:

$$Ca = \frac{\eta_m \dot{\gamma} R}{\gamma_{12}} \tag{2.12}$$

where $\dot{\gamma}$ is the shear rate and R is the radius of the undeformed droplet. If the hydrodynamic stresses dominate over the interfacial tension, the Ca value is higher than a certain value or so-called critical capillary number (Ca_{cr}). Consequently, the droplets become unstable, deformed, and eventually broken. According to Taylor [77], the Ca_{cr} is given by the following equation:

$$Ca_{cr} = 0.5 \frac{16\eta_r + 16}{19\eta_r + 16} \tag{2.13}$$

where η_r is the viscosity ratio between the dispersed phase and the matrix (η_d/η_m).

Under the Ca_{cr} consideration, Grace [78] experimentally reported the relationship of the Ca_{cr} and η_r with two different flow fields, shear and elongation, as shown in Figure 2.10. As a result, the elongational flow is more efficient in the droplet break-up than the simple shear flow. Starý [76] explained that the droplets are restricted to rotate under the elongational flow and unable to circulate the material inside the droplets. These behaviors result in energy dissipation.
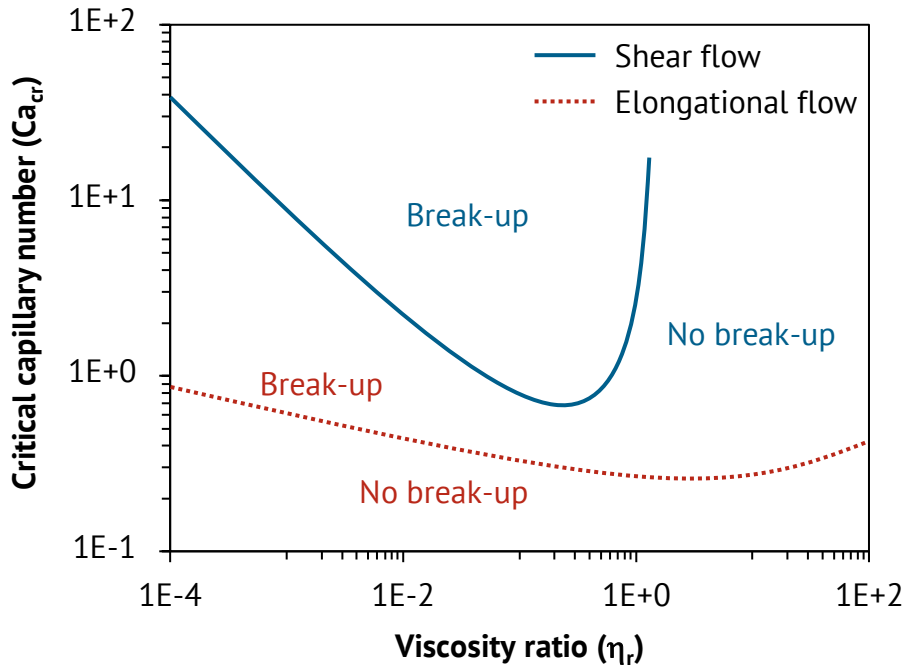
Figure 2.10:   Droplet break-up behavior on the relationship of the critical capillary number (Ca_{cr}) and viscosity ratio (η_r) (adapted and modified from [78,79]).

Afterward, de Bruijn [80] proposed an empirical equation for shear flow of Ca_{cr} based on the experimental data of Grace [78], as described below:

$$\log Ca_{cr} = -0.506 \tag{2.14}$$
$$- 0.0995 \log \eta_r + 0.124 \big(\log \eta_r\big)^2 - \frac{0.115}{\log \eta_r - \log 4.08}$$

Also, Utracki and Shi [81] proposed an equation for elongational flow, as described below [82]:

$$\log Ca_{cr} = -0.64853 \tag{2.15}$$
$$- 0.02442 \log \eta_r + 0.02221 \big(\log \eta_r\big)^2$$
$$- \frac{0.00056}{\log \eta_r - \log 0.00645}$$

To achieve the finest diameter of the dispersed droplets, η_r should be closer to 1 [53]. Figure 2.11 shows the possibilities of the droplet break-up mechanisms under a flow field. The droplet break-up mechanisms can be related to the η_r value under a shear flow field. For $\eta_r < 0.1$, a tip streaming mechanism is observed. The tip streaming generates very fine droplets at the tip of a deformed droplet. A necking and/or end pinching mechanism can

be observed for $0.1 < \eta_r < 1$. The necking usually produces two daughter droplets from a deformed droplet, and the end pinching is formed by the creation of a dumbbell droplet, where two droplets are broken at the ends. A Rayleigh break-up mechanism is found for $1 < \eta_r < 3.8$. The Rayleigh break-up is attributed to the interfacial instability of the surface of the fibril, which breaks up into a line of droplets. For $\eta_r > 3.8$, no droplet can be deformed due to the droplet being too viscous [53,76,79].
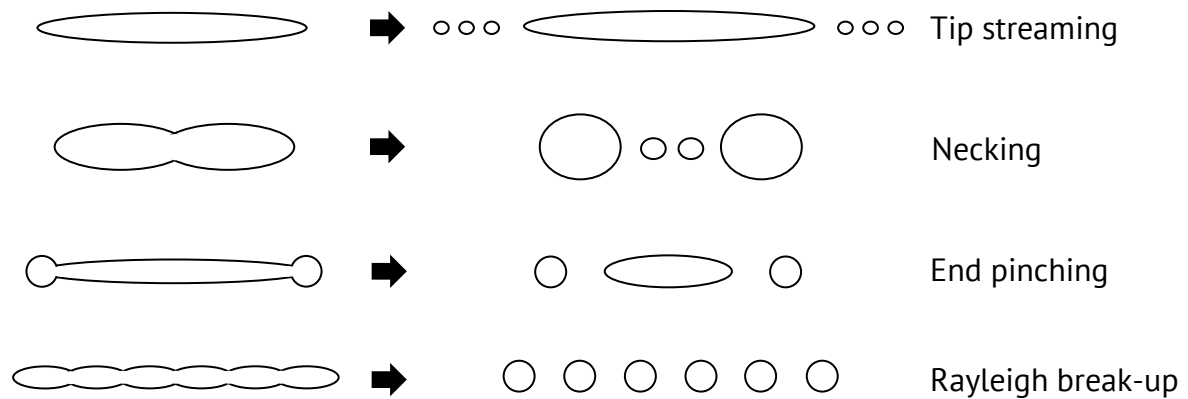
Figure 2.11:   Possibilities of droplet break-up mechanisms in polymer blends under a flow field (adapted and modified from [76,79]).

2.3.2.2 Coalescence Mechanism

Coalescence is a process of two or more dispersed droplets colliding together during the mixing process when there is no involvement of a stabilizer or compatibilizer. Unlike droplet break-up, the coalescence process leads to an increase in the droplet size. The effects of coalescence on the droplet size are governed by the concentration of the dispersed phase, the number of droplets, the interfacial tension, and the shear stress [53]. The flow-induced coalescence is applied to explain the collision between the two droplets [62,76]. Figure 2.12 illustrates the idealized depiction of the coalescence mechanism in immiscible polymer blends. The process starts with the approach of the two droplets by the flow field. Film drainage of the matrix is formed, caused by the squeezing between the two droplets. If the film thickness reaches to its critical value, film rupture occurs. Finally, the relaxation of the droplet shape is formed by the coalescence process [83,84].

i) Approach of the droplets   **ii)** Film drainage of the matrix   **iii)** Rupture of the film   **iv)** Droplet relaxation, Coalescence
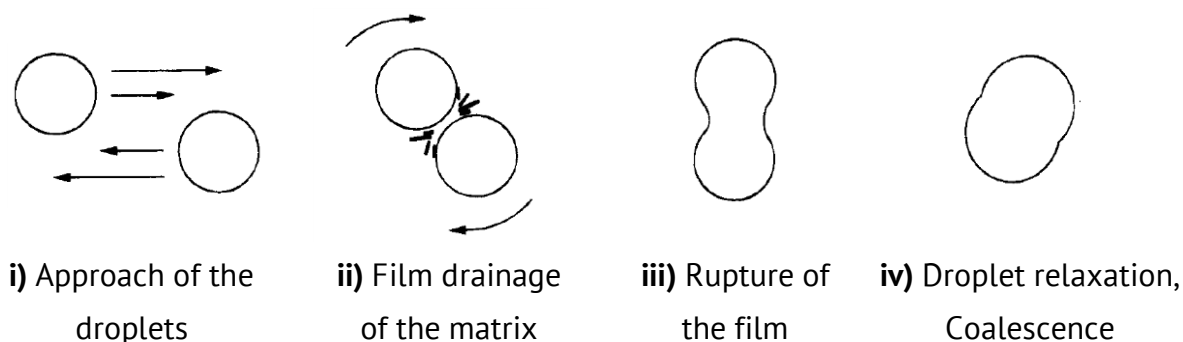
Figure 2.12:   Idealized depiction of the coalescence mechanism in immiscible polymer blends (adapted and modified from [62,83]).

2.4   Polymer Blend Nanocomposites

As discussed earlier, a mixture of two or more polymers can create a new material with the desired and specific properties without synthesizing a new polymer. Nevertheless, deterioration of some aspects can occur owing to the immiscibility of the polymer blend. An assembly of fillers, especially in the nanoscale, has been introduced in a polymer blend to optimize the material performance as well as to broaden applications. Generally, the addition of nanofillers enhances the mechanical and physical properties of the polymers [11–13]. Accordingly, polymer blends containing nanofillers or polymer blend nanocomposites can be tailored not only by the types of polymers used but also by the nanofillers. Nanofillers can be classified into three categories in terms of their geometries: (i) sheet-like nanofillers (1D, i.e., nanoclays, graphene sheets), (ii) fiber or tube nanofillers (2D, i.e., carbon nanotubes (CNTs), cellulose nanocrystals (CNCs)), and (iii) spherical nanofillers (3D, i.e., silicon dioxide (SiO_2)) [13,16]. Figure 2.13 shows the schematics of the three categories of nanofillers. In addition, polymer blend nanocomposites are defined by the polymer blends containing nanofillers with at least one dimension in the range of 1–100 nm [13,85]. The high surface area of nanofillers can produce an ultra-large interfacial area per unit volume between the polymers and the nanofillers. Consequently, the superior performance of the polymer blend nanocomposites can be reached at very low nanofiller loadings [11,13].

Sheet-like nanofillers
Thickness ~1 nm

Fiber or tube nanofillers

Diameter < 100 nm

Spherical nanofillers
Diameter < 100 nm

a) **b)** **c)**
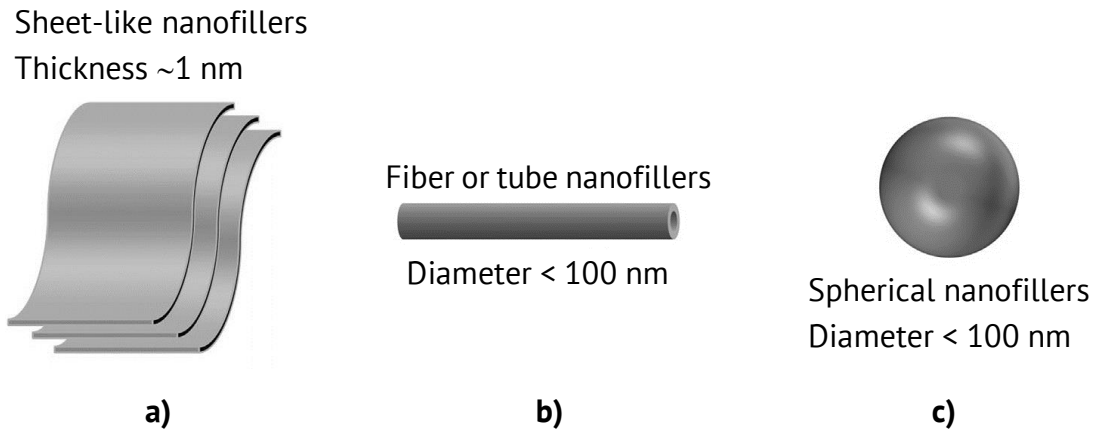
Figure 2.13:   Categories of nanofillers: a) sheet-like nanofillers, b) fiber or tube nano-fillers, and c) spherical nanofillers (adapted and modified from [11,16]).

All the categories of nanofillers have been utilized to improve or optimize the properties of polymer blends with their individual properties. Jiang et al. [86] studied PLA/PBAT blends containing montmorillonite clay (MMT). As expected, the presence of PBAT reduced the tensile strength and modulus of PLA. However, the inclusion of 5 wt.% MMT restored the strength of the blend and increased the modulus to even higher than that of the pure PLA. The incorporation of multi-walled carbon nanotubes (MWCNTs) in PLA/PS blends was reported by Lee et al. [87]. They reported that the electrical resistivity of the nanocomposites decreased with increasing MWCNT content (1–10 wt.%). In the meantime, the electrical percolation threshold was lowered (0–1 wt.%). In a study by Yu et al. [88], they showed that a PLA/thermoplastic polyurethane (TPU)-based nanocomposite exhibited an improvement in the strain at break and impact strength with the addition of 2 wt.% hydrophobic nano-SiO_2 without sacrificing the strength and stiffness.

In this study, particular attention is given to the spherical nanofillers, specifically nano-SiO_2. As a spherical shape, the nanoparticles can be utilized as nanofillers with isotropic properties. The average particle size and specific surface area are in the range of 3–250 nm and 50–400 m^2/g, respectively [89]. Nano-SiO_2 is delivered as a fine, transparent, odorless, and tasteless powder that is abundant in nature [90,91]. According to the literature, the incorporation of nano-SiO_2 has been considered one of the best candidates for producing nanocomposites with a diversity of desired functions, such as toughening, reinforcement, thermal resistance, nucleating agent, and gas barrier [9,13,16,92,93]. Nano-SiO_2 is an inorganic filler containing silanol groups (Si-OH) on its surface, as shown

in Figure 2.14(a). Therefore, the nano-SiO_2 particles exhibit intrinsically hydrophilic pro-
perties with a high interaction of hydrogen bonding. This behavior has led to the strong
aggregation and agglomeration of nanoparticles. Figure 2.15 shows the schematic struc-
tures of nanoparticles in the form of primary nanoparticles, aggregates, and an agglo-
merate. It is well known that uniform dispersion of nanofillers is required to obtain the
ultimate performance of the nanocomposites [18]. Therefore, surface modification of
nano-SiO_2 is required to diminish the hydrophilicity of the nanoparticles. Figure 2.14(b)
illustrates the aggregation structure of SiO_2 nanoparticles after surface modification by
hexamethyldisilazane (HMDS). According to Evonik Industries, the hydrophobic nano-SiO_2
with surface modification has a lower interaction among the particles, leading to a de-
crease in the agglomerate size of the nano-SiO_2 [94].
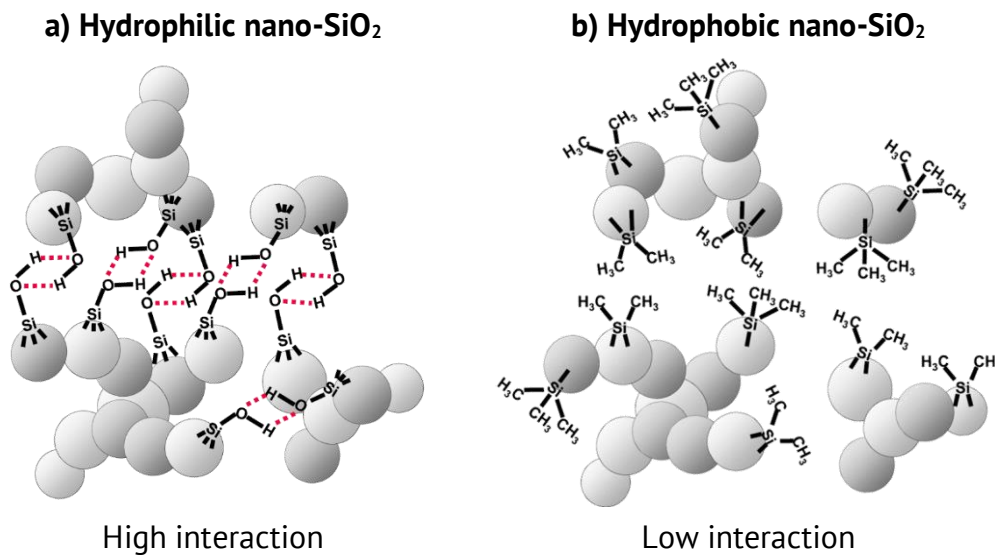
Figure 2.14:   Aggregation structures of a) hydrophilic and b) hydrophobic nano-SiO_2
(adapted and modified from [94]).
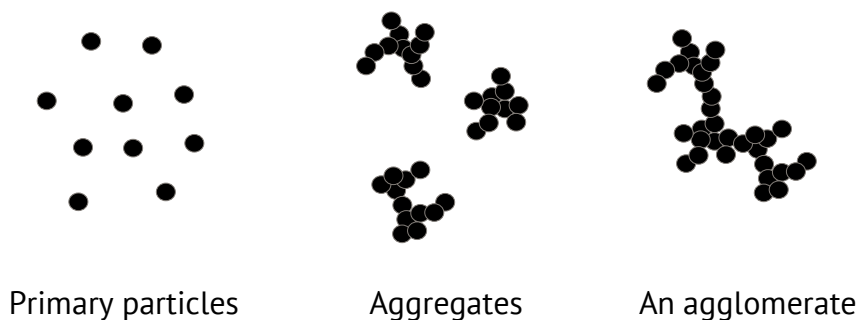
Figure 2.15:   Primary particles, aggregates, and an agglomerate of nanoparticles
(adapted and modified from [94]).

Dorigato et al. [95] reported that the hydrophobic nano-SiO_2 exhibited a finer dispersion of aggregate nano-SiO_2 in the PLA matrix compared to the unmodified nanoparticles. Moreover, the remarkable improvement in the tensile properties, fracture toughness, and creep stability was observed in the presence of the surface-modified nano-SiO_2.

In addition, it is interesting to note that the de-agglomerates can take place into the aggregates by shear force during melt mixing such as extrusion [94,96]. Knör et al. [97] showed that polyamide (PA)/TiO_2 nanocomposites prepared by a two-step melting process presented the de-agglomeration of the nano-TiO_2. The result led to an improvement in the impact strength by 141 %. Thereafter, Lin and Schlarb [96] reported well-dispersed thermoplastic-based nanocomposites by using a masterbatch dilution process. The masterbatches (PP/SiO_2 and PP/TiO_2) with a high filler content were first prepared by extrusion and then diluted to a required nanocomposite content with the same processing conditions. The obtained nanocomposites revealed a smaller size and narrow distribution of the agglomerate nanoparticles when compared to the one-step melting process.

2.4.1 Phase Morphology of Polymer Blend Nanocomposites

Most of the polymer blends have phase-separated morphology, which is an important key to determine the final feature of the materials. The incorporation of nanoparticles is a well-established approach not only to enhance the desired properties in the polymer blends but also to control and stabilize the phase morphology between the two polymers [5,14,15]. In such systems, it is generally known that the nanoparticles most likely have a preferential location either in one polymer phase or at the interface between the two polymers, as shown in Figure 2.16 [5,15,17,98]. As a result, the location of nanoparticles and the interfacial properties between two components (polymer–polymer and polymer–nanoparticles) are essential factors to control the overall properties of polymer blend nanocomposites [5]. In addition, the phase morphology of polymer blend nanocomposites as well as the nanoparticle location are governed by the thermodynamic effects and/or kinetic effects [12,18,99]. The thermodynamic effects can be described by the surface properties of each component or wetting parameters, and the kinetic effects can be explained by the processing sequence, processing time, and viscosity ratio [5,12,18,99]. These factors will be described in the next section.

a) Nanoparticles locate
in polymer 1

b) Nanoparticles locate
in polymer 2

c) Nanoparticles locate
at the interface
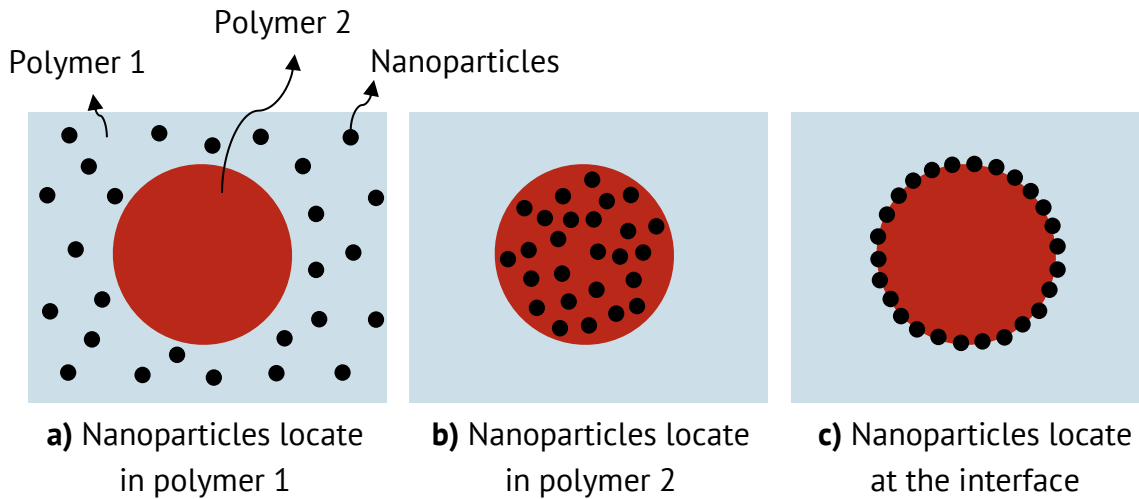
Figure 2.16:   Selective location of nanoparticles in immiscible polymer blends.

2.4.2   Factors Determining the Location of Nanoparticles

2.4.2.1 Thermodynamic Effects

Wetting Parameters

The theory of equilibrium thermodynamics is applied to predict the location of nanopar-
ticles in the polymer blends. It is related to the affinity of the nanoparticles to each po-
lymer, indicated by interfacial energies (γ_{ij}) between the polymer pair and the polymer
and nanoparticles [18]. As described by Sumita et al. [100], the interfacial energies can
be used to calculate the wetting parameter (ω) (see Figure 2.17). According to the calcu-
lated ω value, if ω is greater than 1 ($\omega > 1$), the nanoparticles are located in polymer 2. If
ω is less than -1 ($\omega < -1$), the nanoparticles are located in polymer 1. If ω is in between
-1 and 1 ($-1 < \omega < 1$), the nanoparticles are located at the interface between the two
polymers.

$$\omega = cos\theta = \frac{\gamma_{1s} - \gamma_{2s}}{\gamma_{12}}$$
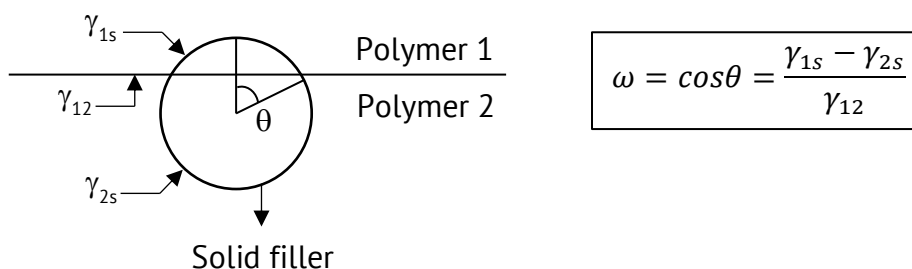
Figure 2.17:   Schematic representation of a solid filler at the interface between polymers
1 and 2 and an equation of the wetting parameter (adapted and modified from [18,100]).

Several studies have reported the blend nanocomposite system and agreed with the prediction by Sumita et al. [100]. For instance, Nofar et al. [49] studied the location of nanoclay in PLA/PBAT blends and used a wetting parameter to predict the location of the nanoclay. They found that with 1 wt.% nanoclay, the nanoparticles were located at the interface between the PLA and PBAT, as predicted from the wetting parameter, irrespective of the mixing sequence. In a study by Heshmati et al. [101], bio-based PLA/PA11 nanocomposites were prepared using spray-dried CNC nanoparticles. Firstly, the PLA/CNC and PA11/CNC mixtures were prepared by casting, evaporating, and grinding the prepared suspension. Then, the PLA/PA11/CNC nanocomposites were prepared by mixing both the PLA/CNC and PA11/CNC mixtures with PA11 and PLA, respectively, using an internal-melted mixer. They found that the CNC nanoparticles were selectively located in the PA11 phase regardless of the mixing strategies. The nanoparticle location was also in good agreement with the prediction of the calculated wetting parameter.

However, the balance of the nanocomposite system can alter the equilibrium location of the nanoparticles by using a compatibilizer. Li et al. [19] studied PET/PP/TiO$_2$ without and with PP-grafted maleic anhydride (PP-g-MA) as a compatibilizer. Based on the thermodynamic prediction, the nanoparticles should be located in the PET phase. They found that the TiO$_2$ nanoparticles were located in the PET phase, which was consistent with the thermodynamic prediction. However, in the case of PET/PP/PP-g-MA/TiO$_2$, the location of the nanoparticles changed from the PET phase to the PP phase. They explained that TiO$_2$ nanoparticles were readily absorbed by the maleic anhydride, which is an excellent ligand for metal oxides. Therefore, the PP-g-MA acted as a bridge between the PP phase and the nanoparticles.

2.4.2.2 Kinetic Effects

Besides the thermodynamic effects that control the location of the nanoparticles, kinetic effects can also play a dominant role in the uneven distribution of the nanoparticles [18–20]. The kinetic effects are involved in the rate of the mixing process in such systems [20]. Accordingly, the related factors – processing strategy, processing sequence, and viscosity ratio – can rule out the equilibrium thermodynamic consideration and must be taken into account for the blend nanocomposite system.

Processing Sequence

The location of the nanoparticles can be influenced by the processing sequence or the order in which each component is added during melt compounding. As described by Nazockdast [12], the processing sequence can be mainly classified into three different routes. The first route is known as direct mixing. In terms of direct mixing, all the components are mixed simultaneously in the mixing machine (one-step process). In this route, the nanoparticles will first be dispersed in a polymer phase, which has a lower melting temperature. After that, the nanoparticles might migrate to another polymer phase that has a thermodynamically preferred location. As a result, it is difficult to distinguish an actual parameter for describing the final location of the nanoparticles. In the second route, the polymer components are pre-melted at a certain amount of time, and then the nanoparticles are added during the melt compounding (two-step process). In the third route, the first polymer and nanoparticles are first blended. Afterward, the obtained compound is blended with a second polymer (two-step process).

In the work of Li et al. [19] mentioned earlier, although the addition of a compatibilizer (PP-g-MA) altered the location of TiO_2 nanoparticles in the PET/PP blends from the PET phase to PP phase in the direct mixing, the change in the processing sequence can restrain the influence of the compatibilization effect between PP and maleic anhydride. When PET and TiO_2 were blended in the first step and then PP and PP-g-MA were added in the second step, the nanoparticles were located in the PET phase. The authors explained that PET chains at the beginning encapsulated the TiO_2 nanoparticles. When PP-g-MA was added in the second step, it, therefore, reacted mostly with the hydroxyl groups of the PET polymer instead of the nanoparticles. Dil and Favis [52] also studied the thermodynamic and kinetic effects of PLA/PBAT/SiO_2 nanocomposites. The thermodynamic prediction showed that the preferential location of SiO_2 nanoparticles was determined to be in the PBAT phase. The result agreed with the prediction for direct mixing. However, by pre-mixing PLA with SiO_2 and then later adding PBAT, the location of the nanoparticles changed and was at the interface between the two polymers. The slow migration velocity at the interface between the PLA and PBAT polymers was used to explain the obtained result. Consequently, the result indicates that the processing sequence has the potential to prevent the equilibrium thermodynamic location in the final morphology of the blend nanocomposite systems.

Processing Time

As previously mentioned, the migration of nanoparticles from their initial location to their thermodynamically preferred location can occur during melt compounding. It is assumed that if the processing time is sufficient and material and mixing conditions are suitable, the nanoparticles can stay entirely in their equilibrium thermodynamic location. Therefore, the processing time is one of the essential factors for controlling the final morphology of the polymer blend nanocomposites.

Urquijo et al. [102] studied the kinetically induced nanoclay location of PLA/PCL-based nanocomposites filled with organically modified montmorillonite (OMMT). The nanocomposites were prepared by using a twin-screw extruder under high shear conditions and a low residence time (~30 s). The results showed that OMMT nanoparticles were first located in the PCL phase, although their preferred location was in the PLA phase [14,102]. This behavior can be explained by the fact that since PCL has a lower melting temperature (~60–65 °C) compared to PLA (~160 °C), the nanoparticles were, therefore, initially dispersed in the PCL phase and did not have enough time to migrate to their preferred location. To confirm this concept, Urquijo et al. [102] also experimented further by re-mixing and increasing the processing time to 5, 10, and 15 min. They found that OMMT nanoparticles migrated to the PLA phase and at the PLA/PCL interface, the concentration of nanoparticles at their new locations increased with increasing mixing time. Moreover, the change in the nanoparticle location also altered the final morphology of the nanocomposites from a co-continuous to a sea-island morphology.

Viscosity Ratio

The migration rate of nanoparticles is generally involved with the viscosity of the melted polymers during compounding [12,20]. Many studies have reported on the effects of the viscosity ratio on the location of nanoparticles [14,52,103–106]. For example, Wu et al. [14] reported selective location of CNTs on PLA/PCL blends. They used two different types of PCLs with different viscosities. For a high viscosity ratio between the PLA and PCL, CNTs were selectively located in the PCL phase (which was a lower viscous phase) and at the interface. On the other hand, for a reduced viscosity ratio, the thermodynamic effect became a dominant factor, leading to the change in the nanoparticle location from the PCL phase to the PLA phase. In a work by Persson and Bertilsson [103], they demonstrated PE/polyisobutylene (PIB) blends containing aluminum borate whisker, in which the polymer pairs had different viscosities. The results showed that the whisker was dispersed in

the high viscosity polymer phase. They explained that the whisker was absorbed by the high viscosity phase to minimize its dissipative energy. In their previous study, they observed the location of the whisker in poly(styrene-co-acrylonitrile) (SAN)/PA6 blends and found that the whisker was preferably located in the lower viscosity polymer [107]. They finally concluded that the viscosity ratio plays a dominant role only when the thermodynamic affinity in the system is comparable.

In another interesting work, Elias et al. [106] studied PE/poly(ethylene-co-vinyl acetate) (EVA) filled with hydrophilic and hydrophobic nano-SiO_2. EVAs with two different viscosities were used as a dispersed polymer. According to the thermodynamic prediction, the hydrophilic nano-SiO_2 should be located in the EVA phase and the hydrophobic nano-SiO_2 should stay at the interface. The obtained results showed that the hydrophilic nano-SiO_2 was located in the EVA phase irrespective of the EVA viscosity. In contrast, the hydrophobic nano-SiO_2 was able to migrate to its preferred location only in the case of the low viscosity EVA. This behavior was because the EVA polymer is an initial dispersed phase (lower melting temperature).

As stated in the above examples, the viscosity ratio has a weaker effect compared to the thermodynamic consideration. However, it is challenging to distinguish the real effect of the nanoparticle location because the melt mixing of polymer blend nanocomposites has several parameters (thermodynamic and kinetic effects) that must be taken into consideration.

3 Experimental Procedures

3.1 Materials

3.1.1 Bioplastics

In this study, a commercial poly(lactic acid) (PLA) (Ingeo™ 3251D, NatureWorks, Minnetonka, USA) was used as a polymer matrix (see Appendix A). This commercial grade is designed for injection molding applications. A commercial poly(butylene adipate-co-terephthalate) (PBAT) (ecoflex® F Blend C1200, BASF SE, Ludwigshafen, Germany) was used as a dispersed polymer (see Appendix B). It has been developed for flexible films using blown film or cast film process. The characteristics of the polymer matrix and dispersed polymer used in this work are listed in Table 3.1.

Table 3.1:   Characteristics of the bioplastics used in this work [108,109]

Properties	Unit	Matrix phase	Dispersed phase
		PLA	PBAT
Density	g/cm^3	1.24	1.25–1.27
Melt flow rate (190 °C, 2.16 kg)	g/10 min	35	2.7–4.9
Crystallization temperature (5 K/min)	°C	99	51
Glass transition temperature (10 K/min)	°C	61	-29
Melting temperature (10 K/min)	°C	168	124
Young's modulus	MPa	3680	–
Tensile strength	MPa	73.6	35–44
Elongation at break	%	4.8	560–710

3.1.2 Nanofillers

A hydrophobic fumed silicon dioxide (nano-SiO_2) (AEROSIL® R 8200, Evonik Industries, Hanau-Wolfgang, Germany) was used as dispersed nanofillers (see Appendix C). It has 12 nm diameter of primary particles and a structure modified with hexamethyldisilazane.

The characteristics of the nano-SiO_2 referred to the information of manufacturer and literatures are listed in Table 3.2.

Table 3.2:   Characteristics of the nanofillers used in this work [110–113]

Properties	Unit	Nanofillers
Diameter of primary particles	nm	12, spherical
Specific surface area	m^2/g	135–185
Density	g/cm^3	~2
SiO_2 content	%	≥99.8
Behavior in water	–	Hydrophobic
Young's modulus	GPa	73
Surface tension		
γ	mJ/m^2	32
γ^d		30
γ^p		2

3.2   Material Preparation

3.2.1   Extrusion

Prior to melt processing, all the polymer granulates were dried in an oven at 80 °C for 15 h to avoid moisture-induced degradation. All compounding processes were carried out on a co-rotating twin-screw extruder (Leistritz ZSE 18 MAXX 40D, Leistritz Extrusionstechnik GmbH, Germany). The screw diameter is 18.5 mm and the screw has a length to diameter (L/D) ratio of 40 (see Appendix D). A single screw side feeder with the screw diameter of 16 mm was assembled for the introduction of the nanoparticles. The temperature profiles and screw speeds of all compounding processes are listed in Table 3.3.

Table 3.3:   Processing conditions of all compounds

Material	Temperature profile, °C (From feeding zone to die zone)	Screw speed, rpm	
		Main screw	Side feeder
PLA–SiO$_2$	80/120/150/180/185/190/190/190/190/190/190	50	200
PBAT–SiO$_2$	100/150/160/170/180/190/200/205/205/205/205	50	200
PLA–PBAT	80/120/150/180/185/190/190/190/190/190/190	50	–
PLA–PBAT–SiO$_2$	80/120/150/180/185/190/190/190/190/190/190	50	200

To achieve uniform distribution and dispersion of nanoparticles, a high concentration of polymer and nanofillers, a so-called masterbatch, was pre-prepared. For processing sequence purposes, two different masterbatches of PLA and nano-SiO$_2$ (MB-PLA) and PBAT and nano-SiO$_2$ (MB-PBAT) were compounded with a nanoparticle content of 30 wt.% (21.0 vol.% and 21.3 vol.%, respectively). Each masterbatch was processed through the extrusion with a two-time process (15 wt.% nano-SiO$_2$ for each time). Then, the masterbatches were mixed and diluted by neat PLA and neat PBAT to obtain different materials with four processing procedures. The four processing procedures are described as following and illustrated in Figure 3.1;

Procedure 1 (P1):   MB-PLA, neat PLA, and neat PBAT were directly compounded in one-step process.

Procedure 2 (P2):   MB-PLA and neat PLA were first compounded. The obtained compound (Pre-P2) was dried and compounded again with neat PBAT (two-step process).

Procedure 3 (P3):   MB-PBAT, neat PBAT, and neat PLA were directly compounded in one-step process.

Procedure 4 (P4):   MB-PBAT and neat PBAT were first compounded. The obtained compound (Pre-P4) was dried and compounded again with neat PLA (two-step process).

Compounds of PLA containing nano-SiO$_2$ (PLA-S1) and PLA/PBAT blend without nanofillers (S0) were also prepared for comparison purpose. Table 3.4 summarizes the details of all the materials used in this work.
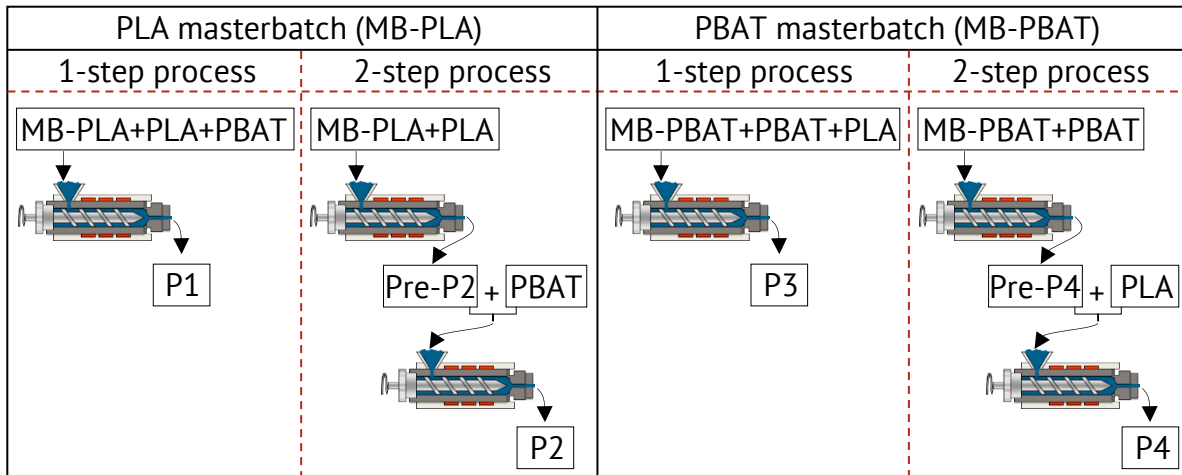
Figure 3.1:   Schematic diagram of the four processing procedures.

Table 3.4:   Summary of all materials used in this work

Materials		Volume ratio	Blending process	
Full name	Short name	(PLA : PBAT : SiO$_2$)	Step 1	Step 2
PLA	PL	100 : 0 : 0	–	–
PLA-S1	PL1	99 : 0 : 1	MB-PLA + PLA	–
PLA/PBAT-S0	S0	80 : 20 : 0	PLA + PBAT	–
PLA/PBAT-S1-P1	S1-P1	79.2 : 19.8 : 1	MB-PLA + PLA + PBAT	–
PLA/PBAT-S1-P2	S1-P2	79.2 : 19.8 : 1	MB-PLA + PLA (Pre-P2 or Step 1)	Pre-P2 + PBAT
PLA/PBAT-S1-P3	S1-P3	79.2 : 19.8 : 1	MB-PBAT + PBAT + PLA	–
PLA/PBAT-S1-P4	S1-P4	79.2 : 19.8 : 1	MB-PBAT + PBAT (Pre-P4 or Step 1)	Pre-P4 + PLA
PLA/PBAT-S4-P1	S4-P1	76.8 : 19.2 : 4	MB-PLA + PLA + PBAT	–
PLA/PBAT-S4-P2	S4-P2	76.8 : 19.2 : 4	MB-PLA + PLA (Step 1)	Step 1 + PBAT
PLA/PBAT-S4-P3	S4-P3	76.8 : 19.2 : 4	MB-PBAT + PBAT + PLA	–
PLA/PBAT-S4-P4	S4-P4	76.8 : 19.2 : 4	MB-PBAT + PBAT (Step 1)	Step 1 + PLA
PBAT	PB	0 : 100 : 0	–	–

3.2.2   Injection Molding

After extrusion process, all the materials listed in Table 3.4 (except neat PBAT) were in-
jection-molded into 50 x 50 x 4 mm^3 plates using an injection molding machine (VC
200/80 SPEX, ENGEL AUSTRIA GmbH, Schwertberg, Austria) under the screw speed of
190 rpm. The screw diameter and L/D ratio are 25 mm and 24.8, respectively. The details
of the injection molding parameters are given in Table 3.5.

Table 3.5:   Injection molding parameters of all materials

Material	Temperature profile, ºC		Injection pressure, bar
	From feeding zone to die zone	Mold	
PLA PLA–SiO$_2$	175/180/185/185	40	700
PLA–PBAT PLA–PBAT–SiO$_2$	185/185/190/195	40	700

3.3   Material Characterizations

3.3.1   Preparation of Testing Samples

For further characterization, the injection-molded plates were milled and cut into dif-
ferent shapes and dimensions, as shown in Figure 3.2. The thin film of 10 μm thickness
was prepared by using a rotation microtome (Hyrax M 25, Carl Zeiss MicroImaging GmbH,
Jena, Germany) for polarized light optical microscope (PLOM) investigation. In addition,
neat PLA and PBAT granulates were used to prepare PLA and PBAT films for surface wet-
ting properties. The films with a thickness of approximately 0.3 mm were compression-
molded on a hot plate at 200 ºC between two glass plates and polytetrafluoroethylene
(PTFE) release foil. All prepared films have an average surface roughness (Ra) of 0.4 μm.
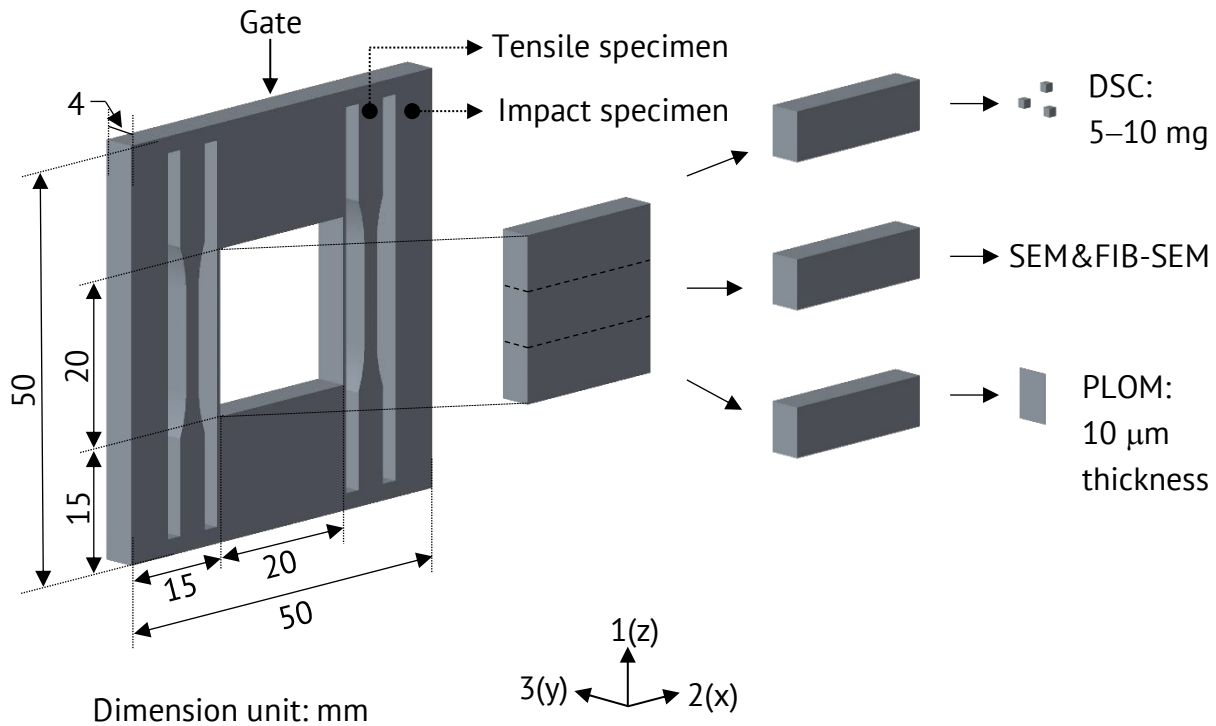
Figure 3.2: Preparation of the testing samples from the injection-molded plates.

3.3.2 Morphology

The morphology in terms of dispersion and distribution of SiO_2 nanoparticles as a dispersed nanofiller and PBAT droplets as a dispersed polymer was investigated under a scanning electron microscope (SEM) (SU8000, Hitachi, Japan). The acceleration voltage of 5 kV was used for the investigation. A rectangular sample (see Figure 3.2) was fractured under liquid nitrogen (N_2) and then sputter-coated with a thin Iridium (Ir) layer using a high vacuum sputter coater (ACE 600, Leica Microsystems GmbH, Germany). The SEM images were used to further evaluate an area proportion of nano-SiO_2, agglomerate size of nano-SiO_2, and PBAT droplet size. At least three different areas were used for the SEM investigation.

To examine the dispersion and distribution of nano-SiO_2 in the PBAT phase, which forms a shape as droplets, a focused ion beam (FIB)-SEM (FEI Helios Nanolab™ 650, Thermo Fisher Scientific, USA) was carried out to cut the PBAT droplets. The acceleration voltage and ion beam current used for performing the cut were 2 kV and 0.1 nA, respectively. The FIB-SEM images were also used to investigate an area proportion of nano-SiO_2 in the PBAT droplets. At least ten droplets were cut for the FIB-SEM investigation.

3.3.2.1 Area Proportion and Agglomerate Size of Nanoparticles

A microscope imaging software (NIS-Elements BR 4.12, Nikon GmbH, Germany) was used to detect all of the observed areas, and then the area proportion of nano-SiO_2 located in PLA or PBAT phase to the total observed area ($A_{Si,PL}$ or $A_{Si,PB}$) was calculated according to equations (3.1) and (3.2). $A_{Si,PL}$ and $A_{Si,PB}$ were evaluated based on SEM images and FIB-SEM images, respectively. Figure 3.3 demonstrates schematic structures, which define parameters used in the calculation.

$$A_{Si,PL} = \frac{\sum_i a_{i,PL}}{A_T - \sum_i A_{i,PB}} \times 100\% \tag{3.1}$$

$$A_{Si,PB} = \frac{\sum_i a_{i,PB}}{A_{PB}} \times 100\% \tag{3.2}$$

where $a_{i,PL}$ is an area i of agglomerate nano-SiO_2 located in PLA phase, A_T defines the total observed area, and $A_{i,PB}$ is an area i of PBAT droplets, according to SEM images. From FIB-SEM images, $a_{i,PB}$ is an area i of agglomerate nano-SiO_2 located in PBAT phase and A_{PB} is the area of cross-sectional PBAT droplet.
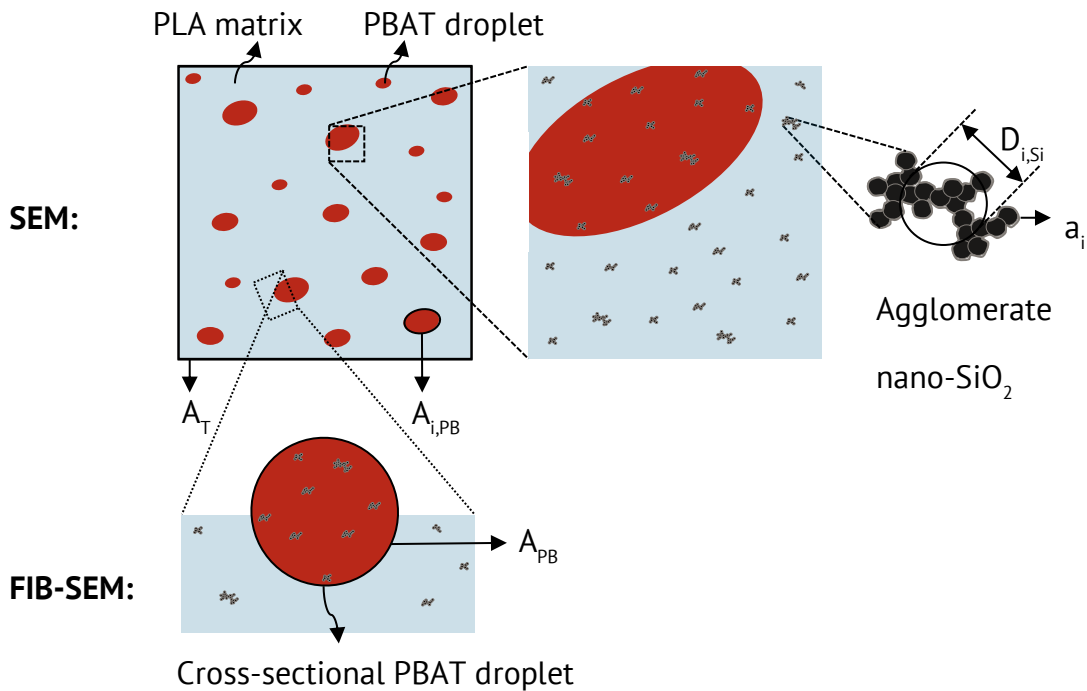
Figure 3.3:   Schematic structures for calculating the area proportion and average agglomerate size of nano-SiO_2.

In addition, the equivalent diameter of agglomerate nano-SiO_2 ($D_{i,Si}$) was automatically calculated from the corresponding area according to the following equation:

$$Equivalent\ diameter\ (D_i) = \sqrt{\frac{4 \times a_i}{\pi}}$$

(3.3)

A histogram was created to obtain a cumulative distribution. An average agglomerate size of nano-SiO_2 ($x_{50,2}$) is defined as the equivalent diameter at which 50th percentile of all the nanoparticles and the subscript number 2 is according to the measurement from the area perspective.

3.3.2.2 Dispersed Polymer Size

The average PBAT droplet size was analyzed by an image analysis software (ImageJ 1.52a, Wayne Rasband National Institutes of Health, USA). At least 300 PBAT droplets were determined per sample. The diameter of each droplet ($D_{i,PB}$) was calculated from the responding area ($a_{i,PB}$) using equation (3.3). The Schwartz-Saltykov correction [114] was applied for the fact that the observed droplets might not be cut exactly at their equator. The correction method is shown in Appendix E. After the correction, the number average diameter (D_n) and volume average diameter (D_v) of the PBAT droplets were calculated based on the following relation:

$$D_n = \frac{\sum_i n_i D_{i,PB}}{\sum_i n_i}$$

(3.4)

$$D_v = \frac{\sum_i n_i D_{i,PB}^4}{\sum_i n_i D_{i,PB}^3}$$

(3.5)

where n_i is the number of the droplets having diameter $D_{i,PB}$. The droplet size dispersity (d) is defined by d = D_v/D_n.

3.3.3   Surface Wetting Properties

To obtain surface and interfacial energies, contact angle measurements were carried out using a contact angle meter (G2/DSAII, Krüss GmbH, Germany). The measurements were performed on the sample surfaces of the prepared PLA and PBAT films. Before the testing,

all sample surfaces were cleaned with deionized (DI) water and isopropanol, and then dried in an oven at 80 °C for 24 h. A static drop of 2 µL was deposited on the sample surface using two different liquid probes (DI water and diiodomethane (CH_2I_2)) at room temperature (23 °C). The contact angle values are the average of at least ten measurements at different areas of the surfaces.

According to the Owens-Wendt approach [115] and Fowkes theory [116], the surface energy of each component can be calculated based on the relationships of the respectively following equations:

$$\gamma_l(1 + cos\theta) = 2(\gamma_s^d\gamma_l^d)^{\frac{1}{2}} + 2(\gamma_s^p\gamma_l^p)^{\frac{1}{2}} \tag{3.6}$$

$$\gamma_s = \gamma_s^d + \gamma_s^p \tag{3.7}$$

where γ_s and γ_l are the surface energies of solid and liquid, respectively. d and p are the dispersive and polar components, respectively. θ is the contact angle. The slope and interception of the plot between $\gamma_l(1+cos\theta)/2(\gamma_l^d)^{1/2}$ versus $(\gamma_l^p)^{1/2}/(\gamma_l^d)^{1/2}$ are $(\gamma_s^p)^{1/2}$ and $(\gamma_s^d)^{1/2}$, respectively. The surface energy values of the tested liquids used in the calculation are given in Table 3.6.

Table 3.6:   Surface energy values of the tested liquids [117]

Tested liquid	γ (mJ/m^2)	γ_l^d (mJ/m^2)	γ_l^p (mJ/m^2)
DI water	72.8	22.5	50.3
CH_2I_2	50.8	48.5	2.3

The surface energy at processing temperature (190 °C) were obtained by extrapolated using the temperature coefficients ($-d\gamma/dT$) of 0.06 mJ/m^{2}K [118] and 0.10 mJ/m^{2}K [119] for polymers and nano-SiO_2, respectively. The obtained surface energy values of neat PLA and PBAT, including nano-SiO_2 from the literature [111] were then used for calculation the interfacial energy (γ_{ij}) between two polymers using the Harmonic Mean approach [120]:

$$\gamma_{12} = \gamma_1 + \gamma_2 - 4\left[\frac{\gamma_1^d\gamma_2^d}{\gamma_1^d + \gamma_2^d} + \frac{\gamma_1^p\gamma_2^p}{\gamma_1^p + \gamma_2^p}\right] \tag{3.8}$$

and Geometric Mean approach [115] for calculation the interfacial energy between poly-mer and nano-SiO_2:

$$\gamma_{12} = \gamma_1 + \gamma_2 - 2\left[(\gamma_1^d\gamma_2^d)^{1/2} + (\gamma_1^p\gamma_2^p)^{1/2}\right] \tag{3.9}$$

3.3.4 Rheological Properties

The rheological properties of the polymer melts were performed at 190 ^{o}C under a nitro-gen atmosphere using a rotational rheometer (MCR 702, Anton Paar GmbH, Austria). A parallel plate geometry with 25 mm diameter and 1.5 mm thickness was equipped. The plate was pre-heated for 5 min before time sweep and strain sweep tests were conducted to monitor the thermal degradation of the polymers. According to the obtained results, frequency sweep tests were performed from 100 to 0.05 rad/s at a strain of 0.1 % for 40 min. Prior the testing, the materials were dried in an oven at 80 ^{o}C for 15 h.

3.3.5 Thermal Properties

3.3.5.1 Differential Scanning Calorimeter

A differential scanning calorimeter (DSC) (TA Q20, TA Instruments, Eschborn, Germany) equipped with a refrigerated cooling system unit (RCS90) was applied to determine the thermal properties of the materials. Prior testing, the melting temperature and enthalpy were calibrated using indium as a reference material. Each sample of 5−10 mg was placed between an aluminium pan and lid and tested under liquid nitrogen (N_2). All the samples were tested three times for the average values.

Non-Isothermal Characterization

To eliminate the thermal history, the samples were first heated to 200 ^{o}C at a rate of 10 K/min, and held at this temperature for 3 min. Subsequently, they were cooled down to −80 ^{o}C at a rate of 5 K/min and held for 3 min. The samples were again heated to 200 ^{o}C at a rate of 10 K/min. The crystallization temperature (T_c) and enthalpy of crystallization (ΔH_c) were corrected during the 1st cooling scan. The glass transition temperature (T_g), cold crystallization temperature (T_{cc}), melting temperature (T_m), and enthalpy of cold crys-

tallization and melting (ΔH_{cc} and ΔH_m) were corrected during the 2nd heating scan. Temperature data were collected from the peak positions of the obtained thermograms. The degree of crystallinity (X_c) was calculated according to the following equation [121]:

$$X_c = \frac{\Delta H_m - \Delta H_{cc}}{\Delta H_m^o \times f} \times 100\% \tag{3.10}$$

where ΔH_m^o is the heat of fusion of completely crystallized PLA (93 J/g) [122] and f is the mass fraction of the PLA.

Isothermal Characterization

For the isothermal investigation, the samples were also heated to 200 °C at a rate of 10 K/min and held at this temperature for 3 min. The samples were then quenched at a rate of 40 K/min to different crystallization temperatures (80–130 °C). The samples were kept isothermal at each temperature until the crystallization was complete.

3.3.5.2 Polarized Light Optical Microscope

A polarized light optical microscope (PLOM) (ECLIPSE LV100, Nikon GmbH, Düsseldorf, Germany) was used to investigate the development of supermolecular morphology. The microscope was equipped with a hot stage (LTS 420, Linkam, Surrey, England). The sample was prepared by using a thin film (see Figure 3.2) which was inserted between a microscope glass slide and a glass cover, then pre-heated and gently pressed on a hot plate at 200 °C for 3 min to eliminate air bubbles between the stack. The sample was then placed in the hot stage under the microscope and performed isothermal crystallization by heated the sample from room temperature to 200 °C at a rate of 10 K/min, held at this temperature for 3 min. Accordingly, the sample was cooled down at a rate of 20 K/min to two selected crystallization temperatures (110 °C and 130 °C) and kept constant until the complete of crystallization. The morphology was imaged during the isothermal condition.

3.3.5.3 Simulation of Injection Molding

To predict the cooling rates during the injection molding process, a commercial software package (Autodesk Moldflow 2016) was used in this work. The software generated the simulation of temperature gradient during the filling, cooling, and wrapping process in

injection molding. A numerical modeling data of a commercial PLA/PBAT blend (ecovio®
IS1335, BASF SE, Ludwigshafen, Germany) was used. The commercial blend has the same
blending ratio and the same PLA and PBAT grade materials used in this work. The 3D
model of the injection-molded plate was created by a CAD program (PTC Creo) and then
meshed by creating tetrahedral elements. The temperature distribution data were
corrected as a function of time at different thicknesses of the injection-molded plate from
the core area (center of the sample thickness) to the skin area (nearby the wall of cold
mold).

3.3.5.4 Flash Differential Scanning Calorimeter

A fast scanning or Flash differential scanning calorimeter (Flash DSC) (FLASH DSC 1,
Mettler Toledo, Gießen, Germany) was performed in this work to investigate the
crystallization behavior of the materials at very fast cooling rates. The calorimeter was
attached to a Huber Intracooler TC100 and purged with dry nitrogen gas at a flow rate of
35 mL/min. A thin film (see Figure 3.2) was cut into a small piece with a typical lateral
dimension of about 50 μm and placed directly on the chip sensor. The sample was first
heated to 200 °C at a heating rate of 1 K/s before the actual tests to provide a good
thermal contact to the sensor and to erase the thermal history of the sample. In this study,
the samples were heated to 200 °C at a heating rate of 1000 K/s and kept isothermal for
0.1 s. The samples were then cooled to −80 °C at various cooling rates according to the
simulation data. The selected cooling rates are in a range from 0.5 to 500 K/s. The
crystallization behavior was observed during the cooling scan. The more details regarding
the calorimeter and procedures are described in the literatures [123,124].

3.3.6 Mechanical Properties

3.3.6.1 Tensile Testing

The tensile properties of all the materials were investigated using a universal testing
machine (Zwick 1446, Zwick GmbH & Co. KG, Germany). An extensometer and a 10 kN
load cell were equipped for testing at a temperature of 23 ± 2 °C and a humidity of 50 ±
10 %. Dog-bone shaped samples according to DIN EN ISO 527−2/1BB were tested at the
crosshead speed of 1 and 50 mm/min for determining Young's modulus and tensile
strength, respectively. The average data were presented with at least eight measure-
ments.

3.3.6.2 Impact Testing

Charpy notched impact properties were determined using an impact testing machine (CEAST 9050 Impact Pendulum, Instron, USA) equipped with a 5J pendulum. The rectangle samples (50 x 6 x 4 mm^3) were milled for a U-notch according to DIN 53453. The tests were performed at 23 ± 2 °C temperature and 50 ± 10 % humidity. At least eight samples per material were tested for an average value. The U-notched impact strength (a_n) was calculated based on the following equation:

$$a_n = \frac{W}{b \cdot h} \tag{3.11}$$

where W is the impact energy absorbed by the samples. b and h are the width and height of the samples, respectively.

4   Results and Discussion

4.1   Morphology

It is well known that the multi-phase polymer nanocomposites can exhibit different mor-
phologies (i.e., droplets, fibers, co-continuous) and preferential locations of the nanopar-
ticles. High-resolution SEM is, therefore, used to characterize the morphology of the
nanocomposites. For comparison purposes, representative SEM micrographs of neat PLA
and PLA/PBAT-S0 are shown in Figure 4.1. The neat PLA displays a smooth and continu-
ous surface, while the addition of 20 vol.% PBAT shows a typical phase separation of the
immiscible blends. This phase separation is defined as a droplet or sea-island morpho-
logy. In this work, the main component, which is PLA, forms a continuous phase, so-called
polymer matrix, and the minor component, which is PBAT, forms a dispersed polymer
phase or droplets. An arrow at the right top of Figure 4.1(b) indicates the injection direc-
tion. It reveals that the orientation of PBAT droplets is parallel to the injection flow.
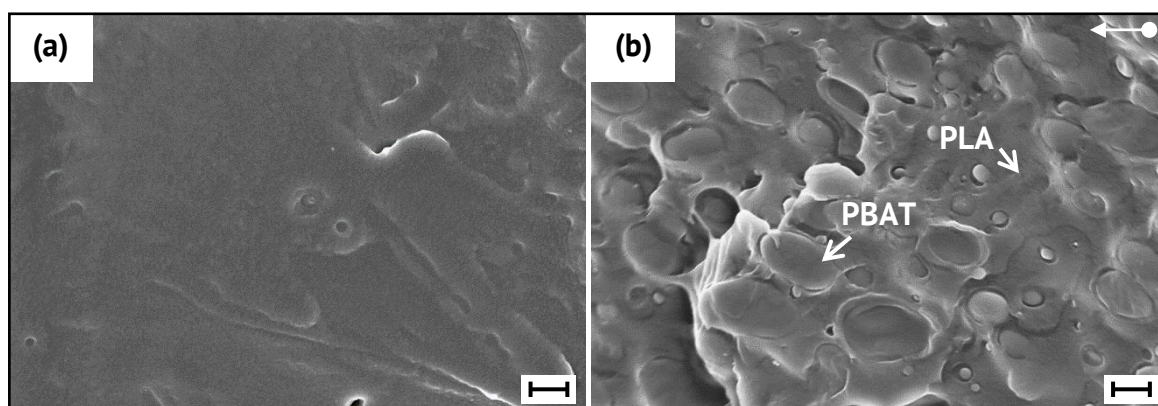
Figure 4.1:   SEM micrographs of fracture surfaces: (a) neat PLA and (b) PLA/PBAT-S0
(scale bar = 1 μm).

4.1.1   Location of Nanoparticles

As a dispersed nanofiller, 1 vol.% nano-SiO_2 was incorporated into the PLA/PBAT blend.
Figure 4.2 shows representative SEM micrographs of PLA/PBAT-based nanocomposites
with different processing procedures (i.e., P1 and P2 processed by PLA masterbatch (MB-
PLA), P3 and P4 processed by PBAT masterbatch (MB-PBAT)). The micrographs show that
the droplet morphology is also observed for all the nanocomposites. The cavities on the

continuous PLA phase are detected due to the detachment of the PBAT droplets, showing poor interfacial adhesion between the PLA and PBAT polymers. The agglomerate nano-SiO_2 is presented in the form of white dots.
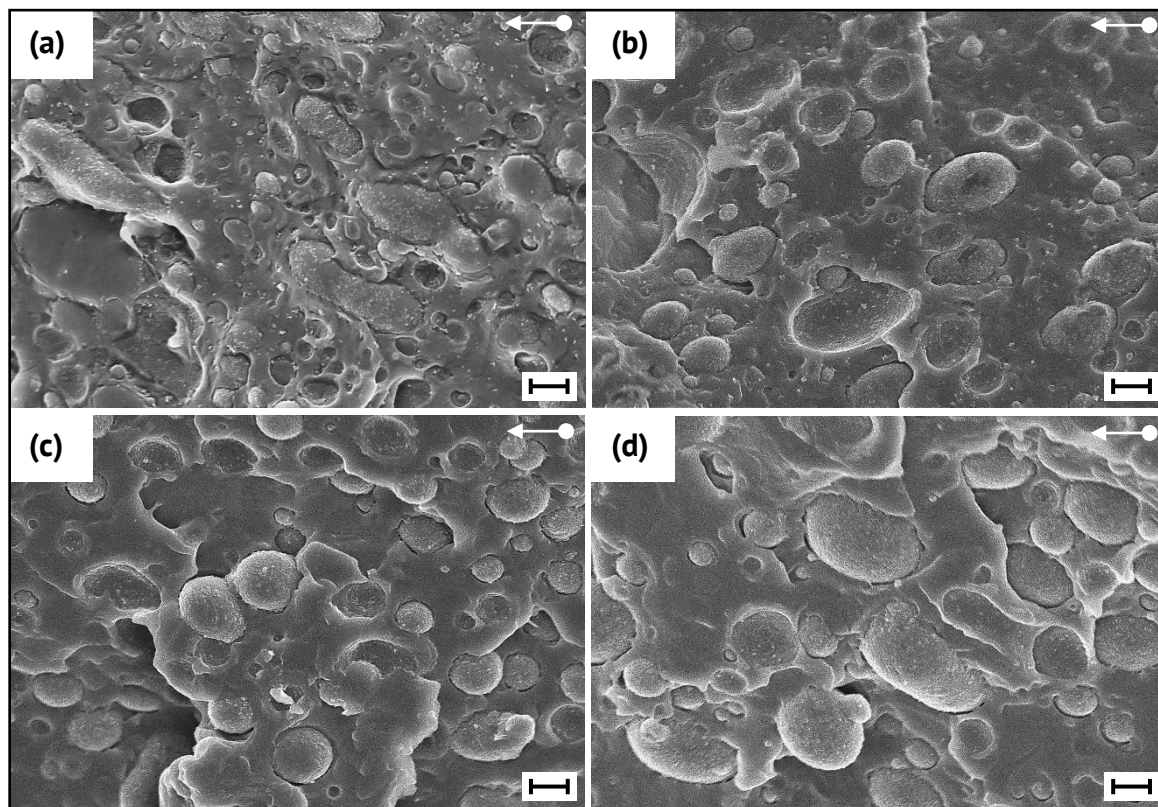
Figure 4.2:   SEM micrographs of fracture surfaces: (a) PLA/PBAT–S1-P1, (b) PLA/PBAT–S1-P2, (c) PLA/PBAT–S1-P3, and (d) PLA/PBAT–S1-P4 (scale bar = 1 μm).

For the dispersion of the nano-SiO_2, the nanoparticles are well dispersed in the continuous PLA phase and at the interface between the PLA and PBAT polymers (i.e., on the PBAT droplets and the cavities of the PLA phase) with the nanocomposites P1 and P2, as shown in Figures 4.2(a) and (b), respectively. In addition, using a two-step process P2, which means an increase in residence time, results in a lower concentration of nano-SiO_2 in the continuous PLA phase. This result implies that there is probably a migration process during the second-step extrusion. On the contrary, Figures 4.2(c) and (d) show that for the nanocomposites P3 and P4, the nano-SiO_2 could hardly be detected in the continuous PLA phase and were only present at the interface between the two polymers. Based on the SEM micrograph, it can be assumed that the nano-SiO_2 might be exclusively located in the PBAT phase and at the interface between the PLA and PBAT polymers when the MB-PBAT was used in the dilution process.

As seen in Figure 4.2, the cryo-fracture samples do not reveal the information of nano-SiO_2 dispersion in the dispersed PBAT phase because the breaking of the PBAT droplets is hardly detected. There is still a question regarding the location of nano-SiO_2 in the PBAT phase. Therefore, a FIB-SEM technique is applied to further investigate the dispersion of nano-SiO_2 inside the PBAT droplets. It should be mentioned that the FIB technique produces a beam of ions (usually gallium (Ga^+)) to mill the selected surface of samples [125]. In this case, the PBAT droplets are milled into a rectangular shape to obtain a cross-section of the droplets. Figure 4.3 depicts the FIB-SEM micrographs of all the nanocomposites. It illustrates the cross-sectional PBAT droplets with the agglomerate nano-SiO_2 as the boundary between the PLA matrix and PBAT droplets. In accordance with the FIB-SEM results, the micrographs reveal that there is only a small amount of the agglomerate nano-SiO_2 in the PBAT droplets in the nanocomposites P1 and P2, as seen in Figures 4.3(a) and (b). In contrast with the nanocomposites P3 and P4, a higher amount of nano-SiO_2 is detected inside the PBAT droplets (see Figures 4.3(c) and (d)). Therefore, the above assumptions that the nano-SiO_2 is mainly located in the continuous PLA phase and at the interface between the two polymers in the case of the nanocomposites P1 and P2 are confirmed. Also, it disperses particularly in the dispersed PBAT phase and at the interface in the case of the nanocomposites P3 and P4, accordingly.

Consequently, the results obtained from the SEM and FIB-SEM analyses verify the location of the nanoparticles. It can be concluded that the nano-SiO_2 is mainly located in the original polymer phase, in which it is first dispersed in the masterbatch process, and at the interface between the PLA and PBAT polymers. This behavior indicates that the processing procedure or the sequence of the mixing process (kinetic effect) has a tremendous influence on the location of the nano-SiO_2 in the PLA/PBAT-based nanocomposites.

As mentioned earlier, according to the two-step nanocomposite P2 prepared by MB-PLA, there is a phenomenon that is considered a migration process during the second-step extrusion. This phenomenon is identified by a smaller amount of nano-SiO_2 in the PLA phase when compared to the one-step nanocomposite P1. A similar trend is also observed in the two-step nanocomposite P4 prepared by MB-PBAT. As discussed above, the nano-SiO_2 is located in the PBAT phase and at the interface in the nanocomposites P3 and P4. Figure 4.3(d) reveals that the nanocomposite P4 also contains a relatively smaller amount of nano-SiO_2 in the PBAT droplets, indicating the migration process during the second-step extrusion. In order to evaluate the amount of nano-SiO_2 quantitatively, area proportions of nano-SiO_2 located in each phase compared to the total observed area are calculated. The measurement structure is described in section 3.3.2: Morphology. Figure 4.4

presents the area proportions of nano-SiO_2 located in the PLA phase or PBAT phase to the total observed area ($A_{Si,PL}$ or $A_{Si,PB}$, respectively). As expected, the calculated data not only confirm the preferential location of nano-SiO_2 in all the nanocomposites but also corroborate a reduction in the nano-SiO_2 of the nanocomposites using a two-step process. For both production methods (MB-PLA and MB-PBAT), there is a reduction in the nano-SiO_2 in its original phase of 46.3 % and 23.8 %, respectively. An explanation for the difference in the migration speed will be discussed in section 4.2: Rheological Properties.
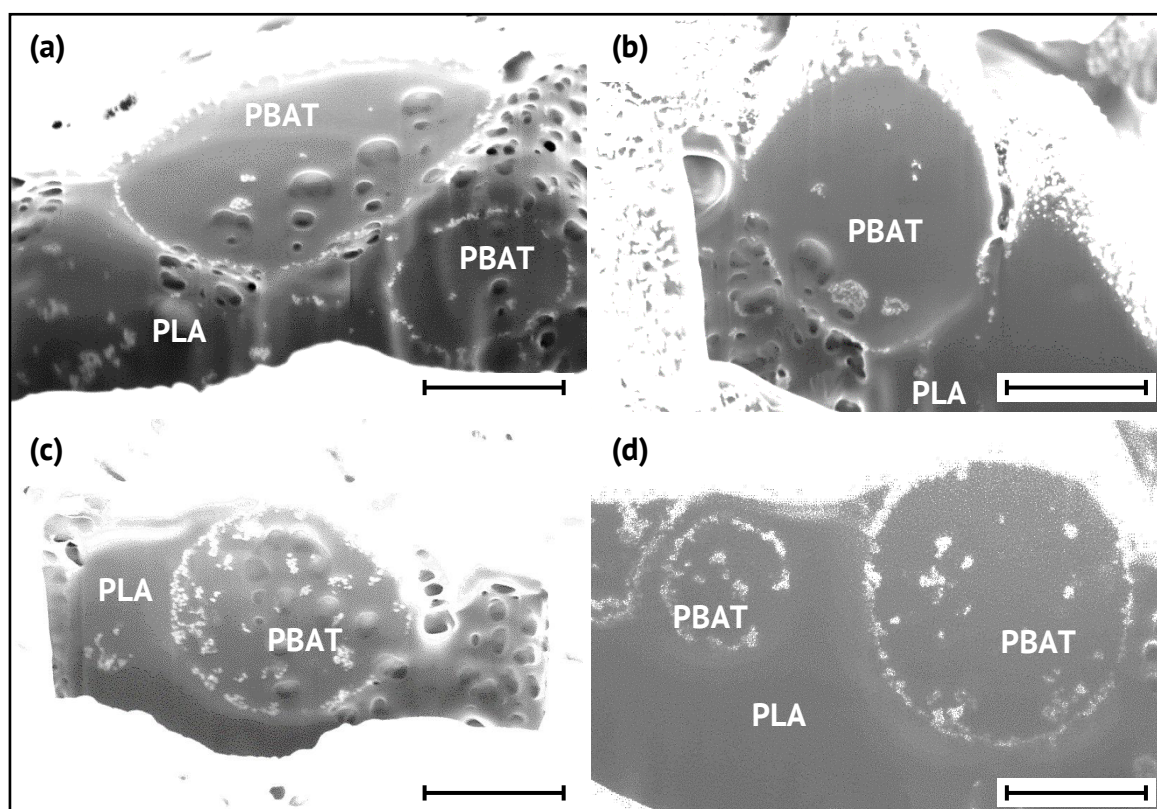
Figure 4.3:   FIB-SEM micrographs of cross-sectional PBAT droplets: (a) PLA/PBAT-S1-P1, (b) PLA/PBAT-S1-P2, (c) PLA/PBAT-S1-P3, and (d) PLA/PBAT-S1-P4 (scale bar = 1 μm).
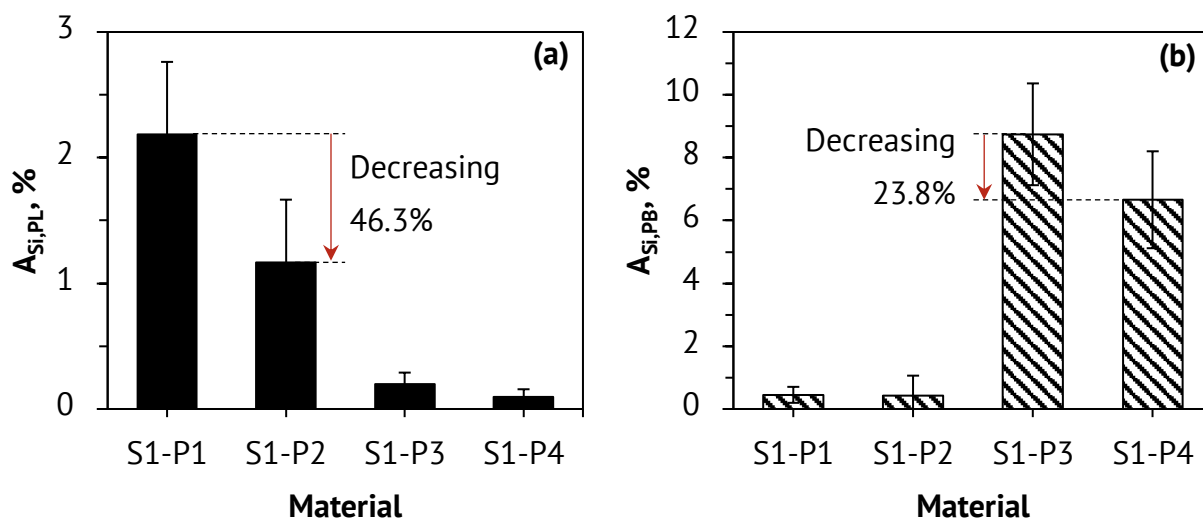
Figure 4.4:   Area proportion of nano-SiO$_2$ located in the (a) PLA phase (A$_{Si,PL}$) and (b) PBAT phase (A$_{Si,PB}$) to the total observed area (The data describe only the tendency of the A$_{Si}$ values in each phase. A$_{Si,PL}$ and A$_{Si,PB}$ cannot be quantitatively compared due to the use of different investigated instruments).

Furthermore, Figure 4.5 shows representative high-magnification SEM micrographs of the cavities on the continuous PLA phase of all the nanocomposites. It can be seen that the SEM micrographs reveal another piece of evidence of the migration of nano-SiO$_2$. The results show that by increasing the residence time in the extrusion, the nano-SiO$_2$ seems to travel from the PLA phase (in the case of nanocomposites P1 and P2) and the PBAT phase (in the case of nanocomposites P3 and P4) to the phase boundary between the two polymers. It is indicated by a higher amount of observed nano-SiO$_2$ on the PLA cavities (marked by the arrows) in the nanocomposites P2 and P4, as seen in Figures 4.5(b) and (d), respectively. Based on the analysis, it can be inferred that the nano-SiO$_2$ is preferentially located at the interface between the PLA and PBAT polymers. This will be further discussed in the next section 4.1.2: Wetting Parameters of Nanoparticle Location. Figure 4.6 illustrates the summary of the location of nano-SiO$_2$ in the PLA/PBAT-based nanocomposites using different processing procedures.

Apart from the migration to the polymer interface, the penetration behavior from one phase to another is also detected. This behavior will be discussed in section 4.1.3: Nanoparticle Size and Distribution.
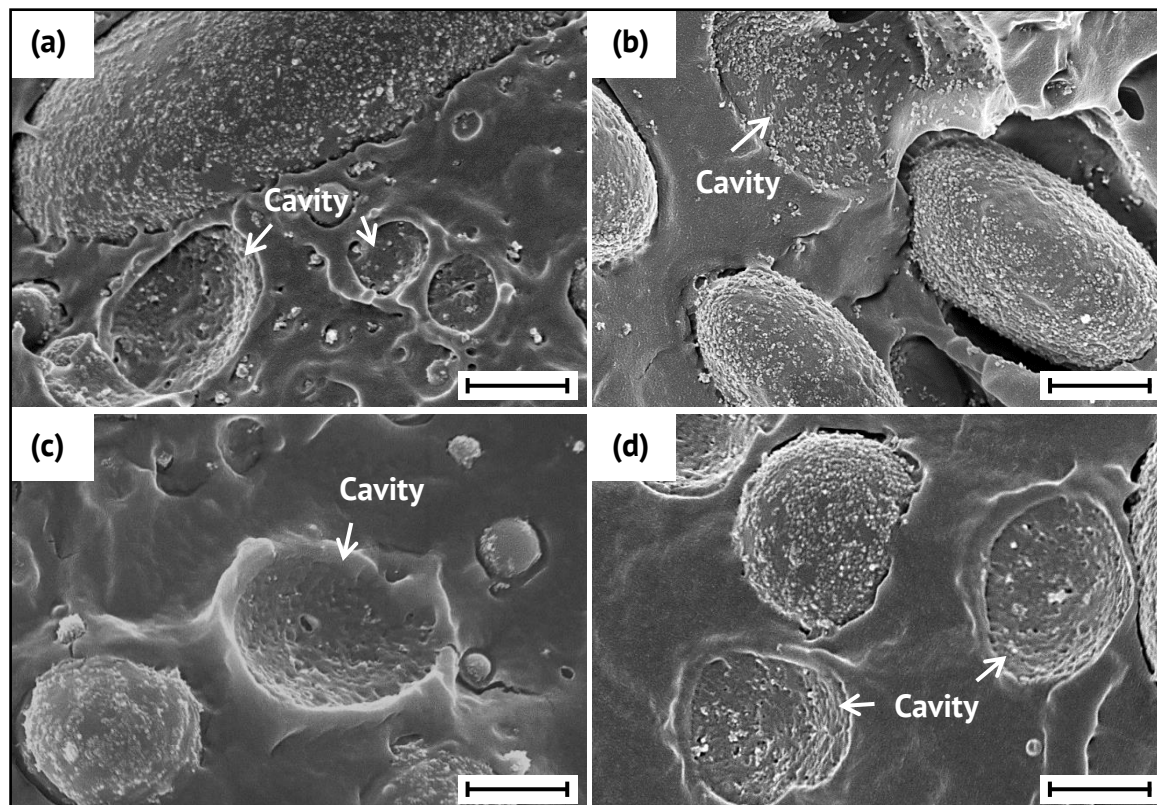
Figure 4.5:   SEM micrographs showing the cavities on the continuous PLA phase: (a) PLA/PBAT-S1-P1, (b) PLA/PBAT-S1-P2, (c) PLA/PBAT-S1-P3, and (d) PLA/PBAT-S1-P4 (scale bar = 1 μm).

S1-P1: 1-Step   S1-P2: 2-Step

MB-PLA:

S1-P3: 1-Step   S1-P4: 2-Step

MB-PBAT:

Continuous phase: PLA, Dispersed polymer phase: PBAT,

Dispersed nanofillers: Nano-SiO$_2$
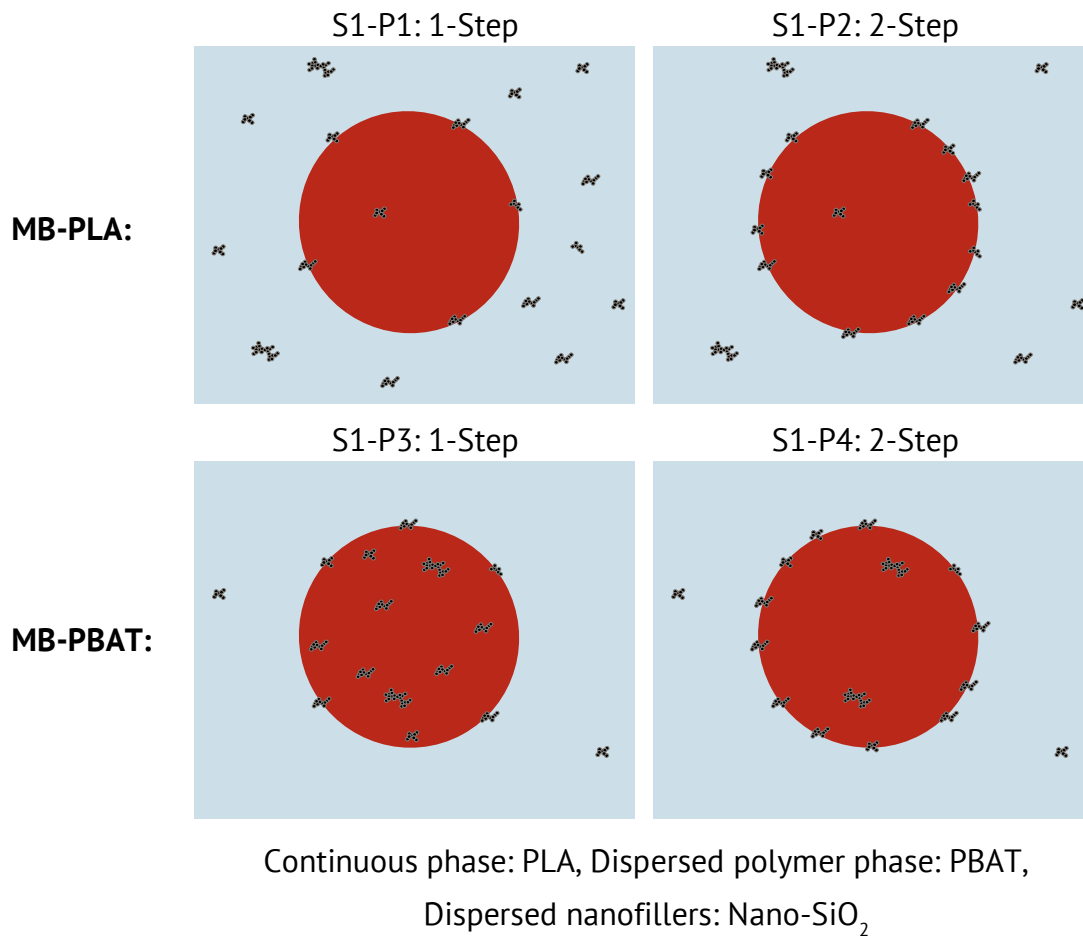
Figure 4.6:   Schematic representation of the location of nano-SiO$_2$ in the PLA/PBAT-based nanocomposites with different processing procedures.

4.1.2 Wetting Parameters of Nanoparticle Location

As discussed previously, the investigation of the location of nano-SiO$_2$ seems to not only depend on the processing sequence of the melts but also the residence time in the extrusion process. These parameters are defined as kinetic effects. It is also believed that the migration phenomenon could be due to the non-equilibrium thermodynamics of the nanoparticles. Therefore, the thermodynamic effect in terms of wettability is considered in this section.

In principle, the location of nanoparticles in immiscible blends can be predicted by estimating the affinity between the nanoparticles to each component of the polymer blends. The stabilization of interfacial energies between each component is applied to calculate the thermodynamic or wetting parameter (ω) based on Young's equation, as shown in the following equation [100]:

$$\omega = \frac{\gamma_{1s} - \gamma_{2s}}{\gamma_{12}} \qquad\qquad (4.1)$$

where γ_{1s}, γ_{2s}, and γ_{12} are the interfacial energies between polymer 1 and nanoparticles, polymer 2 and nanoparticles, and polymers 1 and 2, respectively. If ω is greater than 1 (ω > 1), the nanoparticles are located in polymer 2. The nanoparticles are located in polymer 1 when ω is less than -1 (ω < -1). For ω between -1 and 1 (-1 < ω < 1), the nanoparticles are located at the interface between polymers 1 and 2.

As seen in equation (4.1), the wetting parameter can be obtained from the interfacial energies (γ_{ij}) between each component in the nanocomposite system. Therefore, the relationships between contact angle and surface energy from the Owens-Wendt approach are applied [115]. The average values of the contact angle between the tested liquids and polymers and their corresponding surface energies of each component are listed in Table 4.1. After that, the interfacial energies can be calculated by using the obtained data. The calculated approaches are described in more detail in section 3.3.3: Surface Wetting Properties.

Table 4.1:   Contact angle and calculated surface energy of each component

| Material | Contact angle, ° | | Surface energy (γ), mJ/m^2 | | | | | |
| | | | At 23 °C | | | At 190 °C[b] | | |
	H_2O	CH_2I_2	γ	γ^d	γ^p	γ	γ^d	γ^p
PLA	86.8 ± 3.4	56.8 ± 5.0	32.1	26.1	6.0	22.0	17.9	4.1
PBAT	81.6 ± 4.0	58.9 ± 4.1	31.1	24.8	6.3	21.1	16.8	4.3
Nano-SiO$_2$[a]	–	–	32.0	30.0	2.0	15.5	14.5	1.0

[a]Surface energy of hydrophobic nano-SiO$_2$ at 25 °C is corrected from a literature [111].
[b]Linear extrapolated from the experimental values with a slope of $-d\gamma/dT$.

Based on the calculation, PLA and PBAT polymers are defined as polymers 1 and 2, respectively. The interfacial energy values are then given in Table 4.2. According to the result, the wetting parameter (ω) has a value of 0.01, indicating that the nano-SiO$_2$ is thermodynamically driven into the phase interface between the PLA and PBAT polymers. This is the main reason why the migration of the nanoparticles towards the interface is

pronounced in the nanocomposites P2 and P4, in which the double residence time is taken into account in the overall mixing process.

Table 4.2:   Calculated interfacial energy (γ_{ij}) and wetting parameter (ω)

Material pairs	Interfacial energy (γ_{ij}), mJ/m^2	Wetting parameter (ω)
PLA–PBAT (γ_{12})	0.04	
PLA–nano-SiO$_2$ (γ_{1s})	1.27	0.01
PBAT–nano-SiO$_2$ (γ_{2s})	1.27	

It is interesting to note that the processing procedures can control the location of nano-SiO$_2$ by first dispersing it into the desired phase. The nano-SiO$_2$ would be located either in the desired phase or at the interface. However, by increasing the processing or residence time, the migration process appears due to the thermodynamically preferred location of the nanoparticles. Therefore, in this work, both kinetic and thermodynamic effects play an important role regarding the location of nano-SiO$_2$ in the PLA/PBAT-based nanocomposites.

Besides the thermodynamic prediction, it is worth discussing the calculated interfacial energies (γ_{ij}) of each component pair, as reported in Table 4.2. The obtained data reveal that the interfacial energies of PLA–nano-SiO$_2$ (γ_{1s}) and PBAT–nano-SiO$_2$ (γ_{2s}) are higher than the interfacial energy between the PLA and PBAT polymers (γ_{12}). These results verify the distinct detachment behavior of the PBAT droplets in all the PLA/PBAT-based nanocomposites containing nano-SiO$_2$, as identified by the observed cavities on the continuous PLA phase (see Figure 4.5). The nano-SiO$_2$ located at the interface between the PLA and PBAT polymers acts as the repulsive force, promoting the de-bonding phenomenon between the two polymers. Meanwhile, the PLA/PBAT-S0 blend shows a mostly droplet breaking behavior during the cryo-fracture (see Figure 4.1(b)). It should be noted that a lower interfacial energy results in a stronger interaction between the component pair.

4.1.3   Nanoparticle Size and Distribution

It is generally known that the incorporation of nanofillers into polymer blends leads to an improvement in the final performance of the materials. However, the added fillers, especially in the nanoscale, usually form aggregations and/or agglomerations, which can

define their capability to enhance the material properties. To achieve a greater understanding of the nano-SiO_2 size and distribution in the PLA/PBAT-based nanocomposites, the agglomerate size of nano-SiO_2 is measured. As aforementioned, the nanoparticles disperse at different locations (i.e., continuous PLA phase, dispersed PBAT phase) depending on the processing procedure. The average agglomerate sizes of nano-SiO_2 in both PLA and PBAT phases ($x_{50,2,PL}$ and $x_{50,2,PB}$, respectively) are, therefore, determined as described in section 3.3.2: Morphology.

Figure 4.7 shows the agglomerate size distribution of nano-SiO_2 located in the PLA and PBAT phases, and Table 4.3 presents the average agglomerate size in each polymer phase with the migration direction of the nanoparticles. As mentioned earlier, most of the nano-SiO_2 are located in the PLA phase for the nanocomposites P1 and P2. The nanocomposite P1 shows an average agglomerate size of 76.2 nm, while the nanocomposite P2, with an increase in residence time, exhibits an average agglomerate size of 60.3 nm. The smaller agglomerate size can be due to the de-agglomeration of nanoparticles during the extrusion process. It is worth noting that the de-agglomeration mechanism is generally divided into three steps: i) the wetting process of the agglomerates by the polymer melt, ii) penetration of the polymer melt into the agglomerates, and iii) adequate mechanical force to break up the agglomerates [126]. It is also interesting to point out that there are induced stresses (shear and elongational flow) during the twin-screw extrusion process. These stresses cause the de-agglomeration of nanoparticles inside the screw channel [96]. Therefore, those are the possible reasons to gain a double degree of de-agglomeration, promoting the relatively smaller agglomerate size of nano-SiO_2 in the nanocomposites with a two-step extrusion. A comparison of the distribution curves also shows a narrow distribution of nano-SiO_2 agglomerates located in the PLA phase with a lower probability of an agglomerate size over 140 nm in the nanocomposite P2. The results are in good agreement with previous studies [96,127–129].

Furthermore, the agglomerate size of nano-SiO_2 located in the PBAT phase will also be discussed. For the nanocomposites P1 and P2, it should be mentioned that the nano-SiO_2 is dispersed later in the PBAT phase. Therefore, besides the migration of nano-SiO_2 from the PLA phase to its preferred location (interface), the penetration from one phase to another is also detected. In other words, the nanoparticles penetrate from the PLA matrix to the PBAT droplets. Therefore, a small amount of nano-SiO_2 agglomerate in the PBAT droplets is observed (see Figures 4.3 and 4.4). These existing agglomerates are from the penetrating phenomenon. Before further discussion, it is worth mentioning the migration

behavior of nanoparticles, which has three involved mechanisms, as reported by Elias et al. [106].
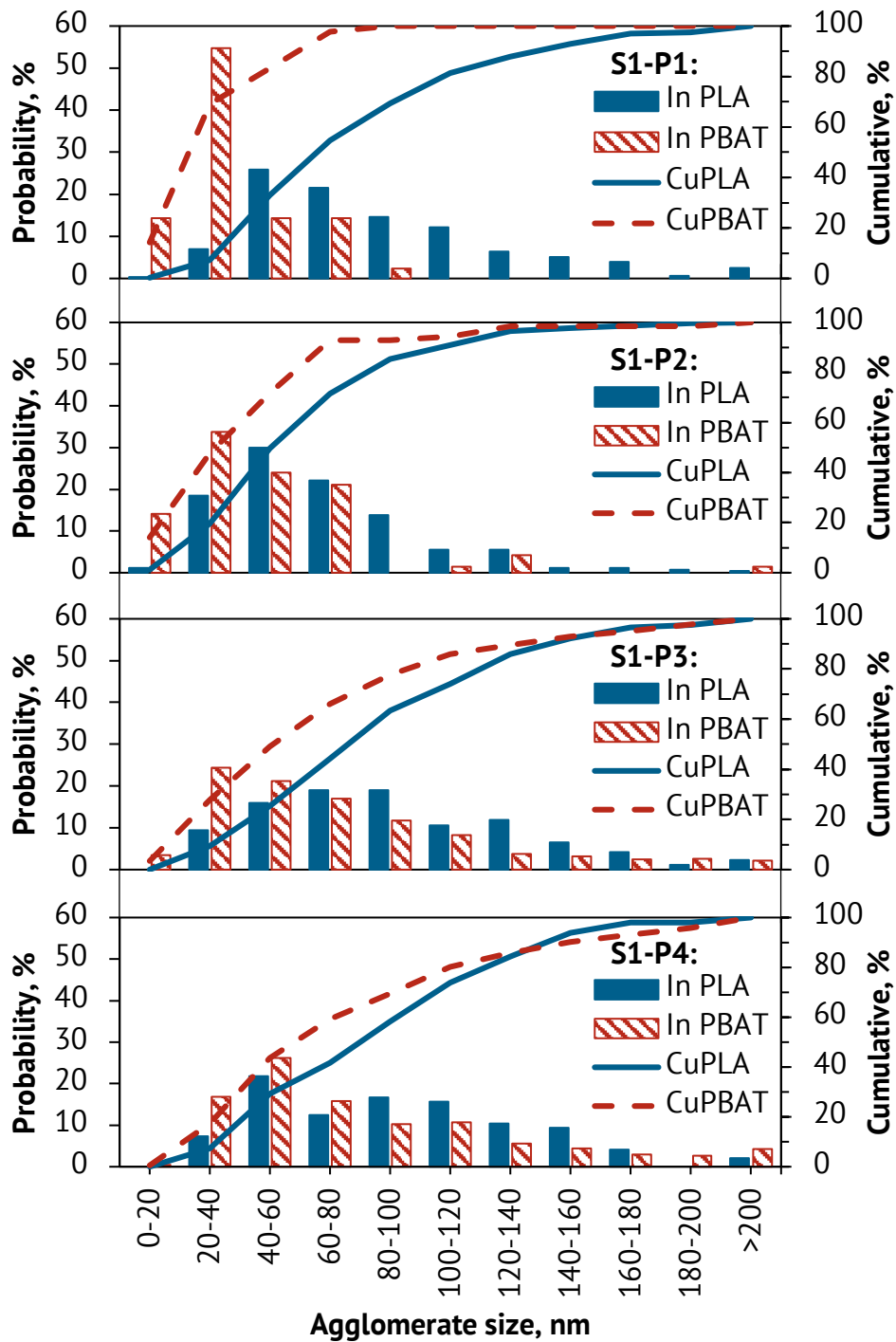
Figure 4.7:   Agglomerate size distribution of nano-SiO_2 located in the continuous PLA phase and dispersed PBAT phase.

Table 4.3:   Average agglomerate size of nano-SiO$_2$ in the PLA and PBAT phases ($x_{50,2,PL}$ and $x_{50,2,PB}$) and migration direction from one phase to another

Material	$x_{50,2,PL}$ or $x_{50,2,PB}$, nm		
	In PLA phase	Migration direction	In PBAT phase
PLA/PBAT-S1-P1	76.2	$\rightarrow$	31.1
PLA/PBAT-S1-P2	60.3	$\rightarrow$	41.7
PLA/PBAT-S1-P3	85.0	$\leftarrow$	61.4
PLA/PBAT-S1-P4	90.0	$\leftarrow$	68.9

The first mechanism is the self-diffusion of nanoparticles, the so-called Brownian motion. It can be described by the diffusion coefficient (D_0) of a spherical particle of radius a, as shown in equation (4.2).

$$D_0 = \frac{k_B T}{6\pi \eta_s a} \qquad (4.2)$$

where k_B is the Boltzmann's constant (1.38×10^{-23} J/K) and η_s is the liquid viscosity at temperature T. Accordingly, the required time (t_D) for a particle to diffuse a distance equal to its radius a can be estimated by the following equation:

$$t_D = \frac{a^2}{D_0} = \frac{6\pi \eta_s a^3}{k_B T} \qquad (4.3)$$

In this case, if we define the characteristic data as 34–nm radius a of an agglomerate nano-SiO$_2$, 72.6 Pa·s for PLA viscosity ($\eta_{s,PL}$), and 640.2 Pa·s for PBAT viscosity ($\eta_{s,PB}$) at a temperature T of 463.2 K (see in section 4.2: Rheological Properties), the calculated t_D values for both PLA and PBAT are, respectively, about 8 s and 74 s. The residence time of twin-screw extruders is usually only a few minutes. Based on the experimental data, the dilution process in the twin-screw extruder has a residence time of 3.28 min (see Appendix F). This means that a nano-SiO$_2$ agglomerate is diffused by Brownian motion in a dilution process with only a distance of ~839 nm in the PLA melt and ~94 nm in the PBAT melt. Therefore, the Brownian motion of nanoparticles is barely accounted for during the extrusion process.

The second mechanism is the shear-induced migration. During mixing, random collisions frequently take place between the drifting particles and the dispersed or droplet component. The frequency of collisions (C) can be roughly estimated by the following equation [83,106,130]:

$$C = \frac{8}{\pi}\dot{\gamma}\phi \tag{4.4}$$

where $\dot{\gamma}$ is the shear rate and ϕ is the volume fraction of the considered dispersed entity. The numerous collisions may cause nanoparticles to be embedded in the droplets. A similar mechanism can be applied to explain when the nanoparticles embed in the droplets and tend to migrate forward to the interface and finally to the matrix phase because of the velocity field inside the droplets [99,106].

The third mechanism involves the coalescence process. The collision between two droplets leads to the trapping process of nanoparticles inside the droplets [106]. The trapping mechanisms of nanoparticles are illustrated in Figure 4.8. First, droplets travel by shear- or flow-induced migration during the melting process. The two droplets approach each other and eventually collide with one of the droplets, adsorbing nanoparticles/agglomerates at the equilibrium droplet surface. Finally, the coalescence process takes place and traps the nanoparticles inside the newly formed droplet if the wettability between the nanoparticles and the droplet phase is in a proper condition [131]. However, this is not an ideal process because the nanoparticles commonly influence the morphology stabilization. The collision of polymer droplets in the polymer emulsion is very high; therefore, the contribution of this mechanism should be taken into account.

Based on the three involved migration mechanisms, the nano-SiO_2 particles travel through the PLA phase to the PBAT phase most likely due to the shear-induced migration and trapping process during the coalescence of the droplets. As shown in Table 4.3, the average agglomerate sizes in the PBAT phase are 31.1 nm and 41.7 nm, respectively, for the nanocomposites P1 and P2. The observed agglomerates are relatively smaller than those in the PLA phase. As discussed above, the movement of nanoparticles is influenced by more than Brownian motion, in which the boundary is dominated by the Peclet number (Pe), as described below [99].

$$Pe = \frac{\eta_s \dot{\gamma} a^3}{k_B T} \propto \dot{\gamma} t_D \tag{4.5}$$

According to this relationship, the nanoparticle size (a) and the required time (t_D) for nanoparticles to move are directly proportional. This means that a smaller agglomerate moves faster than a bigger one. In addition, the viscosity of polymer melts also plays an essential role in either the migration behavior or the agglomerate size of nano-SiO_2, which will be discussed in section 4.2: Rheological Properties.
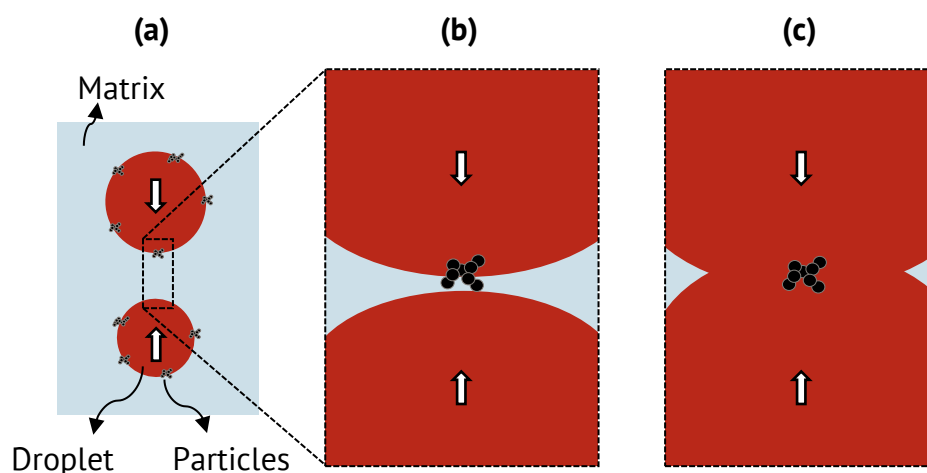
Figure 4.8: Schematic diagrams of the trapping mechanisms of nanoparticles: (a) shear- or flow-induced migration of droplets, (b) collision between two droplets, and (c) nanoparticle trapping process during the coalescence (adapted from [131]).

In the case of nanocomposites P3 and P4, the main location of nano-SiO_2 is in the PBAT droplets. As listed in Table 4.3, the nano-SiO_2 particles have average agglomerate sizes of 61.4 nm and 68.9 nm in the main-located phase, respectively. The results reveal that the agglomerate sizes are relatively smaller than those of nanocomposite P1 in their main-located phase ($x_{50,2,PL}$ = 76.2 nm). The possible reason can be explained by the difference in viscosity between the two polymers, which will be discussed later. Moreover, by using a two-step process, the re-agglomeration is generated in the nanocomposite P4 instead of the de-agglomeration in the two-step nanocomposite P2. The re-agglomeration might be explained by the fact that the free volume in the dispersed PBAT droplets is comparatively smaller than the continuous PLA matrix. Therefore, the probability of nanoparticle collisions, including the PBAT droplets, is higher. The induced stresses from the extruder play a less essential role than the cohesive forces. As a result, a longer residence time results in the development of re-agglomeration of nano-SiO_2 inside the PBAT droplets [132]. The same phenomenon can also be applied when the agglomerate size of

nano-SiO_2 located in the PBAT droplets ($x_{50,2,PB}$) increases from 31.1 nm in nanocomposite P1 to 41.7 nm in nanocomposite P2 (see Table 4.3).

The penetration behavior traveling from the PBAT droplets to the PLA matrix is also observed. The involved mechanism is most probably governed by the shear-induced migration of the nano-SiO_2. In contrast to the nanocomposites P1 and P2, the nano-SiO_2 shows larger agglomerate sizes after traveling and penetrating to another polymer phase (continuous PLA matrix). A small amount of the agglomerates located in the PLA phase have average agglomerate sizes of 85.0 nm and 90.0 nm in the nanocomposites P3 and P4, respectively. This behavior might be attributed to the thermodynamic affinity or wettability between the PLA polymer and nano-SiO_2, including the relatively low viscosity of the PLA melt (see section 4.2: Rheological Properties) [133]. Table 4.2 also reveals that the interfacial energy between PLA and nano-SiO_2 (γ_{1s}) is relatively high, revealing the incompatibility between the pair. It is believed that the combination of those parameters results in a more dominant role of the cohesive forces among the nanoparticles, leading to the re-agglomeration of nano-SiO_2 during the migration to the PLA phase.

Furthermore, because the processing sequence is studied in this work, there are step-1 compounds from the nanocomposites P2 and P4 (so-called Pre-P2 and Pre-P4, respectively) that can further be associated with the behavior of nanoparticle distribution. It should be noted that the nanocomposites Pre-P2 and Pre-P4 are, respectively, the diluted PLA/SiO_2 and PBAT/SiO_2 nanocomposites before blending with a second polymer, as seen in Figure 3.1. Therefore, the nanocomposites Pre-P2 and Pre-P4 as well as their masterbatches (MB-PLA, MB-PBAT) are examined by SEM. Representative SEM micrographs are shown in Figure 4.9. As a result, the MB-PLA reveals a surface corrugation and voids can be observed, indicating a relatively brittle material (see Figure 4.9(a)). In contrast, MB-PBAT shows a comparatively smoother surface with ductile deformation, as shown in Figure 4.9(b). In addition, it is obvious from the SEM images that both masterbatches depict a high degree of agglomeration and contain interlocking and network structures among the agglomerate nano-SiO_2. Thus, the average agglomerate size cannot be measured for both masterbatches.
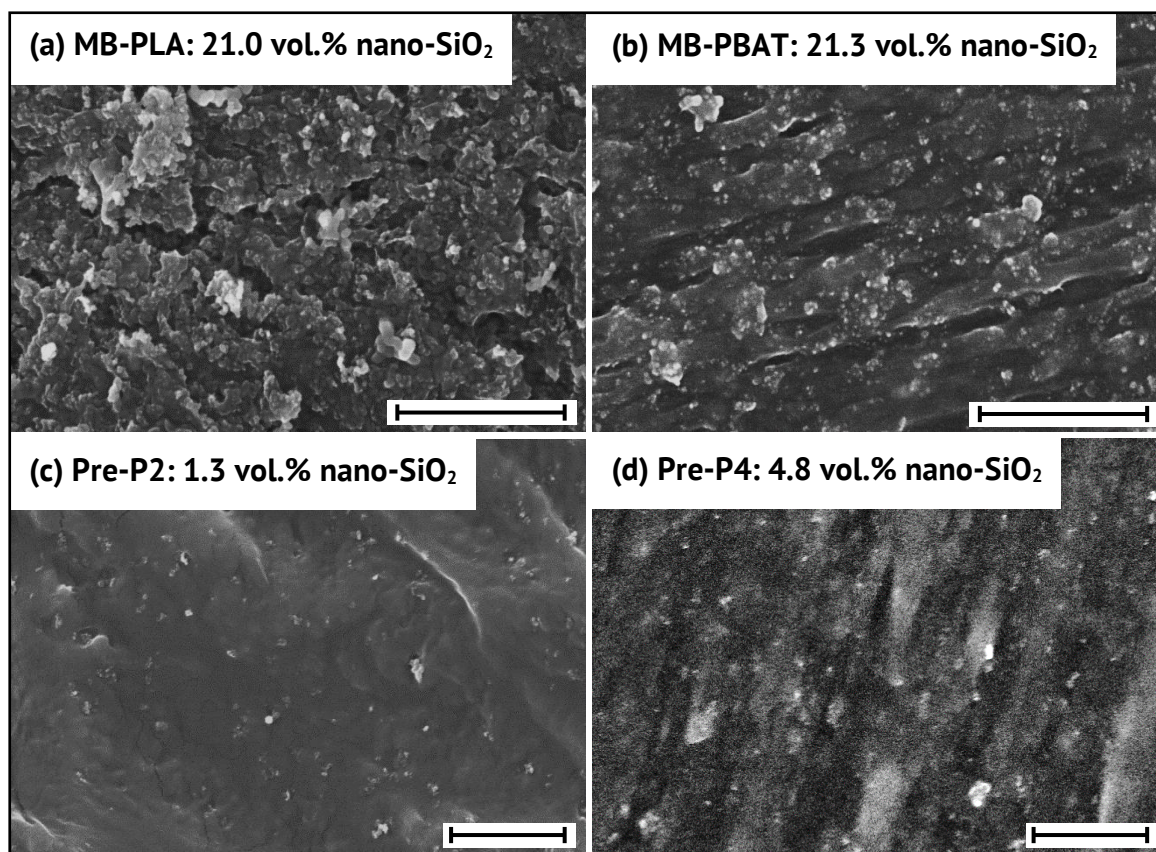
Figure 4.9   SEM micrographs of fracture surfaces: (a) MB-PLA, (b) MB-PBAT, (c) Pre-P2, and (d) Pre-P4 (scale bar = 1 μm).

The dispersion of nano-SiO_2 in the nanocomposites Pre-P2 and Pre-P4 is shown in Figures 4.9(c) and (d), respectively. It is clear that the diluted nanocomposites have relatively smaller nano-SiO_2 agglomerates that are well distributed in the respective matrices. Figure 4.10 illustrates the agglomerate size distribution and average agglomerate size of nano-SiO_2 of the Pre-nanocomposites. According to the obtained results, it can be inferred that the addition of a second polymer is another reason for the creation of relatively larger agglomerates. Despite the identical residence time, the nano-SiO_2 agglomerate size increases with the presence of more than one polymer component during compounding. It is evident that the nanocomposites Pre-P2 and Pre-P4 present smaller average agglomerate sizes of 51.7 nm and 43.8 nm ($x_{50,2,PL}$ and $x_{50,2,PB}$), respectively, when compared to the nanocomposites P1 and P3 containing two polymer components with the same residence time. This phenomenon is observed regardless of the type of polymer matrix. Figure 4.11 summarizes the average agglomerate sizes of nano-SiO_2 of the observed polymers in each processing step. The observed polymer phases of MB-PLA and MB-PBAT systems are in PLA and PBAT phases, respectively.

As mentioned earlier, several parameters play an essential role in the nanoparticle distribution for the PLA/PBAT-based nanocomposites filled with nano-SiO_2 in terms of both de-agglomeration and re-agglomeration.
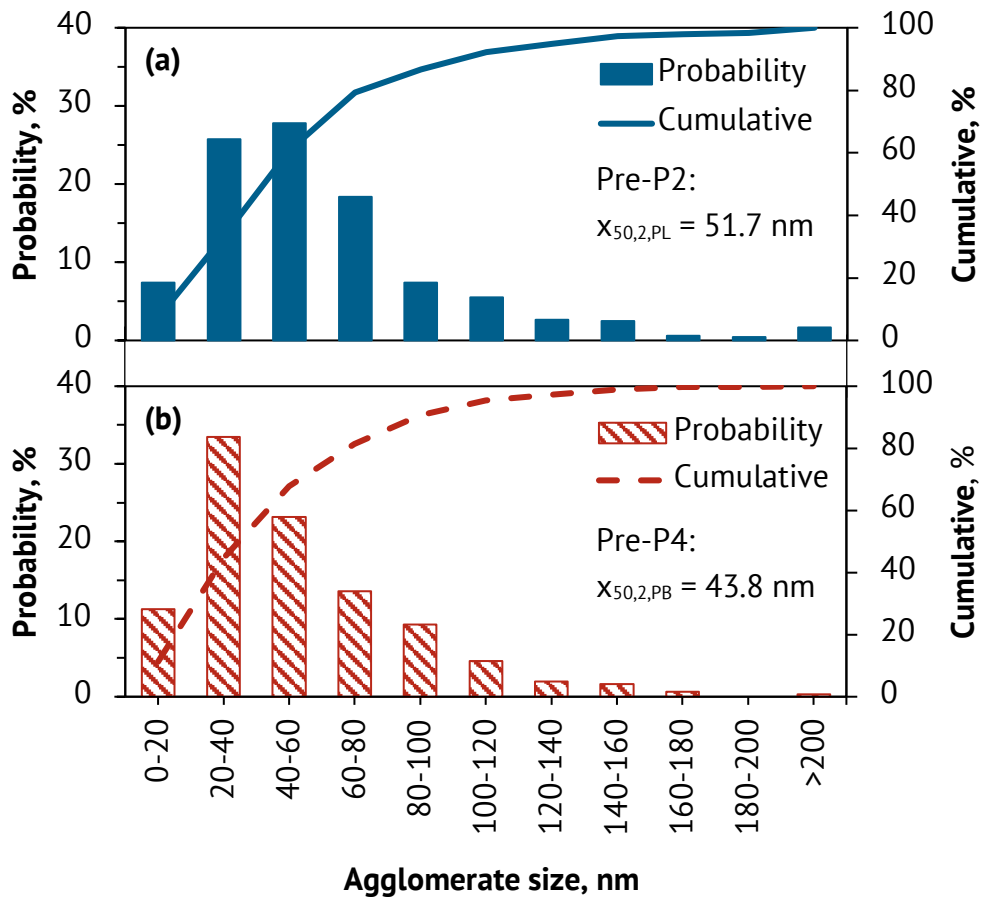
Figure 4.10:   Agglomerate size distribution and average agglomerate size ($x_{50,2}$) of nano-SiO_2: (a) Pre-P2 and (b) Pre-P4.
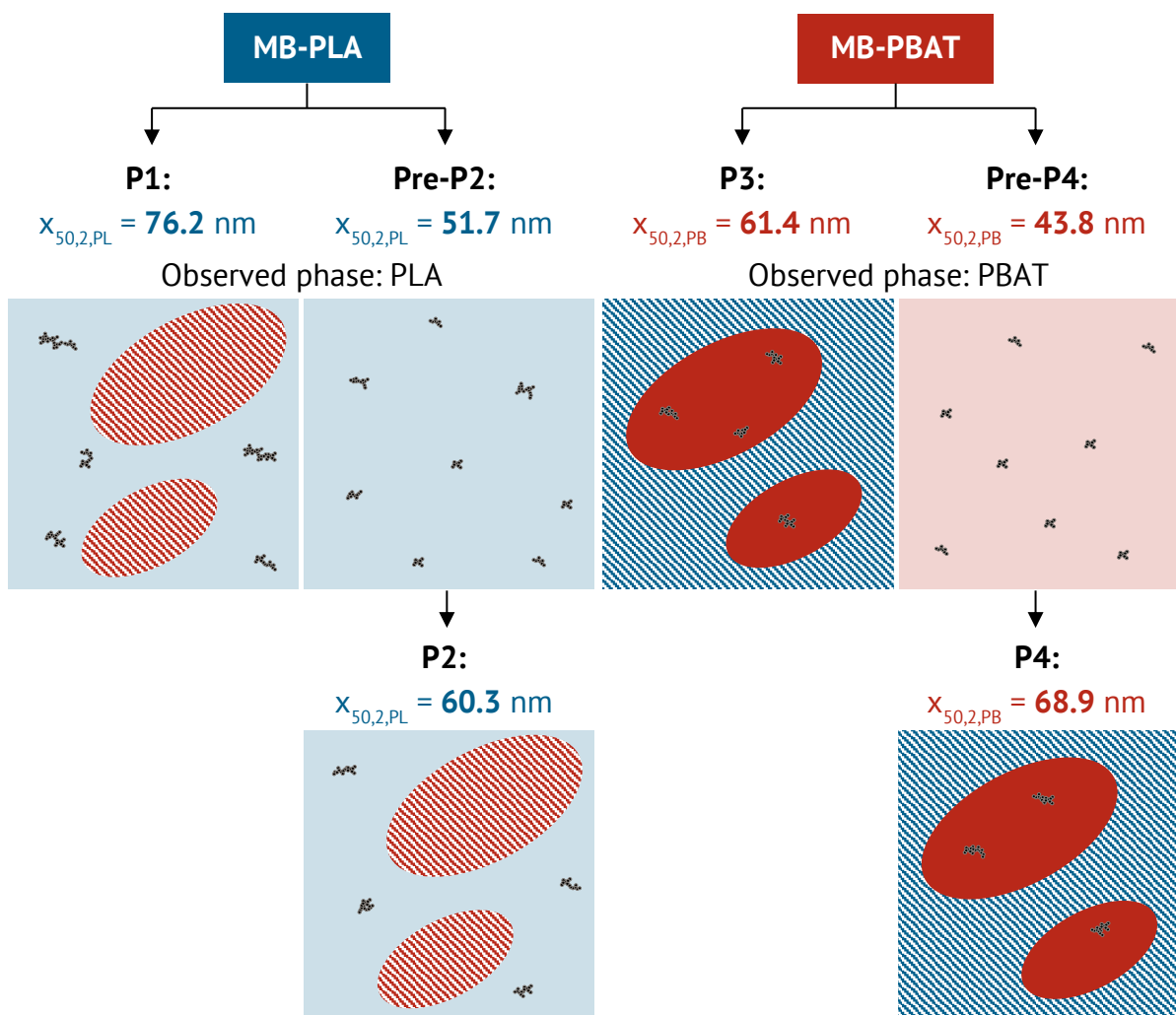
Figure 4.11:   Schematic diagrams summarizing the average agglomerate sizes ($x_{50,2}$) of nano-SiO$_2$ of the observed polymers in each processing step.

4.1.4   Dispersed Polymer Size and Distribution

One of the most important properties of the immiscible blends is the morphology stabilization between the matrix phase and the dispersed polymer phase (or in this case, the droplet phase). A fine and homogenous distribution of the dispersed polymer phase facilitates the improvement in the final properties of the blends (i.e., mechanical performance). In this work, nano-SiO$_2$ particles are incorporated into the immiscible PLA/PBAT-based nanocomposites to examine their effect on the average size of the droplet phase.

In general, the addition of nanoparticles can play major roles in the droplet size. Two possible phenomena are proposed: (i) suppressing the coalescence process of the droplet phase when the nanoparticles are stabilized at the interface and (ii) favoring the break-

up of the droplet phase due to the change in the viscosity ratio or viscoelasticity between the two polymers [14,47,134–137].

For comparison, the droplet size distribution curves of PBAT droplets before and after the Schwartz-Saltykov correction are shown in Figures 4.12 and 4.13, respectively. The correction method is shown in Appendix E. Figure 4.14 shows a diagram of the number average diameter (D_n), volume average diameter (D_v), and droplet size dispersity (d = D_v/D_n) of the dispersed PBAT droplets. The result shows that PLA/PBAT-S0 has a number average diameter of 0.96 μm. The incorporation of nano-SiO_2 slightly increases the number average diameter in the range of 1.11–1.33 μm. On the other hand, the volume average diameter decreases significantly in all the nanocomposites. This reduction results in a marked decrease in the droplet size dispersity, indicating the greater stability of the phase morphology of the PLA/PBAT-based nanocomposites. Furthermore, the volume average diameters show an increase in both the two-step nanocomposites P2 and P4, which is probably due to the second coalescence in step-2 of the extrusion process, but they are still lower than the PLA/PBAT blend (S0). Therefore, it can be concluded that the addition of nano-SiO_2 into the PLA/PBAT systems might not completely suppress the coalescence process and/or promote the break-up of the PBAT droplets, but it certainly enhances the morphology stabilization of the nanocomposites. Particularly, the one-step nanocomposite P3 prepared by MB-PBAT shows rather low number and volume average diameters of the PBAT droplets. This leads to the best balance of the average droplet size, resulting in the lowest droplet size dispersity, which is closer to 1. In other words, a finer and more homogeneous morphology is achieved in the nanocomposite P3 where most nanoparticles are distributed inside the dispersed polymer phase and at the interface and have inadequate time for the second coalescence. In this case, it can be assumed that this is owing to the droplet break-up by Taylor [77], the so-called, capillary number (Ca), as described by equation (2.12) [53]. If the capillary number is greater than the critical number (Ca >> Ca_{cr}) where the shear stress predominates over the interfacial stress, the droplet break-up is generated. Although the viscosity ratio ($\eta_r = \eta_d/\eta_m$) is quite high (see section 4.2: Rheological Properties), the break-up is unlikely to occur [99,138]. It is worth mentioning that the Taylor study is applied to describe, in particular, a single Newtonian drop in the simple shear flow [62,77]. Indeed, the polymer blend nanocomposite is more complex. As mentioned before, there is a large number of collisions during processing. The high concentration of nano-SiO_2 inside the PBAT droplets builds up shear stress and eventually can lead to the break-up of the droplets.
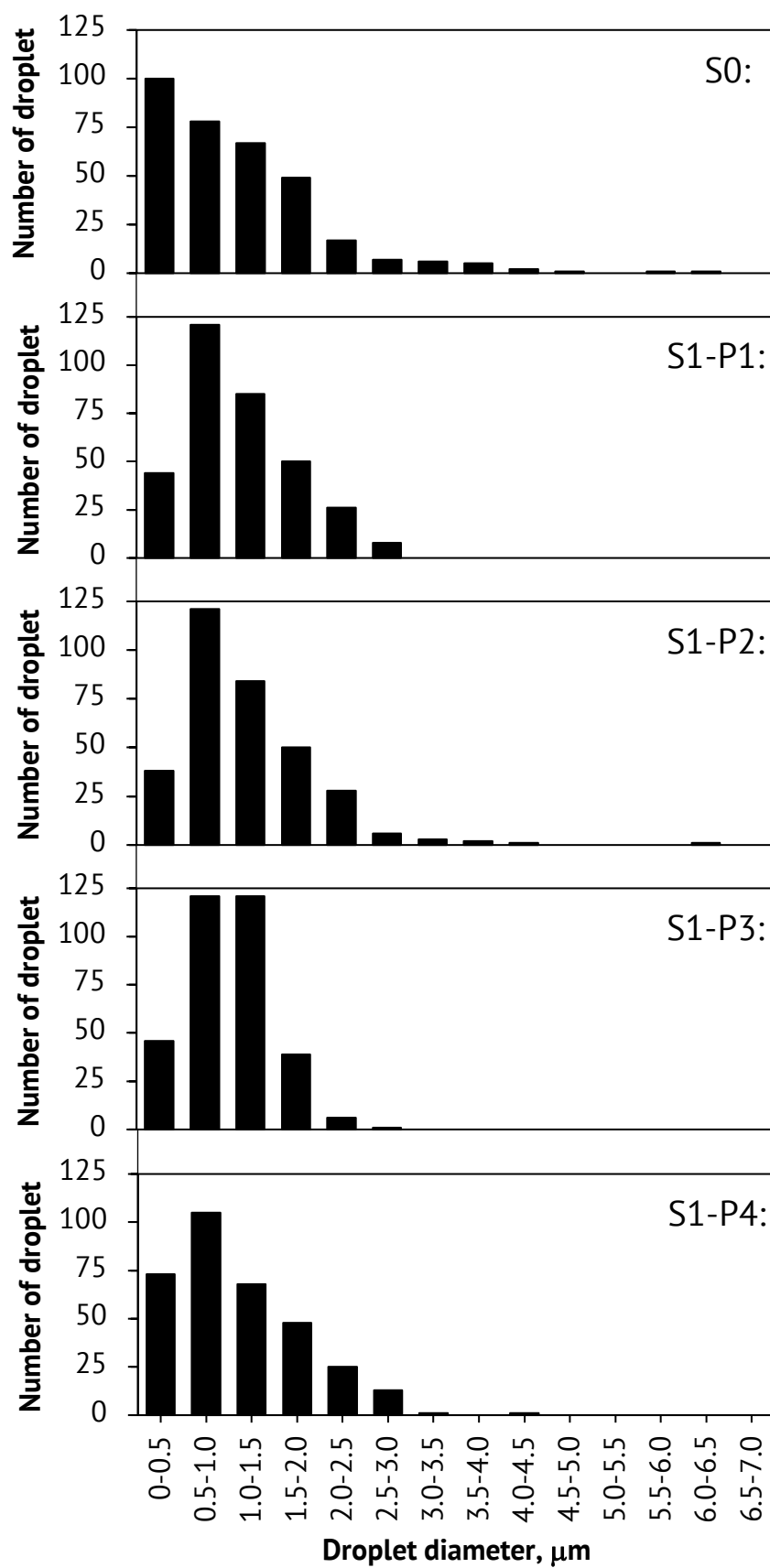
Figure 4.12: Droplet size distribution curves of PBAT droplets before the Schwartz-Saltykov correction.
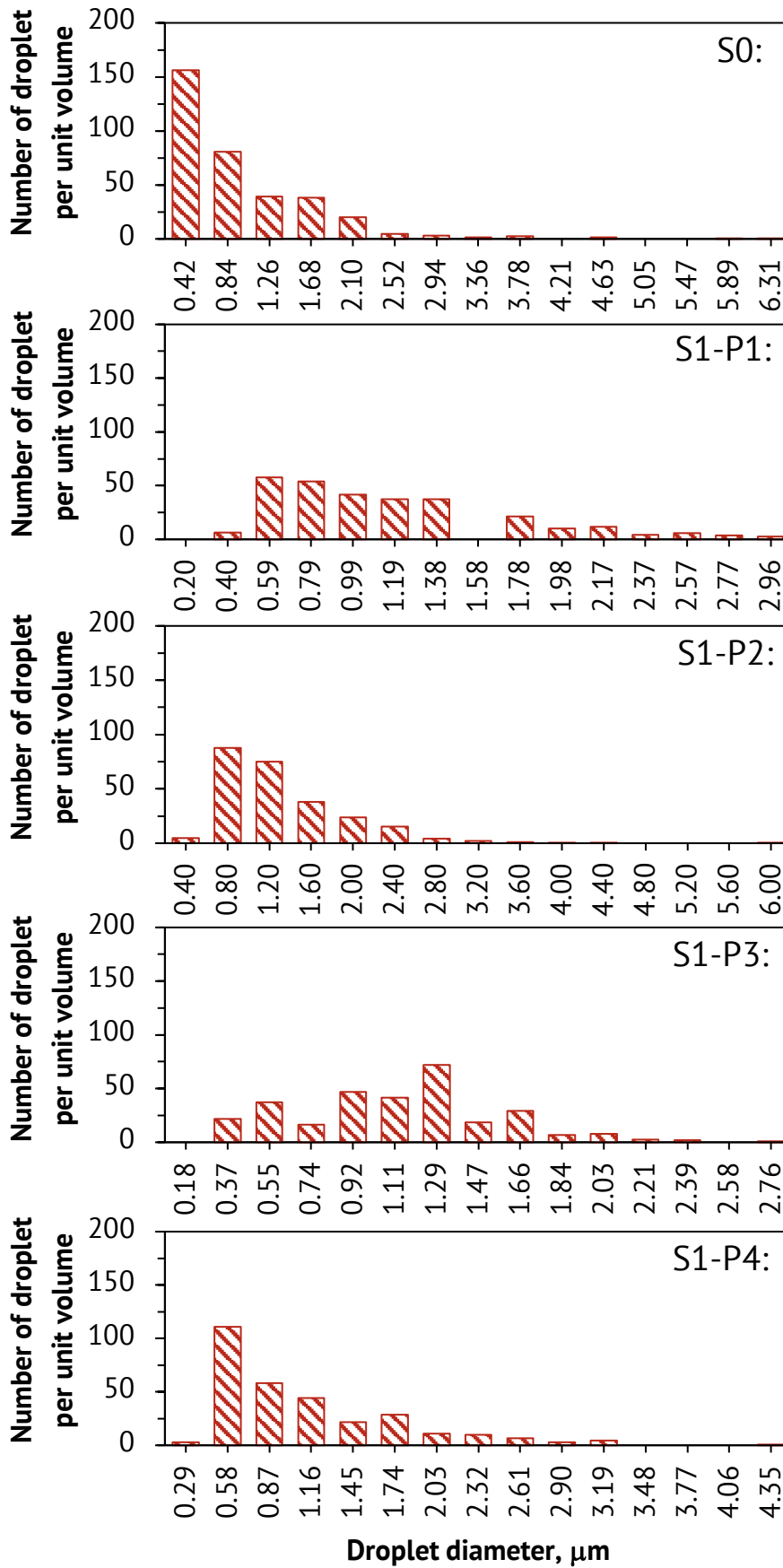
Figure 4.13:   Droplet size distribution curves of PBAT droplets after the Schwartz-
Saltykov correction.
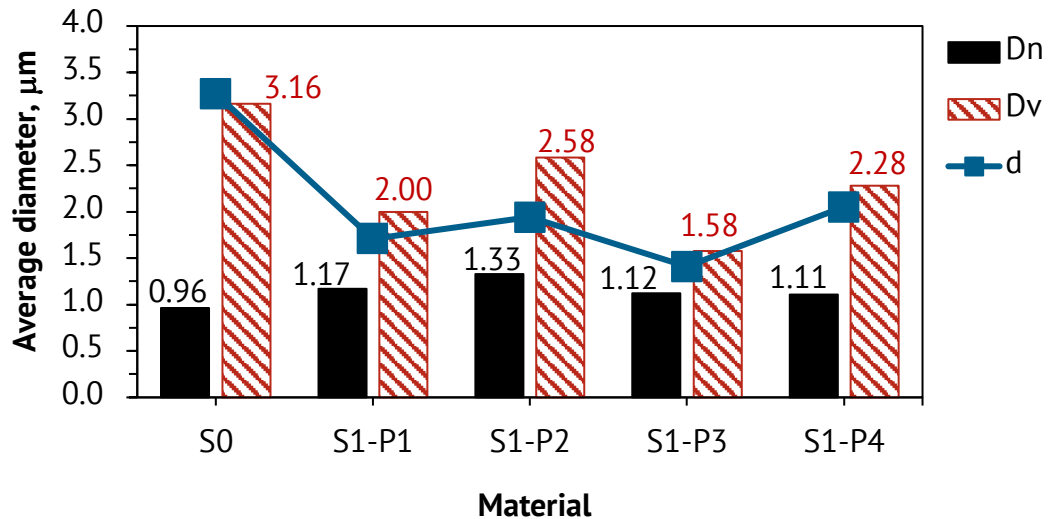
Figure 4.14:   Diagram of number average diameter (D_n), volume average diameter (D_v), and droplet size dispersity (d) of the PBAT droplets.

It is worth mentioning that Wu [139] proposed the matrix ligament thickness or interparticle distance (τ) to describe the brittle to tough transition in rubber toughening. The interparticle distance is related to the dispersed polymer size and volume fraction, as given by the following equation:

$$d = \tau \left[k (\frac{\pi}{6\phi_r})^{1/3} - 1 \right]^{-1} \qquad (4.6)$$

where d is the average diameter of the rubber polymer, k is a geometric constant (i.e., k = 1 for cubic lattice, $2^{1/3}$ for body-centered lattice, and $4^{1/3}$ for face-centered lattice), and ϕ_r is the volume fraction of the rubber polymer. To achieve a high toughness system, the interparticle distance must be lower than the critical interparticle distance (τ_c). At a given droplet volume fraction, a narrow droplet size distribution (droplet size dispersity closer to 1) is advantageous for toughening a polymer blend because the interparticle distance is reduced with a smaller droplet size [139].

4.2   Rheological Properties

Investigating the rheological properties of molten materials can assist in the understanding of the morphology formation (i.e., droplet and nanofiller sizes) because the morphology of the polymeric material can evolve during processing under shear flow. First,

time sweep tests were carried out to investigate the thermal stability during the rheological characterization. The complex viscosity (η^*) was normalized to its initial value (t = 0 s). Figure 4.15 shows the normalized complex viscosity ($\eta^*/\eta^*_{t=0s}$) as a function of time of neat PLA (PL), neat PBAT (PB), PLA/PBAT blend (S0), and PLA/PBAT-based nanocomposites (S1-P1, S1-P2, S1-P3, S1-P4). It can be seen that all materials besides nanocomposite P1 show a significant thermal degradation indicated by a decrease in complex viscosity over time. This thermal degradation is caused by unzipping depolymerization, random main-chain scission, and intramolecular and intermolecular transesterification [6,140–142]. The thermal degradation leads to a decrease in molar mass and an increase in mobility of the polymer chains, resulting in a reduction in the viscosity [141,142]. On the other hand, the complex viscosity of nanocomposite P1 slightly increases in the initial stage and then decreases insignificantly after passing a maximum. The observed behavior can be explained by the fact that the thermal stability of nanocomposite P1 is enhanced by the presence of nano-SiO$_2$. This conclusion is in good agreement with the literature [143,144]. As discussed earlier in section 4.1.1: Location of Nanoparticles, nano-SiO$_2$ is mainly located in the PLA phase, which is a major component and has a harsh thermal degradation compared to the neat PBAT. Therefore, the role of nanoparticles become more pronounced for improving the thermal stability in the nanocomposite P1.
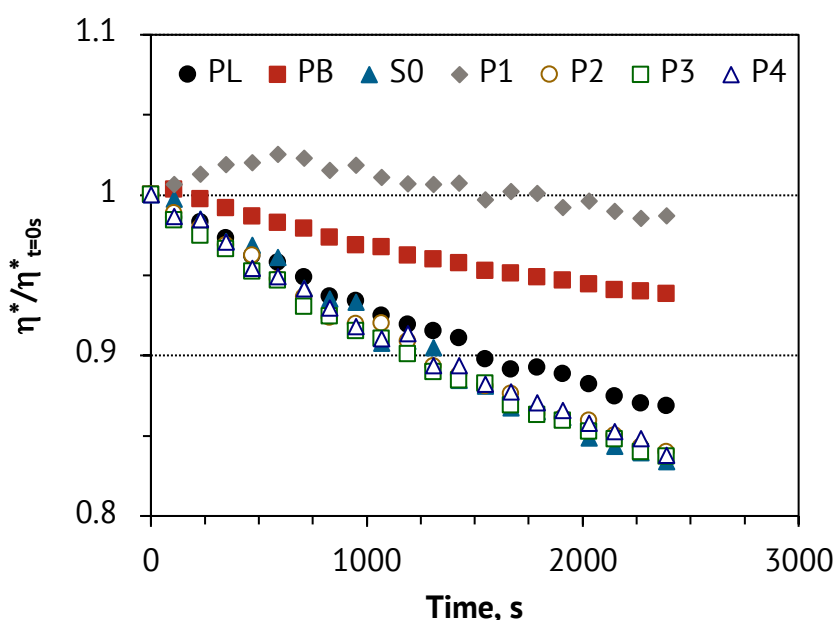
Figure 4.15:   Normalized complex viscosity ($\eta^*/\eta^*_{t=0s}$) as a function of time of neat PLA (PL), neat PBAT (PB), PLA/PBAT blend (S0), and PLA/PBAT-based nanocomposites (S1-P1, S1-P2, S1-P3, S1-P4).

Figure 4.16 illustrates the frequency sweep results by showing curves of complex viscosity as a function of angular frequency (ω) of all the materials. According to the Cox-Merz rule, the complex viscosity as a function of angular frequency is equivalent to the steady shear viscosity (η) as a function of shear rate ($\dot{\gamma}$) [145]. On the one hand, neat PLA, neat PBAT, and PLA/PBAT blend show a maximum instead of a horizontal plateau at low frequency. This behavior is due to the thermal degradation. It is important to note that the viscosity measurement initially starts at high frequency to low frequency. Therefore, the decrease in complex viscosity is observed at low frequency with a longer testing time. On the other hand, the addition of nano-SiO_2 leads to an upturn shift at low frequency. This behavior is known as a yield point, in which an interlocking or a 3D structure of nanoparticles is formed that restricts the mobility of the macromolecules in the molten polymers [36,89,146]. Similar behavior has been reported in other works [15,89,147]. Furthermore, the upturn shift behavior can also refer to the shape relaxation of the dispersed PBAT phase [15,148]. As expected, the nanocomposite P1 presents a very high yield point due to the high concentration of nano-SiO_2 in the polymer matrix (PLA phase). For nanocomposite P4, the high yield point can also be observed, although the nanoparticles are mostly dispersed in the dispersed PBAT phase and at the interface between the PLA and PBAT polymers. This phenomenon might be due to (i) large agglomerate sizes of nano-SiO_2 in both PLA and PBAT phases (90 nm and 68.9 nm, respectively) and (ii) a high degree of droplet size dispersity (d) [148]. The obtained results lead to the confined movement in the polymer matrix. Furthermore, all the nanocomposites exhibit shear thinning at low frequency, whereas the neat polymers and the blend (S0) display shear thinning at a higher frequency. Despite the fact that the shear thinning behavior in the neat PLA is unclear to be observed, which is due to the probable overlapping of the thermal degradation or the range of the investigated angular frequency being too short.

As seen in Figure 4.16, the complex viscosity of neat PBAT is approximately ten times higher than that of neat PLA. The obtained data provide the explanation of why the average agglomerate size of nano-SiO_2 in the dispersed PBAT phase is significantly smaller than the agglomerate size in the continuous PLA matrix ($x_{50,2,PB} < x_{50,2,PL}$), as shown in Table 4.3. It is noteworthy to mention that the maximum separating force (F_{max}) is proportional to the polymer viscosity, as given by equation (4.7) for shear flow and equation (4.8) for elongational flow in the twin-screw extruder [96,126]. Therefore, it can be inferred that the agglomerate nano-SiO_2 in the PBAT phase is confronted by more forces (shear and elongation) during melt processing and then acquires a higher degree of de-agglomeration.

$$F_{max} = 3\pi\eta\dot{\gamma}d^2 \tag{4.7}$$

$$F_{max} = 6\pi\eta\dot{\varepsilon}d^2 \tag{4.8}$$

where η is the polymer viscosity, $\dot{\gamma}$ and $\dot{\varepsilon}$ are the shear rate and shear strain, respectively, and d is the particle diameter.
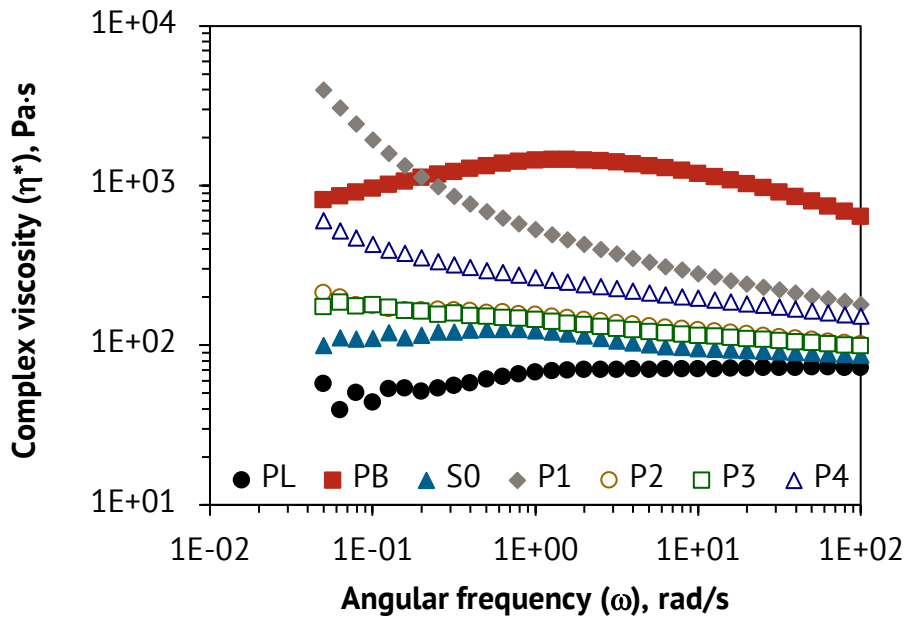
Figure 4.16:   Complex viscosity (η^*) as a function of angular frequency (ω) of neat PLA (PL), neat PBAT (PB), PLA/PBAT blend (S0), and PLA/PBAT-based nanocomposites (S1-P1, S1-P2, S1-P3, S1-P4).

The similar results are also related to the migration speed of the nano-SiO_2, as noted in Figure 4.4. The decrease in the nano-SiO_2 concentration is 46.3 % in the PLA phase (nanocomposites P1 to P2) and 23.8 % in the PBAT phase (nanocomposites P3 to P4). The nanoparticles travel faster in the PLA phase compared to the PBAT phase owing to the less restrained movement in a lower viscous polymer. In addition, the complex viscosity of the blend and its nanocomposites is in between those of the two neat polymers, following the simple rule of mixtures, except for the nanocomposite P1 at low frequency, which is due to the high formation of the nanoparticle network in the polymer matrix, as discussed earlier. All those nanocomposites exhibit a frequency–dependent behavior, as seen in Figure 4.16.

The rheological response of the storage modulus (G′) against the angular frequency of all the materials is illustrated in Figure 4.17. As one can see, the storage modulus of the blend and all nanocomposites behaves similar to the complex viscosity. The presence of nano-SiO_2 enhances the modulus of the melts, indicating the reinforcing effect. In particular, the storage modulus of nanocomposite P1 strongly increases in the low-frequency region, showing a solid-like behavior. This behavior can be attributed to filler–filler and filler–polymer interactions in the polymer matrix.
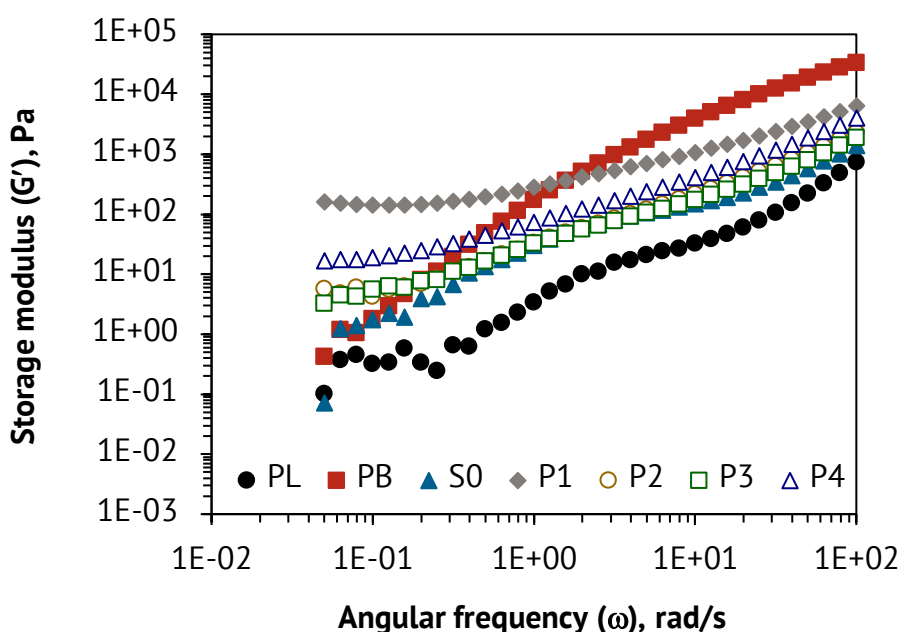
Figure 4.17:   Storage modulus (G′) as a function of angular frequency (ω) of neat PLA (PL), neat PBAT (PB), PLA/PBAT blend (S0), and PLA/PBAT-based nanocomposites (S1-P1, S1-P2, S1-P3, S1-P4).

Based on the rheological data, the so-called Han plot is an approach to obtain the miscibility and morphology of polymer blends and nanocomposites [149,150]. The storage modulus (G′) is plotted versus the loss modulus (G′′) in the log-log scale, as shown in Figure 4.18(a). The polymer blend is considered to be miscible at a molecular level when an identical slope is detected with an individual pair of neat polymers [151]. Otherwise, it is immiscible. The obtained results show that the PLA/PBAT blend and PLA/PBAT/SiO_2 nanocomposites are immiscible, as confirmed by the SEM investigation. The presence of nano-SiO_2 decreases the degree of miscibility, as indicated by a smaller slope, especially for the nanocomposites P1 and P4 (see Figure 4.18(a)), whereas the nanocomposites P2

and P3 are almost identical. In other words, the miscibility of the nanocomposites is dependent on the nanoparticle–location. It is known that the storage and loss moduli represent the elastic and viscous behaviors of the viscoelastic materials, respectively. Therefore, a line of G′ = G″ defines the transition from the elastic to viscous behavior and vice versa. According to Figure 4.18(a), all the materials show predominantly viscous behavior, although the elastic aspect remarkably increases with the incorporation of nano-SiO_2, resulting in an enhancement in the melt strength of the nanocomposites [152].
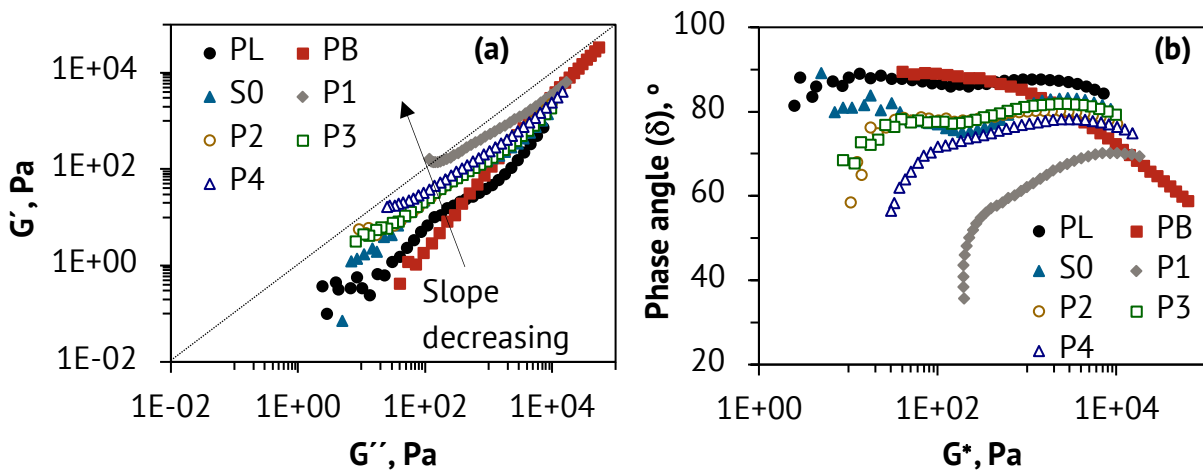
Figure 4.18:   (a) Han plots and (b) van Gurp–Palmen plots of neat PLA (PL), neat PBAT (PB), PLA/PBAT blend (S0), and PLA/PBAT-based nanocomposites (S1-P1, S1-P2, S1-P3, S1-P4).

An alternative approach for investigating the miscibility and morphology is called the van Gurp–Palmen plot. Figure 4.18(b) shows the dependence of the phase angle (δ) on the complex modulus (G*). The presented plots reveal that the phase angle approaches a plateau of about 90° at a low complex modulus for neat PLA and PBAT, revealing a homogenous system and a dominant viscous behavior [151,153]. However, the phase angle of neat PBAT drops steeply at a high complex modulus caused by a much higher viscosity and entanglement of the PBAT chains, leading to an increase in the elastic response [151,154]. The obtained results also indicate the longer relaxation of the PBAT polymer during processing. In the presence of nano-SiO_2, the phase angle decreases significantly depending on the nano-SiO_2 location. This means an increase in the elasticity of the nanocomposites. According to the applied analysis, the van Gurp–Palmen plot is in good agreement with the Han plot. It is evident from the diagrams that the incorporation of nano-

SiO_2 as well as its location alter the microstructure in terms of the miscibility and morphology between the PLA and PBAT polymers.

4.3   Thermal Properties

It is well known that both polymer materials used in this work (PLA and PBAT) are semi-crystalline polymers. Therefore, their properties can be governed by the supramolecular structures, in this case known as the crystallization behavior. The incorporation of nano-particles and their preferential location may play an important role in the crystallization process of the two polymers during the melting and cooling process. Several techniques can be utilized to determine and understand the thermal behavior of polymer materials. In this work, DSC is used to obtain crystallization and melting behavior for non-isothermal and isothermal conditions. A supramolecular structure is shown via a PLOM during the crystallization process. In addition, a numerical simulation is applied to acquire a temperature distribution profile in the injection molding process. After that, a fast scanning or Flash DSC is combined with the obtained simulation data. The crystallization behavior in rapidly processing conditions is then studied. For comparison, neat PLA (PL), PLA filled with 1 vol.% nano-SiO_2 (PL1), and neat PBAT (PB) are also investigated. It should be mentioned that the neat PBAT sample is in a granular (Gn.) form for characterization of the thermal properties because it cannot be processed by an injection molding machine.

4.3.1   Crystallization and Melting Behavior

4.3.1.1 Non-Isothermal Crystallization

Figures 4.19(a) and (b) illustrate DSC thermograms during 1st cooling and 2nd heating scans of all studied materials, respectively. According to the thermograms, crystallization temperatures ($T_{c,PL}$ and $T_{c,PB}$) and enthalpy of crystallization ($\Delta H_{c,PL}$) are observed from the 1st cooling thermograms. Glass transition temperatures ($T_{g,PL}$ and $T_{g,PB}$), cold crystallization temperature ($T_{cc,PL}$), and melting temperatures ($T_{m,PL}$ and $T_{m,PB}$) are examined from the 2nd heating thermograms. The DSC data values obtained from those thermograms are reported in Table 4.4. The degree of crystallinity in the continuous PLA matrix ($X_{c,PL}$), calculated according to the equation (3.10), is presented in Figure 4.20 (see Appendix G).
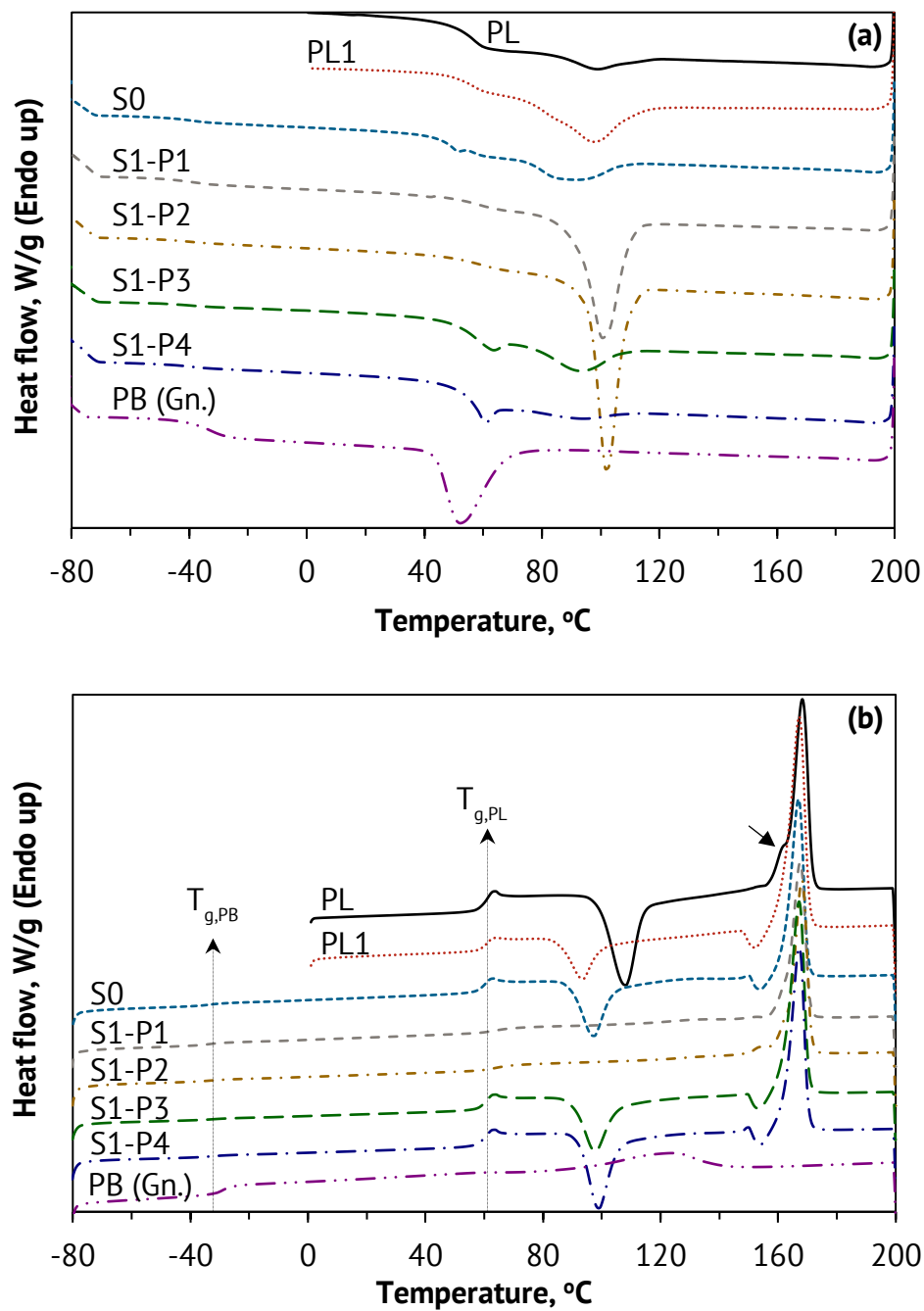
Figure 4.19:   DSC thermograms during (a) 1st cooling and (b) 2nd heating scans of neat PLA (PL), PLA-S1 (PL1), PLA/PBAT blend (S0), PLA/PBAT-based nanocomposites (S1-P1, S1-P2, S1-P3, S1-P4), and neat PBAT (PB) (granular sample, Gn.).

Table 4.4:   Summarized DSC results obtained from the thermograms during 1st cooling and 2nd heating scans for all materials

During 1st cooling scan			
Material	**$T_{c,PB}$, °C**	**$T_{c,PL}$, °C**	**$\Delta H_{c,PL}$, J/g**
PLA (PL)	–	99.5 ± 0.5	4.5 ± 1.0
PLA-S1 (PL1)	–	97.2 ± 0.5	14.6 ± 0.8
PLA/PBAT-S0 (S0)	51.6 ± 0.3	87.8 ± 3.7	5.8 ± 1.7
PLA/PBAT-S1-P1 (S1-P1)	–	100.2 ± 0.5	27.7 ± 0.3
PLA/PBAT-S1-P2 (S1-P2)	–	101.8 ± 0.1	31.6 ± 0.4
PLA/PBAT-S1-P3 (S1-P3)	63.5 ± 0.1	93.3 ± 0.1	8.2 ± 0.3
PLA/PBAT-S1-P4 (S1-P4)	60.3 ± 0.4	92.3 ± 1.5	2.0 ± 0.2
PBAT (PB) (Granulate, Gn.)	51.5 ± 1.1	–	–
During 2nd heating scan			
Material	**$T_{g,PB}$, °C**	**$T_{g,PL}$, °C**	**$T_{cc,PL}$, °C**	**$T_{m,PL}$, °C**
PLA (PL)	–	61.2 ± 0.2	107.8 ± 0.3	168.3 ± 0.03
PLA-S1 (PL1)	–	61.4 ± 0.3	93.8 ± 0.3	167.3 ± 0.3
PLA/PBAT-S0 (S0)	-33.9 ± 0.2	60.7 ± 0.1	96.9 ± 0.3	167.0 ± 0.1
PLA/PBAT-S1-P1 (S1-P1)	-33.8 ± 0.2	63.8 ± 0.8	–	167.5 ± 0.4
PLA/PBAT-S1-P2 (S1-P2)	-33.6 ± 0.4	63.9 ± 0.5	–	168.1 ± 0.2
PLA/PBAT-S1-P3 (S1-P3)	-32.5 ± 0.2	61.1 ± 0.2	97.9 ± 0.04	167.3 ± 0.1
PLA/PBAT-S1-P4 (S1-P4)	-33.2 ± 0.6	61.1 ± 0.1	99.2 ± 0.2	167.2 ± 0.1
PBAT (PB) (Granulate, Gn.)	-29.1 ± 0.1	–	–	*123.6 ± 0.5

*Melting temperature of the PBAT polymer ($T_{m,PB}$).

As shown in Figure 4.19(a), the exothermic peaks are observed in all materials. They are attributed to the crystallization processes of PLA and/or PBAT polymers upon cooling. Neat PLA exhibits a small crystallization peak at 99.5 °C and contains a degree of crystallinity of only ca. 7 %. It is well known that the nucleation and crystallization rates of neat PLA are relatively low in homogeneous conditions. When 1 vol.% nano-SiO_2 is added into the PLA polymer (PL1), a relatively stronger crystallization peak is noticed indicated by

the higher enthalpy of crystallization (ΔH_c) (see Table 4.4). This leads to a significant increase in the degree of crystallinity up to ca. 32 %, as depicted in Figure 4.20. However, the crystallization temperature of PLA slightly decreases by approximately 2 °C. The result suggests that the crystallization rate of PLA containing 1 vol.% nano-SiO_2 is comparatively slower during cooling from the melt.
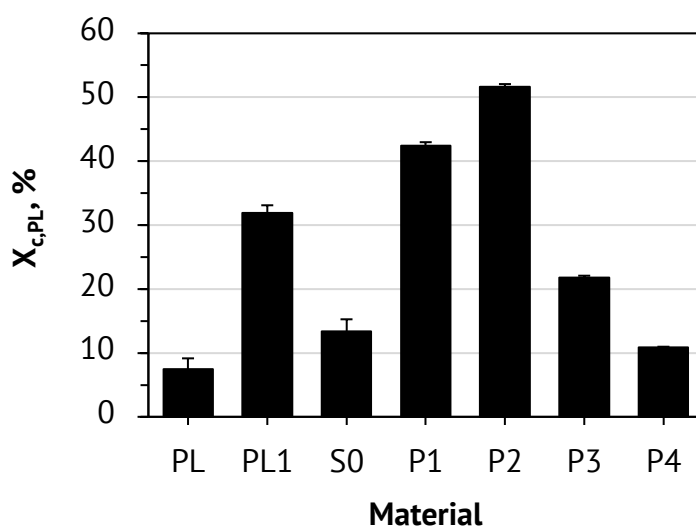
Figure 4.20:   Degree of crystallinity in the PLA phase ($X_{c,PL}$) of neat PLA (PL), PLA-S1 (PL1), PLA/PBAT blend (S0), and PLA/PBAT-based nanocomposites (S1-P1, S1-P2, S1-P3, S1-P4).

In general, nano-SiO_2 is an efficient nucleating agent and promotes the crystallization behavior of the polymer matrix, in this case, the PLA polymer [9,155]. However, it should be noted that the incorporation of nanoparticles could cause either nucleating or retarding effects during the crystallization process [14,121,155]. On the one hand, the nanoparticles serve as nucleation sites and then reduce the nucleation induction period. Consequently, the crystallization ability is promoted through the heterogeneous nucleation process. On the other hand, the molecular mobility of PLA is confined by the nanoparticles, which are usually formed aggregates and/or agglomerates. This phenomenon diminishes the growth of polymer crystals. Thus, the role of nano-SiO_2 relates to the degree of dispersion and distribution [156]. As for the PLA-S1, the decrease in crystallization temperature is assumed to be due to the agglomerates of nano-SiO_2 in the PLA matrix.

For the PLA/PBAT blend (S0), two crystallization peaks are detected at 87.8 °C and 51.6 °C. The first crystallization peak corresponds to the major PLA phase (matrix), and the relatively smaller peak corresponds to the minor PBAT phase. The crystallization temperature of PBAT can be confirmed by the neat PBAT thermogram, as shown in Figure 4.19(a). The

obtained results indicate that the crystallization temperature of PLA dramatically decreases with the presence of 20 vol.% PBAT, signifying that the PBAT domains hinder the chain mobility of the PLA polymer. However, while the crystallization process of PLA starts later, the degree of crystallinity increases from 7.4 % to 13.4 % compared to that of neat PLA. Therefore, it can be concluded that while the PBAT polymer restricts the chain mobility of PLA macromolecules, it can also act as an effective nucleating agent for PLA. A similar result has been reported in the literature [14]. When incorporating 1 vol.% nano-SiO_2 into the blend, the crystallization behavior of PLA is remarkably enhanced in all the PLA/PBAT-based nanocomposites. Both the crystallization temperature and degree of crystallinity of PLA increase up to 101.8 $^\circ$C and 51.6 %, as shown in Table 4.4 and Figure 4.20, respectively. This means that the co-existence of the PBAT droplets as a dispersed polymer and nano-SiO_2 as dispersed nanofillers achieves the synergetic effect for the crystallization behavior of PLA. Furthermore, a more significant influence is acquired in the nanocomposites P1 and P2, in which nano-SiO_2 disperses mainly in the PLA phase and at the PLA/PBAT interface. This is confirmed by a very sharp and strong crystallization peak of the PLA phase, as seen in Figure 4.19(a). Unexpectedly, the nanocomposite P2 has a better crystallization ability in the PLA phase when considering the nano-SiO_2 concentration in the observed phase. It is worth noting that a greater amount of nano-SiO_2 located in the PLA phase is observed in the nanocomposite P1 ($A_{Si,PL}$: S1-P1 > S1-P2, see Figure 4.4). This phenomenon is attributed to the role of nano-SiO_2 dispersion and distribution in the respective polymer phase, as mentioned previously. As described in section 4.1: Morphology, the nanocomposite P2 contains a smaller agglomerate size of nano-SiO_2 ($x_{50,2,PL}$) compared to the nanocomposite P1 in the PLA phase (see Table 4.3). This leads to a relatively lower restriction on the mobility of the PLA polymer. In this case, it is apparent that the nanocomposite P2 with a lower amount of nano-SiO_2 and a smaller agglomerate size of nano-SiO_2 in the PLA phase is better optimized in terms of the crystallization behavior of the PLA matrix. In other words, the mobility of the PLA macromolecules to diffuse, form, and grow PLA crystals dominates over the excessive number of nuclei or the degree of the heterogeneous nucleation process.

For the nanocomposites P3 and P4, as expected, the crystalline ability in the PLA phase is relatively poor when compared with the nanocomposites P1 and P2. This phenomenon can be explained by the location of nano-SiO_2. As described earlier, nano-SiO_2 is barely detected in the major PLA phase but is mostly located in the dispersed PBAT droplets and at the interface for these nanocomposites. Therefore, the nucleating effect initiated by

nano-SiO$_2$ is rather low for the crystallization process of PLA. In contrast, the crystalliza-
tion temperature of PBAT ($T_{c,PB}$) significantly increases by approximately 10 ^{o}C compared
to the PLA/PBAT blend, signifying that the potential of nano-SiO$_2$ to act as a nucleating
agent is distributed to the PBAT polymer where the nanoparticles are mostly located.

The melting behavior of all the observed materials is determined during the 2nd heating
scan. Figure 4.19(b) shows the glass transition temperature (T_g), cold crystallization tem-
perature (T_{cc}), and melting temperature (T_m). Neat PLA has a glass transition temperature
of 61.2 ^{o}C (see Table 4.4). It is clear that only the nanocomposites P1 and P2 present a
slight increase in the glass transition temperature of the PLA polymer (from ca. 61 ^{o}C to
63 ^{o}C), while the glass transition temperature of the other materials remains constant. As
already stated, the nano-SiO$_2$ agglomerate is highly dispersed in the PLA phase for these
nanocomposites and obstructs the mobility of PLA macromolecules during the heating
process. In addition, the PLA/PBAT blend and its nanocomposites present two glass tran-
sition temperatures ($T_{g,PB}$ and $T_{g,PL}$), which are attributed to the PBAT and PLA phases,
respectively. The results also reveal that the presence of the flexible PBAT polymer does
not influence the mobility of the PLA polymer upon heating. These phenomena are des-
cribed as a characteristic of a phase-separated material, which means that there is no
significant molecular interactions between the PLA and PBAT polymers upon heating
[44,157–159].

Figure 4.19(b) illustrates an exothermic transition at about 93–108 ^{o}C, which is observed
in the neat PLA, PLA-S1, PLA/PBAT-S0, PLA/PBAT-S1-P3, and PLA/PBAT-S1-P4. It is at-
tributed to a cold crystallization process of the PLA polymer. Typically, the PLA polymer
could crystallize in the range between the glass transition and melting temperatures
during the heating process, as a so-called cold crystallization. The cold crystallization
process would occur when the crystallization from the previous cooling process is incom-
plete. In other words, the PLA polymer has an insufficient amount of time to achieve full
crystallinity upon cooling, consequently leading to a recrystallization process upon con-
tinued heating [9]. As can be seen, the presence of nano-SiO$_2$ and the PBAT polymer can
decrease the cold crystallization temperature in all cases, confirming the improvement in
the crystalline ability of PLA. In particular, the nanocomposites P1 and P2 can entirely
eliminate the cold crystallization process due to the high-efficiency nucleating effect. As
a result, very high degrees of crystallinity up to ca. 42 % and 52 %, respectively, are
reached. Furthermore, a small exothermic peak before the melting transition is noticed
at around 153 ^{o}C, indicating a second cold crystallization process. As reported in the li-
terature, the latter cold crystallization process is identified as the reorganization of α'-

crystals into α-crystals [160,161]. The α'-crystal structure is considered to be similar to the α-crystals, but with a less ordered and looser chain packing. It is worth mentioning that the formation of the PLA crystal is reported with different crystal conformations: (i) α-form, (ii) β-form, and (iii) γ-form. The most common PLA crystals are the α-form, which occurs in the conventional melting process and solution crystallization conditions [161,162]. The β-form and γ-form are most likely to form only upon hot drawing or fiber spinning [122,163] and via epitaxial crystallization of PLA [164], respectively.

The melting temperature of PLA is observed at around 167–168 $^\circ$C, as reported in Table 4.4. However, the neat PLA displays a small shoulder before a sharp melting peak at around 162 $^\circ$C, as marked by an arrow in Figure 4.19(b). Theoretically, the lower melting transition can be attributed to two possible reasons: the melt/recrystallization process and dual crystal conformation [44,165,166]. However, as mentioned previously, the PLA crystals in the β-form and γ-form are likely not the case. Therefore, it can be concluded that the lower melting temperature is attributed to the melt/recrystallization process of PLA crystals in the α-form. At a heating rate, the imperfect crystals (α'-crystals) have enough time to melt and reorganize into the perfect crystals (α-crystals). Then, the perfect ones melt again at a higher temperature [44]. Other than the neat PLA, the melting temperature of PLA remains almost unchanged whether the nano-SiO_2 and PBAT polymer are incorporated or not. The sharp endothermic peak without a shoulder at the lower temperature suggests that the more stable PLA crystals are obtained during the melting process. For the PBAT phase, the melting transition cannot be detected in the PLA/PBAT blend and its nanocomposites, as shown in Figure 4.19(b). The melting temperature of PBAT should be seen at ca. 123 $^\circ$C according to the neat PBAT thermogram. The undetected melting transition is possibly due to the minority in the volume ratio of the PBAT polymer in the mentioned materials.

4.3.1.2 Isothermal Crystallization

The isothermal crystallization is further investigated by DSC to explore the crystallization kinetics at various crystallization temperatures (T_c). In this work, the crystallization temperatures in the range of 80–120 $^\circ$C are examined. The obtained thermograms of exothermal heat flow (Q) versus crystallization time are shown in Figure 4.21. Because the evolution of the crystallization process at various temperatures exhibits a quite similar trend and for conciseness, only the selected thermograms for all materials at a crystalli-

zation temperature of 100 °C and the PLA/PBAT-S1-P2 nanocomposite at different crys-
tallization temperatures are presented in Figures 4.21(a) and (b), respectively (see Appen-
dix H). However, all the relevant data are given in Table 4.5.
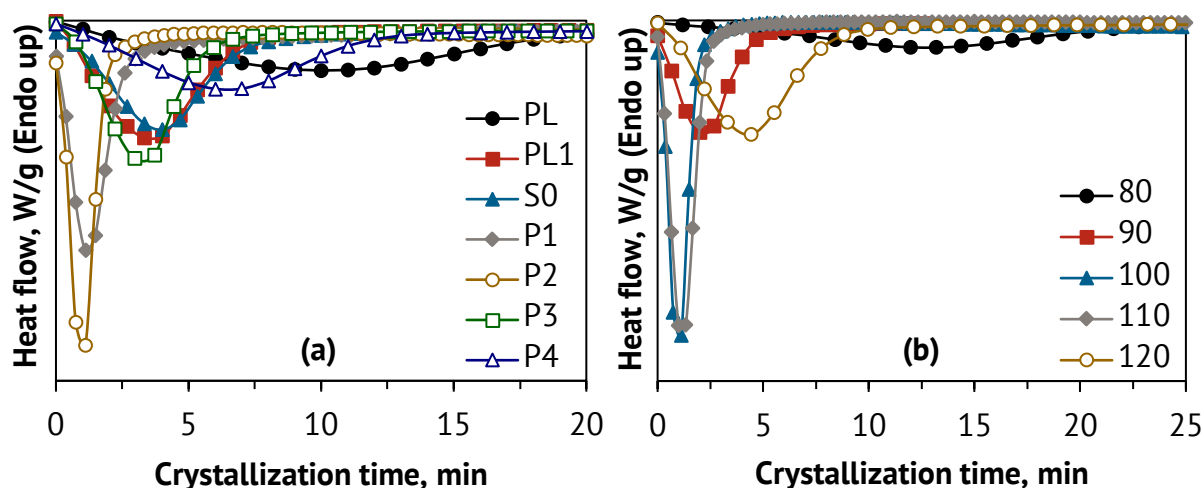
Figure 4.21:   Isothermal crystallization thermograms of (a) neat PLA (PL), PLA-S1 (PL1),
PLA/PBAT blend (S0), and PLA/PBAT-based nanocomposites (S1-P1, S1-P2, S1-P3, S1-P4)
at a crystallization temperature of 100 °C and (b) PLA/PBAT-S1-P2 at different crystalli-
zation temperatures.

As seen in Figure 4.21(a), the crystallization behavior investigated by the isothermal con-
dition of all studied materials exhibits a similar trend in the non-isothermal condition.
The crystallization peak of neat PLA is very broad and takes the longest crystallization
time until the crystallization process is completed. The addition of nano-SiO_2 into either
the PLA or the PLA/PBAT blend shows a narrower peak. Furthermore, the crystallization
curves shift to shorter crystallization times, especially the nanocomposites P1 and P2.
The crystalline ability in each material can be explained by the same reasons in the non-
isothermal condition. Figure 4.21(b) illustrates the crystallization process of nanocompo-
site P2 at different crystallization temperatures. As a result, the crystallization behavior
of PLA is strongly dependent on the crystallization temperature. The result also suggests
that the crystallization temperatures in the range of 100−110 °C promote the most effi-
cient effect on the crystallization rate of the PLA polymer.

To quantify the crystallization rate, the relative crystallinity (X_t) versus crystallization time
is plotted and examined. The relative crystallinity is defined by integrating the exother-
mic heat flow during the crystallization process, which is given by the following relation-
ship [167]:

$$X_t = \frac{Q_t}{Q_\infty} = \int_0^t \left(\frac{dH_c}{dt}\right) dt \Big/ \int_0^\infty \left(\frac{dH_c}{dt}\right) dt \tag{4.9}$$

where Q_t and Q_∞ are the heat flow generated at time t and at an infinite time t_∞ or a complete crystallization time, respectively. dH_c/dt is the rate of heat flow evolution. Figure 4.22 shows the obtained curves showing the typically sigmoidal correlation as a function of crystallization time (see Appendix H). According to the obtained curves, the half-time of crystallization ($t_{1/2}$) can be defined as the time required to attain half of the complete crystallization ($X_t = 0.5$), as shown in Figure 4.22(a). It is important to mention that the half-time of crystallization is usually applied to estimate the overall rate of the crystallization process [91]. All the responding half-time of crystallization data based on the experiments ($t_{1/2,exp.}$) are listed in Table 4.5 and illustrated in Figure 4.23.
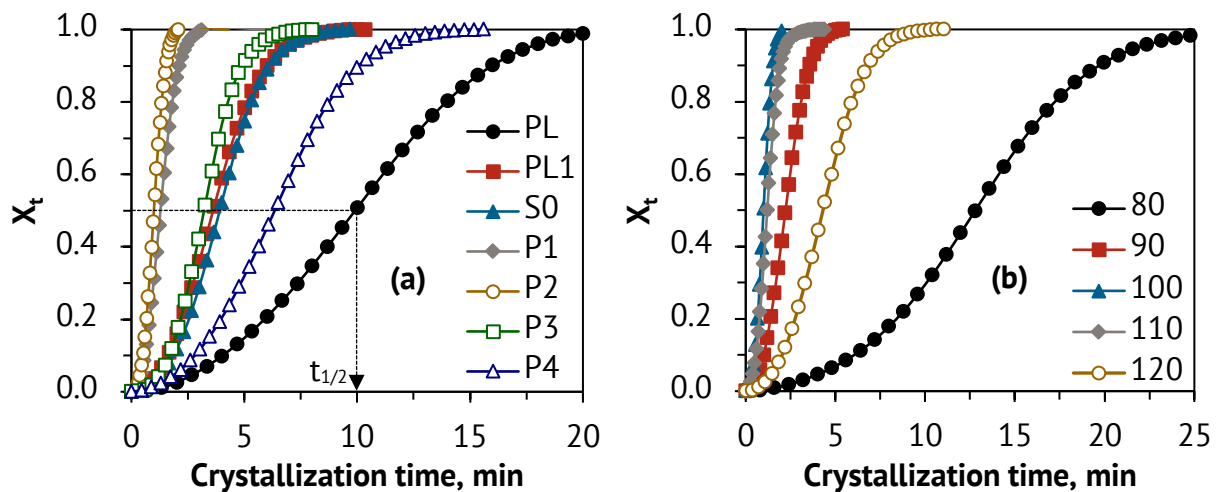
Figure 4.22:   Relative crystallinity (X_t) as a function of crystallization time: (a) neat PLA (PL), PLA-S1 (PL1), PLA/PBAT blend (S0), and PLA/PBAT-based nanocomposites (S1-P1, S1-P2, S1-P3, S1-P4) at a crystallization temperature of 100 ℃ and (b) PLA/PBAT-S1-P2 at different crystallization temperatures.

Table 4.5:   Summary of the isothermal crystallization data along with the parameters from the Avrami equation

Material	T_c, ºC	$t_{1/2,exp.}$, min	n	$k \times 10^{-3}$, min^{-1}	R^2	$t_{1/2,cal.}$, min
PLA	80	27.52	2.34	0.67	0.9999	27.55
(PL)	90	19.26	2.68	0.26	0.9996	19.08
	100	10.05	2.30	3.83	0.9993	9.84
	110	10.58	2.33	3.10	0.9979	10.30
	120	16.67	1.90	3.47	0.9992	16.25
PLA-S1	80	6.89	2.26	9.06	0.9992	6.87
(PL1)	90	2.97	2.23	60.78	0.9919	3.04
	100	3.65	2.45	29.67	0.9999	3.63
	110	3.93	2.52	22.36	0.9999	3.92
	120	8.24	2.55	3.40	0.9997	8.12
PLA/PBAT-S0	80	17.84	2.20	1.29	0.9993	17.56
(S0)	90	6.58	3.07	2.11	0.9999	6.61
	100	3.96	2.60	20.26	0.9999	3.93
	110	6.22	2.47	8.22	0.9995	6.15
	120	16.33	2.15	1.89	0.9996	16.12
PLA/PBAT-S1-P1	80	14.08	2.62	0.73	0.9991	13.90
(P1)	90	3.07	2.47	43.81	1.0000	3.06
	100	1.30	2.44	364.96	0.9999	1.30
	110	1.56	2.36	241.32	0.9998	1.56
	120	4.32	2.44	20.06	0.9999	4.32
PLA/PBAT-S1-P2	80	13.19	2.65	0.79	0.9997	13.04
(P2)	90	2.37	2.49	91.57	0.9999	2.26
	100	0.99	2.81	702.32	0.9999	1.00
	110	1.22	2.54	416.23	0.9998	1.22
	120	4.11	2.48	21.70	0.9999	4.08
PLA/PBAT-S1-P3	80	23.59	2.18	0.76	0.9960	22.71
(P3)	90	5.86	2.86	4.54	0.9999	5.86

Material	T_c, °C	$t_{1/2,exp.}$, min	n	$k \times 10^{-3}$, min^{-1}	R^2	$t_{1/2,cal.}$, min
PLA/PBAT-S1-P3	100	3.33	2.88	21.98	0.9998	3.33
(P3)	110	4.10	2.51	20.56	0.9999	4.07
	120	9.46	2.55	2.31	0.9997	9.35
PLA/PBAT-S1-P4	80	27.14	2.27	0.40	0.9980	26.57
(P4)	90	10.30	2.95	0.82	0.9999	10.21
	100	6.16	2.55	6.92	0.9997	6.10
	110	6.96	2.46	6.23	0.9997	6.88
	120	17.75	2.26	1.15	0.9992	17.47
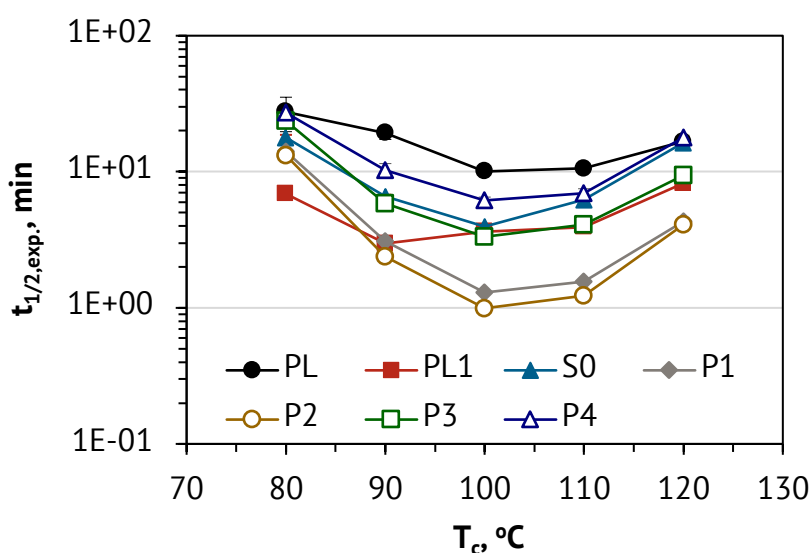
Figure 4.23: Half-time of crystallization ($t_{1/2}$) as a function of crystallization temperature (T_c) for different materials.

In general, the half-time of crystallization is reported as a function of crystallization temperature to establish the optimized temperature range. As seen in Figure 4.23, the typical U-shaped curves are observed. It is apparent that the U-shaped curve shifts to the higher half-time of crystallization for mostly the entire range of crystallization temperatures when a material exhibits a slower crystallization rate. It is worth mentioning that an increase in the half-time of crystallization means a decrease in the overall crystallization rate and vice versa. Accordingly, it is clear that the fastest crystallization process of PLA in all the studied materials is obtained at a crystallization temperature of 100 °C, except for PLA-S1, whose minimum half-time of crystallization is observed at 90 °C. Surprisingly,

considering the inherently low crystallization rate of PLA, the best crystalline perfor-mance is reached by markedly reducing the half-time of crystallization from 10.05 min in the neat PLA to 0.99 min in the nanocomposite P2. Consequently, the obtained results from the isothermal condition agree with the non-isothermal condition that the crystal-lization behavior of PLA is strongly influenced by the presence of nano-SiO_2 and its pre-ferable location.

It is well known that the crystallization process is generally controlled by two main fac-tors: (i) nucleation and (ii) crystalline growth. The U-shaped curve usually presents the minimum half-time of crystallization. This phenomenon is related to the competition be-tween the nucleation rate and mobility of the polymer macromolecules [121,162,168]. On the one hand, the half-time of crystallization increases with a decrease in the crystal-lization temperature (close to a glass transition temperature, T_g), and a reduction in the chain mobility plays an important role, resulting in a slower rate of crystalline growth. On the other hand, when the crystallization temperature is greater than the temperature of the minimum half-time (close to a melting temperature, T_m), the excessive chain mobility restricts the nucleus formation, leading to an extension of the nucleation induction period and eventually the overall crystallization rate. Therefore, the crystallization temperature with the minimum half-time exhibits the equilibrium between the nucleation and crys-talline growth rates.

Furthermore, the well-known Avrami model is usually applied to describe the kinetics of isothermal crystallization of polymers. The Avrami equation, which is associated with the relative crystallinity, is given by the following equation [162,169–171]:

$$X_t = 1 - exp\left(-kt^n\right) \tag{4.10}$$

where k is the overall crystallization rate constant and n is the Avrami index, which describes the nucleation mechanism and the crystal growth morphology. An Origin$^®$ 2018 Graphing & Analysis software is used for Avrami curve fitting according to the equation (4.10). Figure 4.24 shows the experimental isothermal crystallization data (symbols) ver-sus the Avrami curve fittings (dotted line). Accordingly, the n and k parameters can be determined from the calculation of the curve fitting, as reported in Table 4.5. In addition, the correlation coefficient (R^2) is also presented to ensure the quality of the curve fitting.
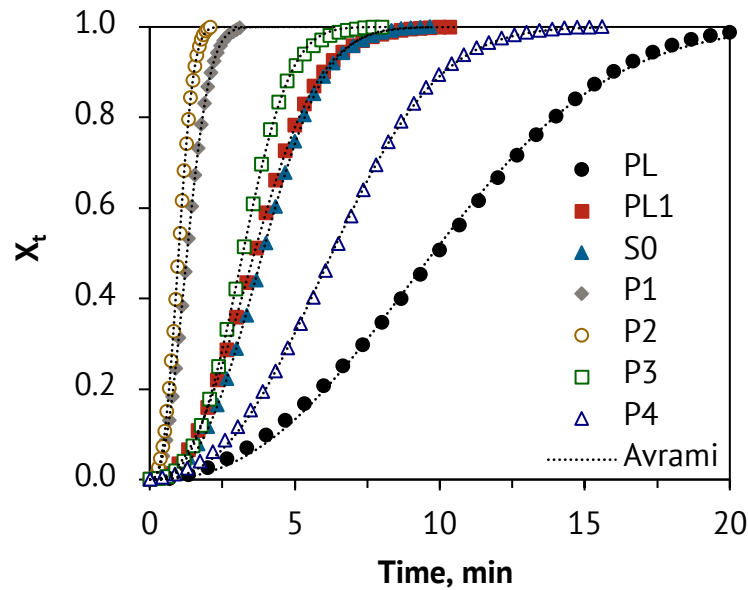
Figure 4.24:   Relative crystallinity (X_t) as a function of crystallization time of all materials at a crystallization temperature of 100 °C; experimental isothermal crystallization data (symbols) and Avrami curve fittings (dotted line).

As seen from Table 4.5, all correlation coefficient values are greater than 99 %, indicating a good fitting between the experimental data and the Avrami equation. Consequently, the half-time of crystallization based on the Avrami equation can be calculated, as described by the following equation:

$$t_{1/2,cal.} = (\ln 2/k)^{1/n} \tag{4.11}$$

As a result, the half-time of crystallization calculated by the Avrami equation ($t_{1/2,cal.}$) is in good agreement with the half-time of crystallization based on the experimental data ($t_{1/2,exp.}$) (see Table 4.5). Furthermore, the Avrami index (n) can be obtained from the curve fitting and can be used to describe the contributions of nucleation and crystal growth. According to Lorenzo et al. [172], the Avrami index is composed of two terms as given by the following relationship:

$$n = n_d + n_n \tag{4.12}$$

where n_d represents the dimensionality index of the formed lamellae, in which the 1, 2, and 3 values are associated with one-, two-, and three-dimensional entities, respectively. In general, the Avrami index can be estimated as 2 and 3 for a polymer, which represents

respective axialites (two-dimensional lamella aggregates) and spherulites (three-dimensional aggregates of radial lamellae). n_n represents the time dependence of the nucleation. The n_n values should be either 0 or 1, where 0 refers to instantaneous or heterogeneous nucleation and 1 refers to sporadic or homogeneous nucleation. However, a nucleation process that is somewhere between completely instantaneous and sporadic is also possible. A non-integer Avrami index can sometimes be explained in this way among others [172,173]. For some cases, when the spherulite growth is non-linear with time, the n_n value can be estimated to be 0.5 [172].

As shown in Table 4.5, the Avrami index is in the range of 1.90–2.68 for neat PLA and 2.15–3.07 for the PLA-based blend and nanocomposites. Therefore, it can be assumed that neat PLA would be in between one- and two-dimensional growth mechanisms with sporadic nucleation. As for the PLA-based blend and nanocomposites, the crystal growth and nucleation contributions would be between two- and three-dimensional crystal growth and instantaneous nucleation, respectively.

4.3.2 Spherulite Development

To further understand the crystallization behavior, PLOM is used to observe the supermolecular structure or so-called spherulite of all studied materials during the crystallization process. The development of the spherulite morphology is examined under isothermal crystallization at two selected crystallization temperatures (110 °C and 130 °C).

Figure 4.25 shows the development of the spherulite morphology upon isothermal crystallization at 110 °C for 2, 5, and 10 min. The spherulites are formed and then grown as a function of time. The growth of the spherulite stops when adjacent spherulites impinge on one another. Finally, the crystallization process is completed when the spherulites fully grow all over the whole area. It should be noted that the spherulites typically present a Maltese cross pattern under polarization. As shown in Figure 4.25(a), the neat PLA appears to form a lower number of nuclei compared to the PLA-based and PLA/PBAT-based nanocomposites. This phenomenon is associated with the nano-SiO_2 in the PLA phase serving as the additional nucleation sites. With a greater number of nuclei, the space for growth is limited for each spherulite, resulting in a relatively smaller spherulite size; hence the crystallization process is completed more quickly. In particular, the polarized light optical micrographs of the nanocomposites P1 and P2 present fully developed spherulites at less than 2 min, as seen in Figures 4.25(d) and (e), respectively. Moreover, the finest spherulite size is also observed in these two nanocomposites. Accordingly, the

crystallization results observed by PLOM are consistent with the isothermal crystallization kinetics obtained from DSC.
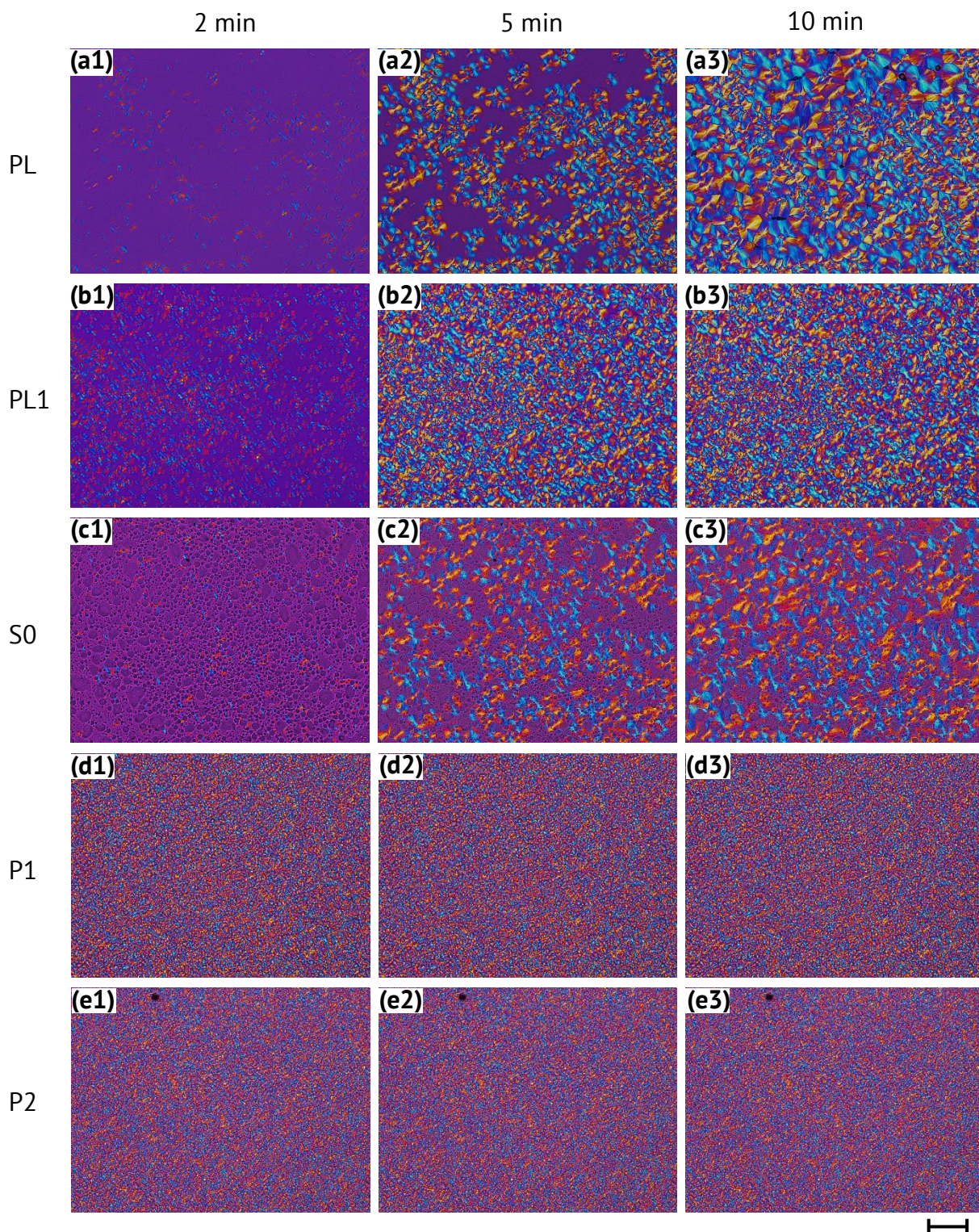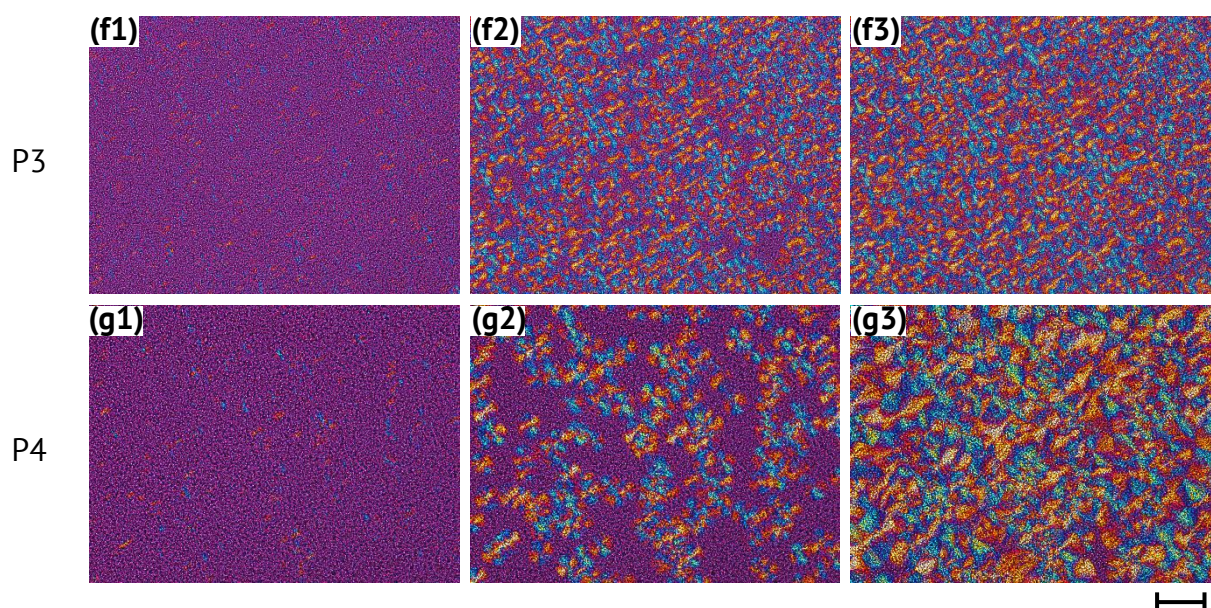
Figure 4.25: Polarized light optical micrographs under isothermal crystallization at 110 °C for 2, 5, and 10 min: neat PLA (PL), PLA-S1 (PL1), PLA/PBAT blend (S0), and PLA/PBAT-based nanocomposites (S1-P1, S1-P2, S1-P3, S1-P4) (scale bar = 50 μm).

As mentioned earlier, a higher isothermal crystallization temperature is also examined to study the effect of crystallization temperature on the supermolecular structure of the PLA polymer. Figure 4.26 illustrates the polarized light optical micrographs under isothermal crystallization at 130 °C for 5, 30, and 60 min. The result shows that the formation of the nuclei requires a longer time when compared to the results obtained from the isothermal crystallization at 110 °C. Fewer nuclei are detected. The impingement of adjacent spherulites is delayed, and the spherulite size is comparatively large. As a result, the overall crystallization rate is very slow at a higher crystallization temperature. On the one hand, the chain mobility of the polymer is very high at a temperature close to the melting temperature (T_m), which facilitates the spherulite growth rate. On the other hand, the formation of nuclei is confined due to excessive chain mobility, as described in the previous section [168]. In addition to the fact that all the materials are held for 60 min at 130 °C, the amorphous region remains, as shown in Figure 4.26.
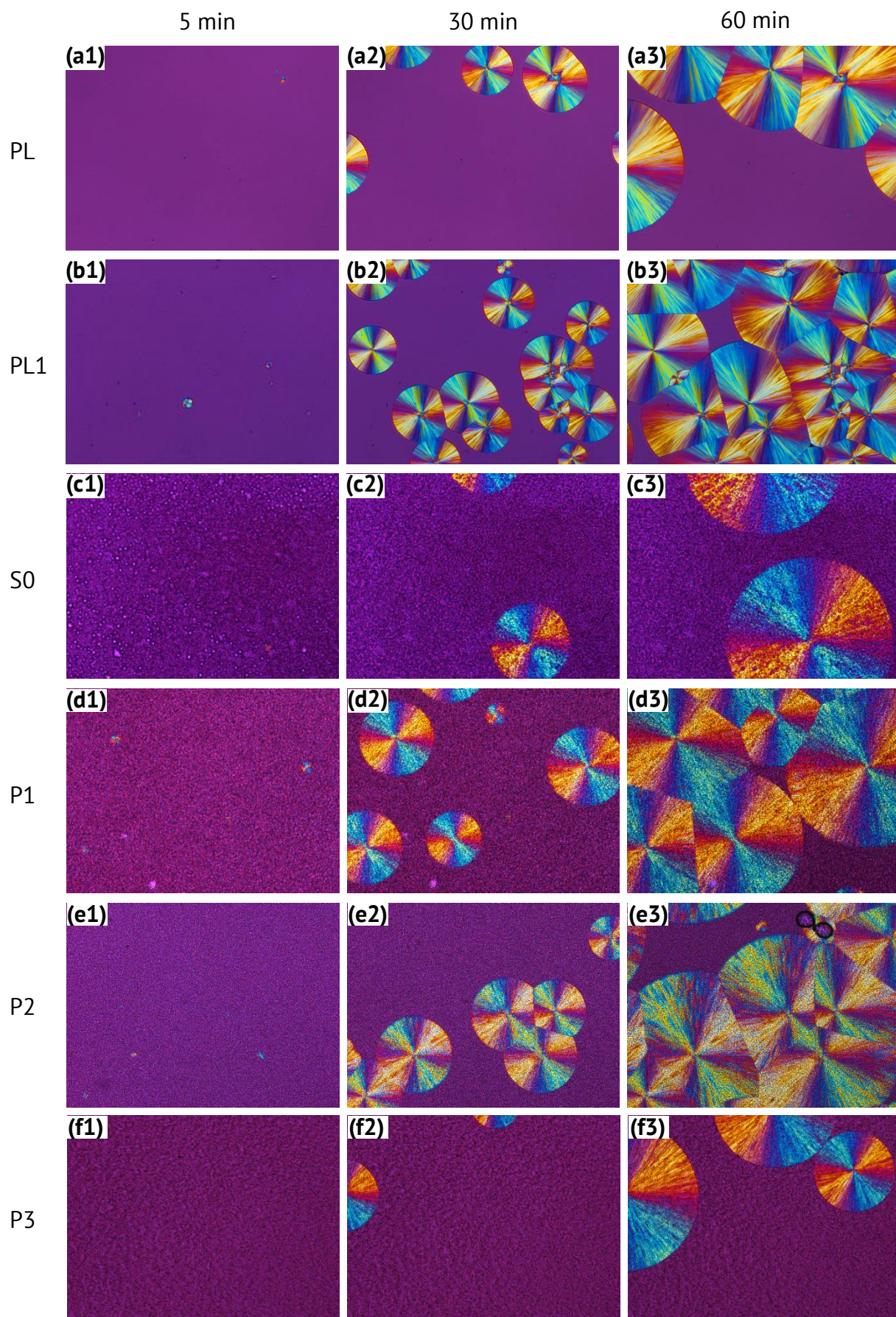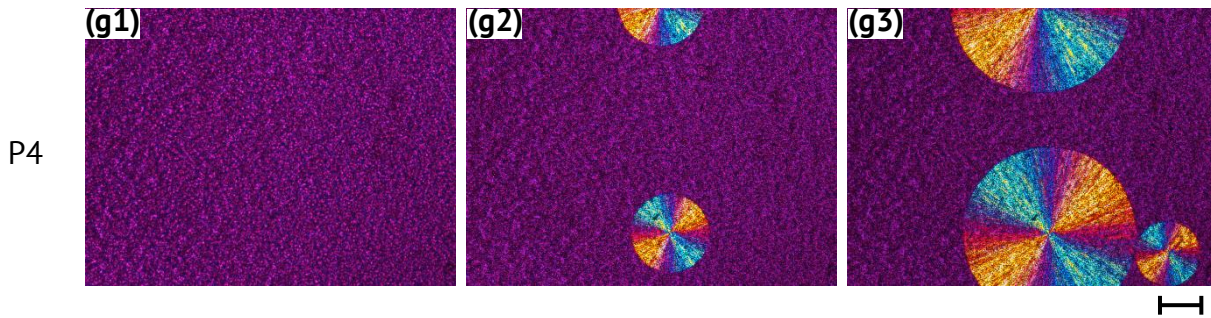
Figure 4.26: Polarized light optical micrographs under isothermal crystallization at 130 °C for 5, 30, and 60 min: neat PLA (PL), PLA-S1 (PL1), PLA/PBAT blend (S0), and PLA/PBAT-based nanocomposites (S1-P1, S1-P2, S1-P3, S1-P4) (scale bar = 100 μm).

4.3.3   Simulation of Injection Molding

It is common knowledge that the actual production processes used in industry to form a particular shape (i.e., injection molding machine) are intended to process as fast as possible to increase the production efficiency. The production process is, therefore, one of the key parameters to define and describe the final properties of the materials, especially when using semi-crystalline polymers. The cooling rates during the production process are generally high, particularly in the local skin area where the melting polymer flows and contacts with the cooled mold. In this work, Autodesk Moldflow software is used to predict the cooling rates during injection molding. Figure 4.27 illustrates the 3D model of the injection-molded plate before and after mesh refinement (1,710,719 elements).
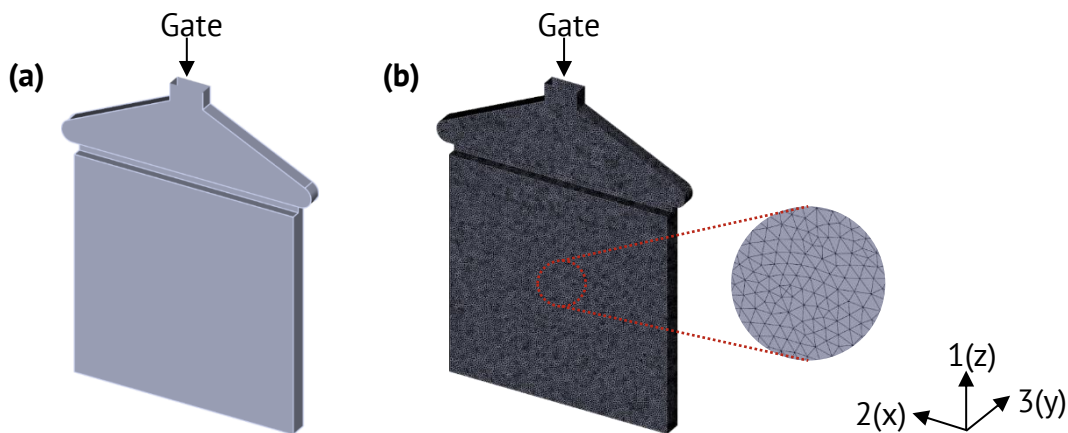
Figure 4.27: 3D model of the injection-molded plate (a) before and (b) after mesh refinement (1,710,719 elements).

After simulation, the temperature distribution data were collected from the center of the injection-molded plate (star symbol) at different thicknesses ranging from the skin area to the core area (0.10, 0, 25, 0.50, 1.00, 1.50, and 2.00 mm), as seen in Figure 4.28. Moreover, the initial temperature (T_0) was recorded at the maximum temperature measured at the gate with the filling time of 0.14 s for a later calculation of the average cooling rate.
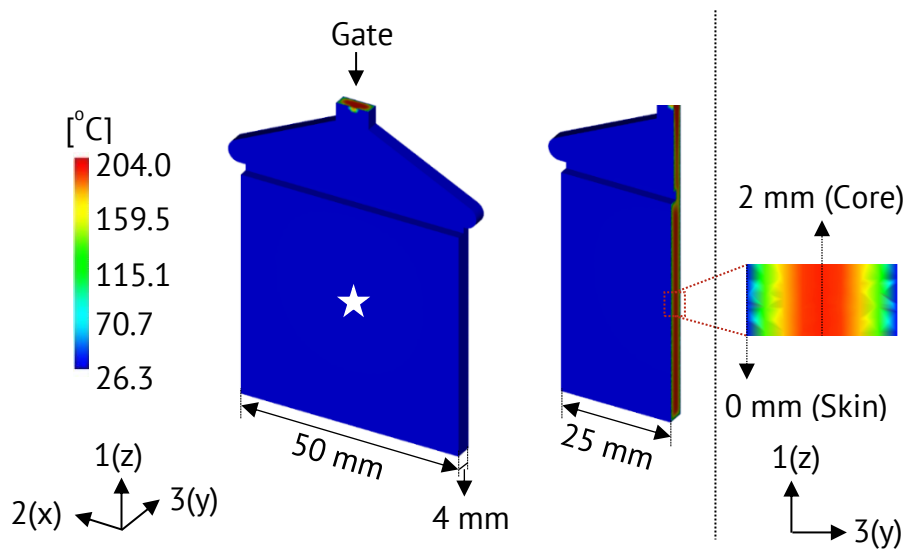
Figure 4.28: Schematic structures of the injection-molded plate after simulation showing the temperature distribution across the wall thicknesses.

Figure 4.29 shows an example of the temperature distribution obtained from the simulation starting from the polymer filling to the end of the injection cycle. The images of the injection-molded plate are shown with half the thickness of an xz-plane (y = 2.00 mm). It should be noted that the filling, cooling, and wrapping times are based on the real-setting conditions in the injection molding process. After that, the temperature profiles are plotted as a function of time at different thicknesses of the injection-molded plate, as shown in Figure 4.30. As expected, an instant decrease in the local temperature near the wall of the cold mold is observed within a few seconds after polymer filling. On the contrary, the melting polymer cools down slower at the local core area.
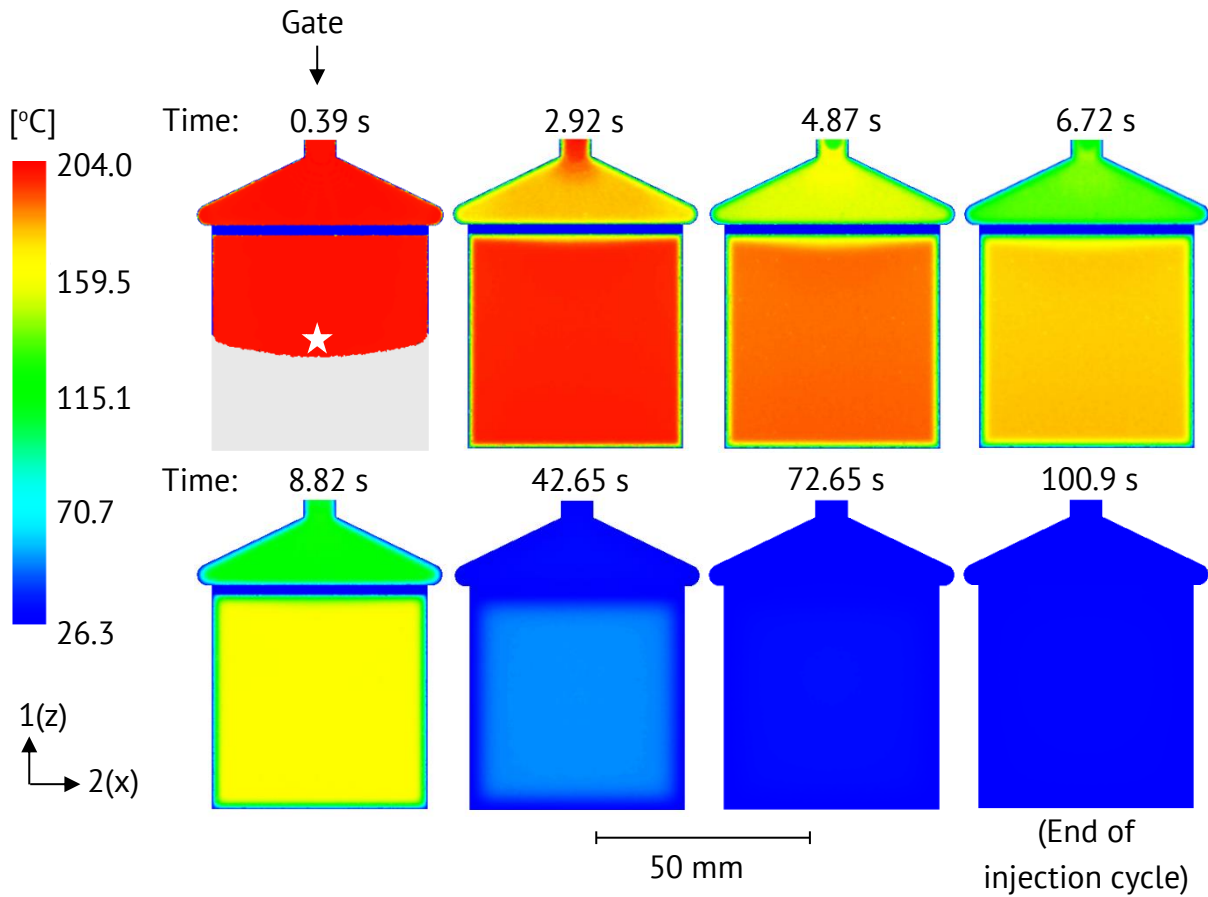
Figure 4.29: Temperature distribution obtained from the simulation of injection molding; starting from the polymer filling to the end of an injection cycle. The images of the injection-molded plate are shown with half the thickness of an xz-plane (y = 2.00 mm).
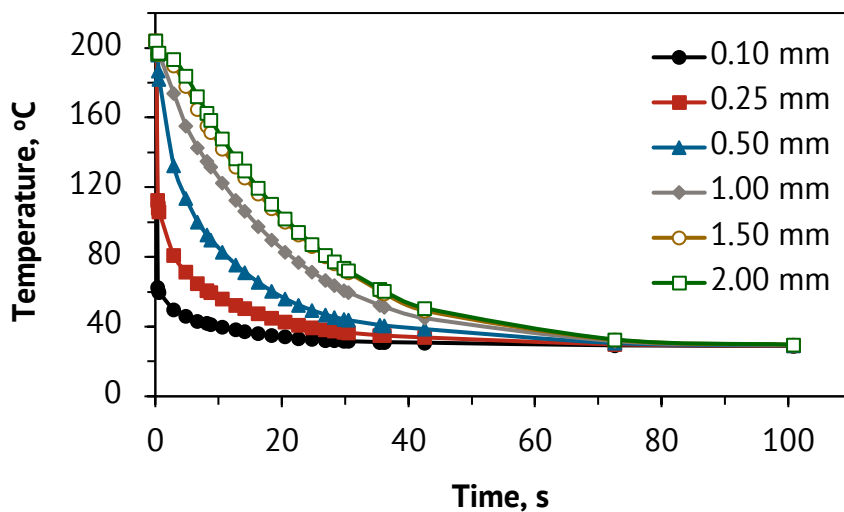
Figure 4.30: Temperature distribution profiles as a function of time at different thicknesses of the injection-molded plate from the skin (0.10 mm) to the core (2.00 mm).

According to the temperature profile, an average cooling rate can be determined along with the thickness of the injection-molded plates. The average cooling rate is calculated based on the following equation:

$$Average\ cooling\ rate\ = \frac{T_o - T_{\sim g}}{t_{\sim g} - 0.14}$$

(4.13)

where T_o is the maximum temperature measured at the gate with the filling time of 0.14 s. $T_{\sim g}$ is the measured temperature at about T_g of PLA (60–61 °C), and $t_{\sim g}$ is the cooling time to reach $T_{\sim g}$.

As seen from Table 4.6, the cooling time to reach $T_{\sim g}$ is only 0.51 s after polymer filling in the mold at the skin area. This event leads to a very high average cooling rate of up to 387.30 K/s (23,238 K/min). Even at the core area where the cooling rate is expected to be the lowest, the average cooling rate is 3.98 K/s (239 K/min). The results show that the cooling rate during injection molding is quite high in the overall studied areas. The crystallization result obtained from conventional DSC (cooling rate = 0.08 K/s or 5 K/min) might, therefore, be inadequate to fully describe the final properties (i.e., mechanical properties) of the studied materials. It should be mentioned that conventional DSC, which can provide a maximum cooling rate of fewer than 1 K/s, is generally applied in academic studies. Therefore, an advanced tool is used to mimic the crystallization behavior under the real injection molding process, which will be described in the next section.

Table 4.6: Cooling time to reach $T_{\sim g}$ ($t_{\sim g}$) and average cooling rate data obtained from simulation

Thickness of injection-molded plate, mm	$t_{\sim g}$, s	Average cooling rate, K/s
0.10 (skin)	0.51	387.30
0.25	8.15	17.85
0.50	18.43	7.85
1.00	29.81	4.82
1.50	35.50	4.06
2.00 (core)	36.21	3.98

Crystallization under Fast Cooling Conditions

As mentioned above, the advanced tool for investigating crystallization behavior in a wide range is applied. Flash DSC can be performed with a maximum cooling rate of 4000 K/s (240,000 K/min) and can imitate the crystallization behavior under real injection molding conditions [174]. Figure 4.31 shows the cooling curves obtained from Flash DSC with a cooling rate range from 0.5 K/s (30 K/min) to 500 K/s (30,000 K/min). Accordingly, the crystallization behavior can be observed within the range of cooling rates along with the thickness of the injection-molded plate. The PLA/PBAT-S1-P2 nanocomposite with the best crystallization behavior is selected for the study under fast cooling conditions. Generally, the crystallization process upon cooling is detected at approx. 102 °C using conventional DSC at a cooling rate of 0.08 K/s (5 K/min) (see Figure 4.19 and Table 4.4). However, the cooling curves obtained from Flash DSC reveal that the crystallization process cannot be detected. The results signify that the nanocomposite exhibits an amorphous material under fast cooling conditions. According to these results, it can be assumed that the crystallization behavior might not play a significant role in improving the final properties (i.e., mechanical properties) of all the studied materials obtained from the injection molding conditions used in this work.
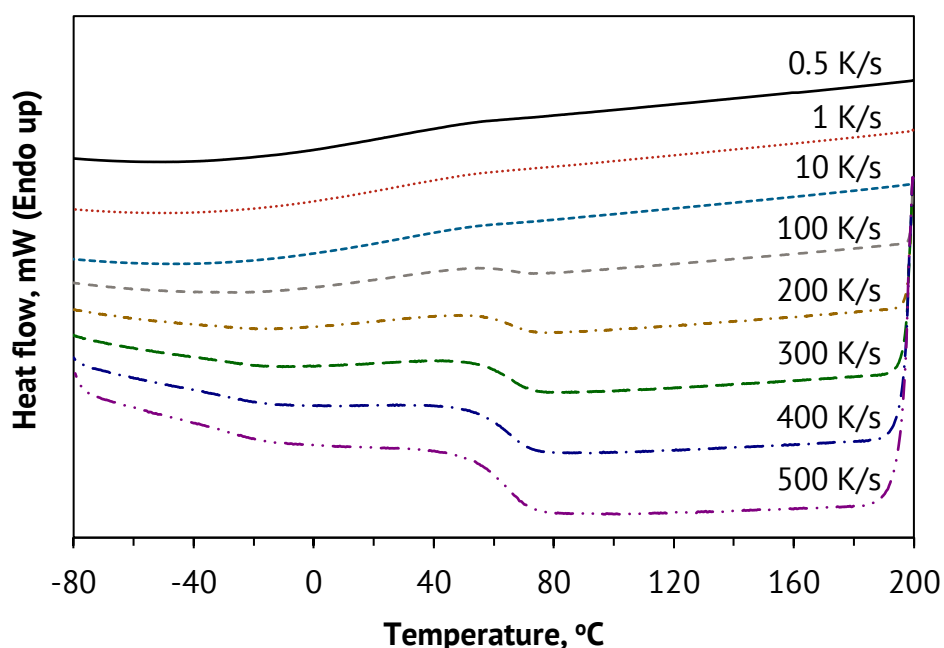
Figure 4.31:   Cooling curves of PLA/PBAT-S1-P2 measured with Flash DSC under fast cooling conditions.

4.4   Mechanical Properties

4.4.1   Tensile Properties

The tensile properties of neat PLA (PL), PLA-based nanocomposite (PL1), PLA/PBAT blend (S0), and PLA/PBAT-based nanocomposites (S1-P1, S1-P2, S1-P3, and S1-P4) are presented in Figure 4.32 (see Appendix I). As seen in Figure 4.32(a), the average stress-strain curves show two distinct behaviors shifted from brittle failure of the neat PLA and PLA-based nanocomposite to ductile failure of the PLA/PBAT blend and the blend nanocomposites. According to all the studied materials, neat PLA exhibits a high Young's modulus and tensile strength but has a very low elongation at break of about 5 %. The failure at the very low elongation at break can be attributed to the instability of the necking formation [44]. An addition of 1 vol.% nano-SiO_2 unexpectedly deteriorates the tensile properties of the PLA matrix. This behavior might be due to the poor compatibility between the polymer matrix and nanoparticles, which causes the defection and stress concentration to build up at the polymer–particle interface [175,176].

Blending PLA with 20 vol.% PBAT significantly improves the ductility of the polymer material, while the stiffness and strength worsen. It is well known that PBAT is considered as a flexible and rubbery segment dispersed in the PLA matrix. In the case of the PLA/PBAT blend, the presence of nano-SiO_2 results in an enhancement in the Young's modulus and tensile strength, although the elongation at break is yet reduced. However, good optimization of the tensile properties can be obtained compared to the neat PLA/PBAT blend when the processing procedure or the location of the nanoparticles is considered. The best compromise of Young's modulus, tensile strength, and elongation at break is acquired with PLA/PBAT-based nanocomposite P3, as seen in Figure 4.32. As described in section 4.1: Morphology, the nano-SiO_2 for nanocomposite P3 is located in the PBAT phase and at the interface between the PLA and PBAT polymers. This indicates that the tensile behavior of the PLA/PBAT-based nanocomposite is significantly improved by dispersing nano-SiO_2 in the PBAT phase and/or at the interface between the two polymers. The obtained analysis can be applied to explain the tensile properties of PLA containing 1 vol.% nano-SiO_2. It means that the nano-SiO_2 has no significant potential to improve the tensile properties of the PLA-based and PLA/PBAT-based nanocomposites when the majority of the nano-SiO_2 is located in the continuous PLA matrix. Moreover, the nanocomposite P3 exhibits a more uniform droplet size distribution so that the introduced forces are distributed more homogeneously (see section 4.1.4: Dispersed Polymer Size and Distribution). Hence, mechanical stress peaks can be reduced. Furthermore, it is

interesting to note that the miscibility behavior also plays a role in improving the tensile properties of the PLA/PBAT-based nanocomposites. According to the Han plot and van Gurp-Palmen plot, the results indicate that the nanocomposites P2 and P3 exhibit better miscibility in the phase morphology compared to the nanocomposites P1 and P4 (see section 4.2: Rheological Properties). As a result, the former nanocomposites present better tensile properties.
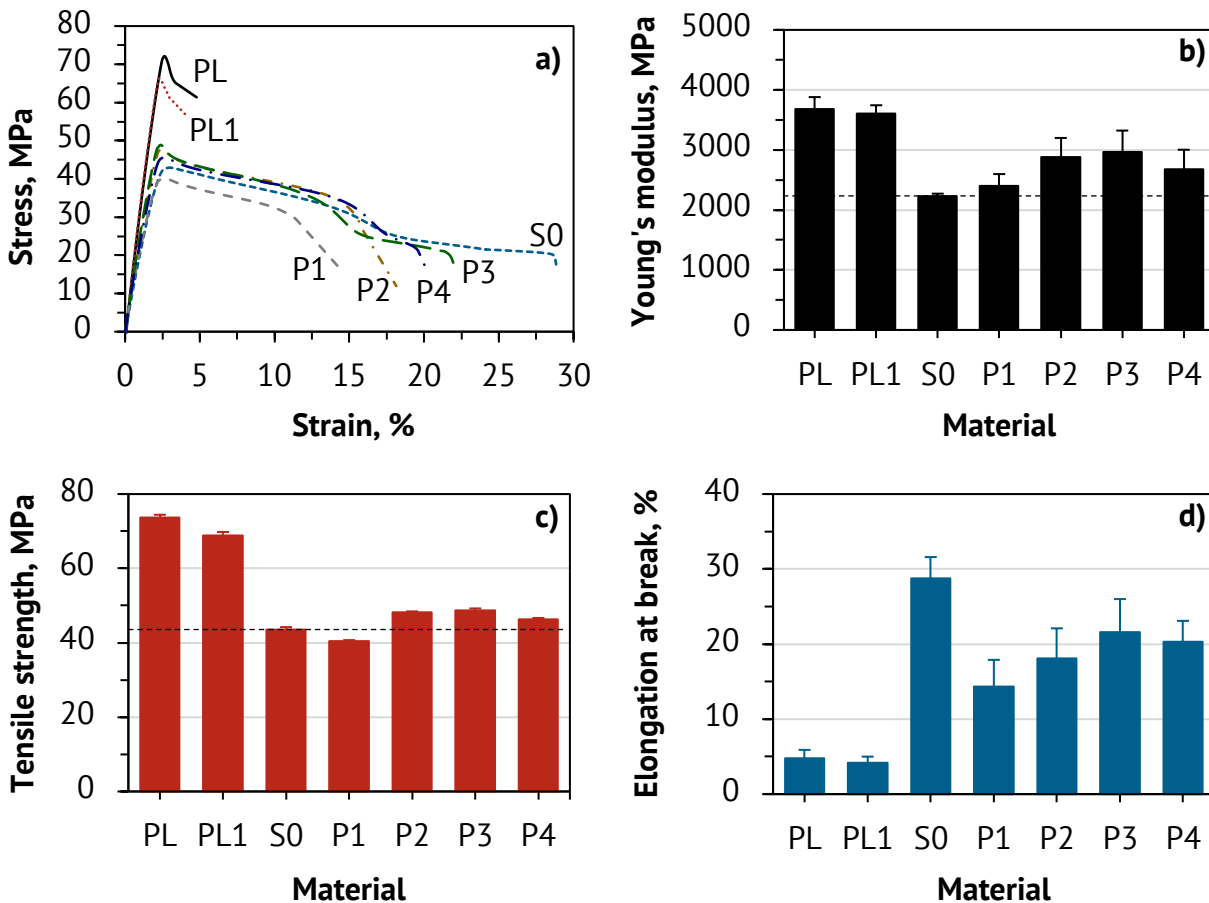
Figure 4.32: (a) Average stress-strain curves, (b) Young's modulus, (c) tensile strength, and (d) elongation at break of neat PLA (PL), PLA-S1 (PL1), PLA/PBAT blend (S0), PLA/PBAT-based nanocomposites (S1-P1, S1-P2, S1-P3, S1-P4).

Effect of Dispersed Polymer Orientation

As described earlier, the phase morphology of the PLA/PBAT blend and its nanocomposites shows the phase separation with a droplet morphology. According to the SEM images, the orientation of the dispersed PBAT droplets is parallel to the injection direction (see section 4.1: Morphology). Therefore, an anisotropic property can be obtained

from the blend and its nanocomposites. To investigate the influence of droplet orientation, tensile properties were tested in both the injection direction (ID) and transverse direction (TD).

Figure 4.33 illustrates the Young's modulus, tensile strength, and elongation at break of the blend and its nanocomposites with different tested directions. The results show that the Young's modulus and tensile strength are, overall, similar in both directions. In contrast, the elongation at break depends significantly on the testing direction. Considering that the PBAT droplet or the flexible phase orients in the testing direction, which can prolong the ductile failure in all observed materials. Hence, a distinct drop in the elongation at break is observed in the samples tested in the transverse direction.

Figure 4.33:   (a) Young's modulus, (b) tensile strength, and (c) elongation at break of PLA/PBAT blend (S0) and PLA/PBAT-based nanocomposites (S1-P1, S1-P2, S1-P3, S1-P4) with different testing directions (ID = Injection direction, TD = Transverse direction).

4.4.2   Impact Properties

The Charpy notched impact strength of all studied materials is shown in Figure 4.34 (see Appendix J). It is apparent that neat PLA and PLA filled with 1 vol.% nano-SiO_2 have a very low toughness of about 2.46 kJ/m^2 and 2.28 kJ/m^2, respectively. As expected, blending PBAT into the PLA matrix improves the impact strength by approximately 205%, indicating a more ductile fracture. The incorporation of nano-SiO_2 moderately decreases the impact strength of the neat PLA/PBAT blend. Generally, the inorganic nanofillers, which typically form aggregates and agglomerates, can restrict the mobility of the polymer matrix and limit plastic deformation. As a result, energy dissipation is reduced in the polymer matrix [177]. Surprisingly, in the case of nanocomposite P1, the impact strength slightly increases when compared to the neat blend. It is interesting that the incorporation of nano-SiO_2 into the PLA/PBAT blend can increase the toughness of the nanocomposite, where the nanoparticles are mainly dispersed in the PLA matrix and at the interface between the PLA and PBAT polymers (see section 4.1.1: Location of Nanoparticles). Meanwhile, the addition of nano-SiO_2 into a pure PLA polymer diminishes the impact strength, as seen in Figure 4.34. Based on this result, it can be inferred that the dispersed PBAT polymer and nano-SiO_2 particles have a synergistic effect in improving the energy dissipation of the PLA matrix when the proper condition of the phase morphology is reached.
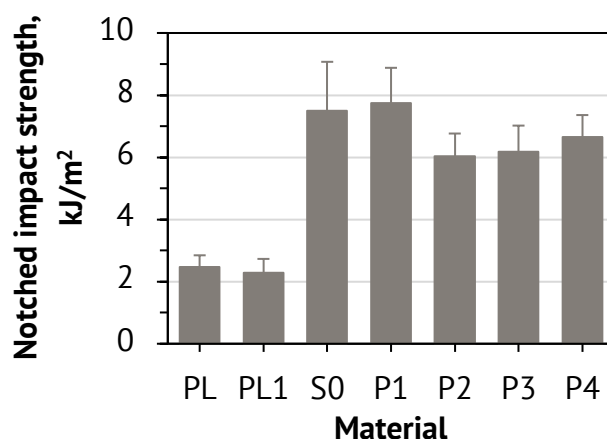
Figure 4.34:   Charpy notched impact strength of neat PLA (PL), PLA-S1 (PL1), PLA/PBAT blend (S0), PLA/PBAT-based nanocomposites (S1-P1, S1-P2, S1-P3, S1-P4).

4.5 Effect of Nanoparticle Content

4.5.1 Morphology

Location of Nanoparticles

As discussed before, the PLA/PBAT-based nanocomposites containing 1 vol.% nano-SiO_2 show a droplet morphology with a large number of nanoparticles located in the initial polymer phase and at the interface. According to the literature, it is recognized that the difference in nanoparticle loadings can alter the morphology of the polymer nanocomposites, including the dispersed droplet size and the location of the nanoparticles [136,137].

In this work, 4 vol.% nano-SiO_2 is incorporated into PLA/PBAT-based nanocomposites to investigate the effect of nanofiller content on the morphology of the nanocomposites. As seen in Figure 4.35, the droplet morphology is still observed when the nanoparticle loading increases up to 4 vol.% in all processing procedures. According to the SEM micrograph, the location of nano-SiO_2 remains unchanged, and the migration behavior seems to be similar to the nanocomposites containing 1 vol.% nano-SiO_2 (see Figure 4.2). Besides, the nanocomposites with 4 vol.% nano-SiO_2 have more and bigger nano-SiO_2 agglomerates, as indicated by the white dots.
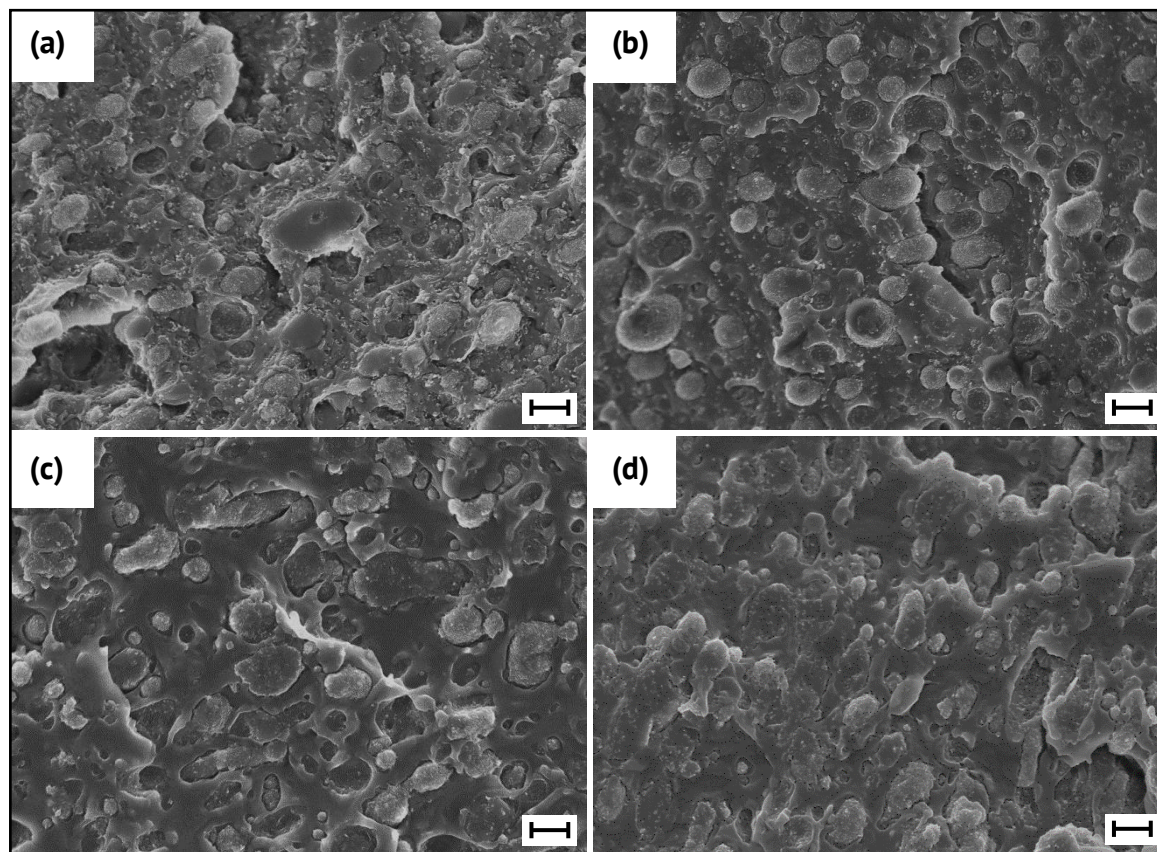
Figure 4.35:   SEM micrographs of fracture surfaces: (a) PLA/PBAT-S4-P1, (b) PLA/PBAT-S4-P2, (c) PLA/PBAT-S4-P3, and (d) PLA/PBAT-S4-P4 (scale bar = 1 μm).

4.5.2   Thermal Properties

Crystallization and Melting Behavior

The crystallization and melting behavior of PLA/PBAT-based nanocomposites containing 1 vol.% and 4 vol.% nano-SiO_2 are compared and summarized in Figures 4.36 and 4.37. It is observed that an increase in nano-SiO_2 to 4 vol.% reduces the crystallization behavior of the PLA. It is well known that an increase in nanoparticle loading results in larger agglomerates dispersed in the polymer matrix. This means that the higher number and larger size of nano-SiO_2 agglomerates restrict the mobility of PLA macromolecules, resulting in a slow crystallization rate. Accordingly, the nucleation process is confined when a lower number of individual nanoparticles is observed in the PLA matrix [9,178]. Figure 4.36(a) depicts the DSC thermograms during 2nd heating. The thermograms reveal that the cold crystallization process is provoked in the nanocomposite P2 containing 4 vol.% nano-SiO_2. Consequently, a dramatic decrease in the degree of crystallinity is observed.
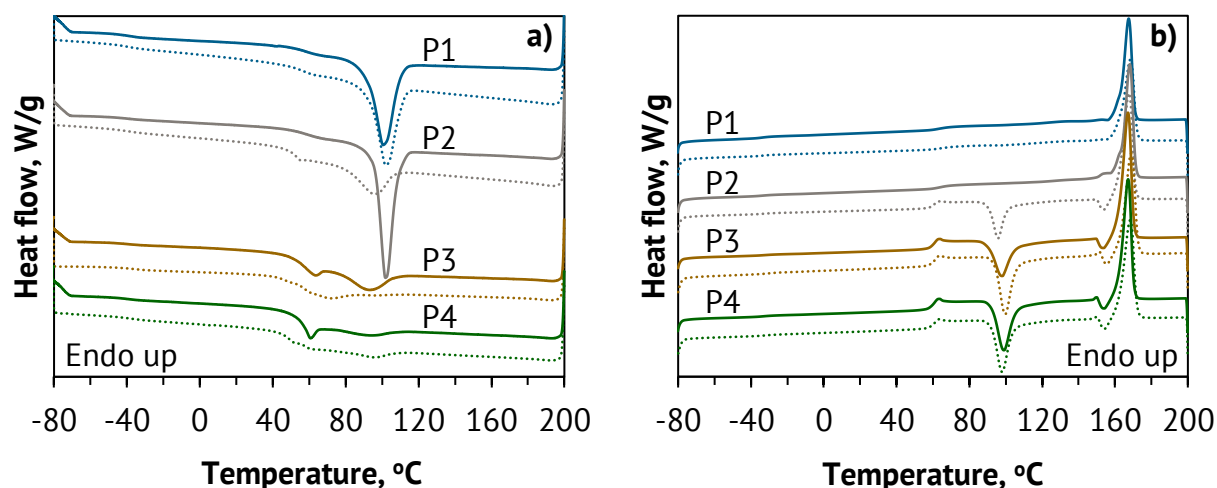
Figure 4.36: DSC thermograms during (a) 1st cooling and (b) 2nd heating scans of PLA/PBAT-based nanocomposites containing 1 vol.% (solid line) and 4 vol.% (dotted line) nano-SiO$_2$.
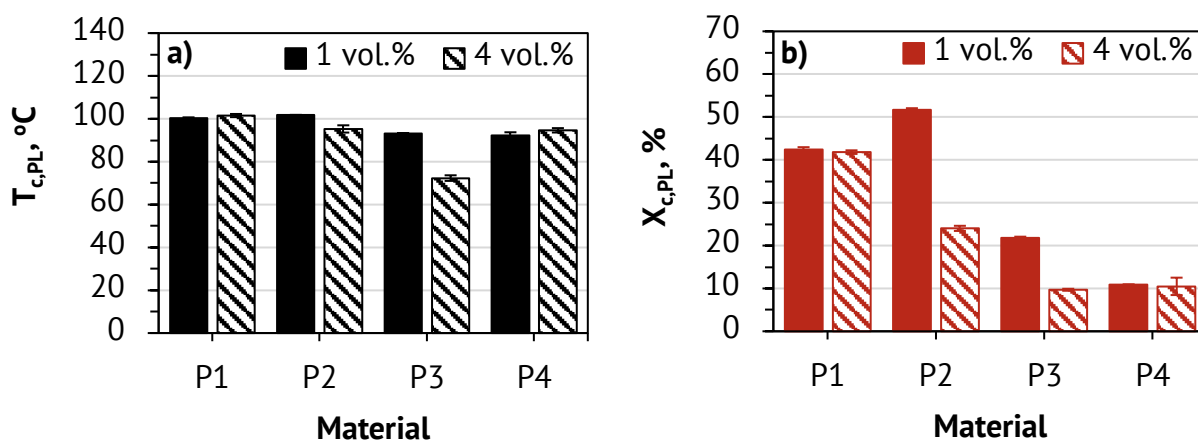
Figure 4.37: (a) Crystallization temperature ($T_{c,PL}$) and (b) degree of crystallinity ($X_{c,PL}$) of PLA/PBAT-based nanocomposites containing 1 vol.% and 4 vol.% nano-SiO$_2$.

4.5.3 Mechanical Properties

Tensile Properties

The effect of the nano-SiO$_2$ content on the tensile properties is also studied. Figure 4.38 shows the Young's modulus, tensile strength, and elongation at break of the PLA/PBAT-based nanocomposites containing 1 vol.% and 4 vol.% nano-SiO$_2$ (see Appendix I). The results show that the Young's modulus is only improved in the nanocomposite P1, in

which a large amount of nano-SiO_2 is dispersed in the PLA matrix. In the case of tensile strength, the results show an insignificant change with increasing nano-SiO_2 content. However, an increase in nano-SiO_2 significantly impairs the elongation at break of PLA/PBAT-based nanocomposites, caused by the restriction of chain mobility or plastic deformation.
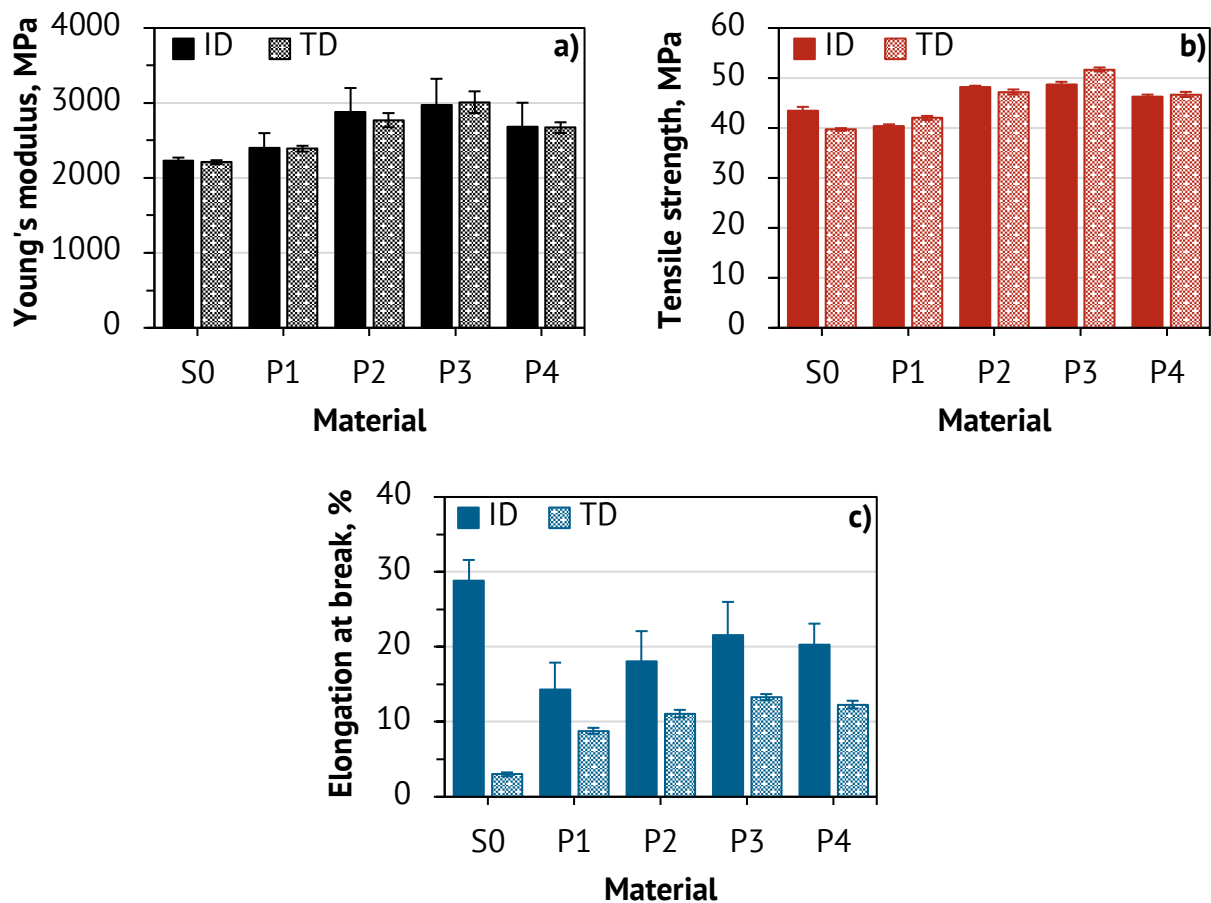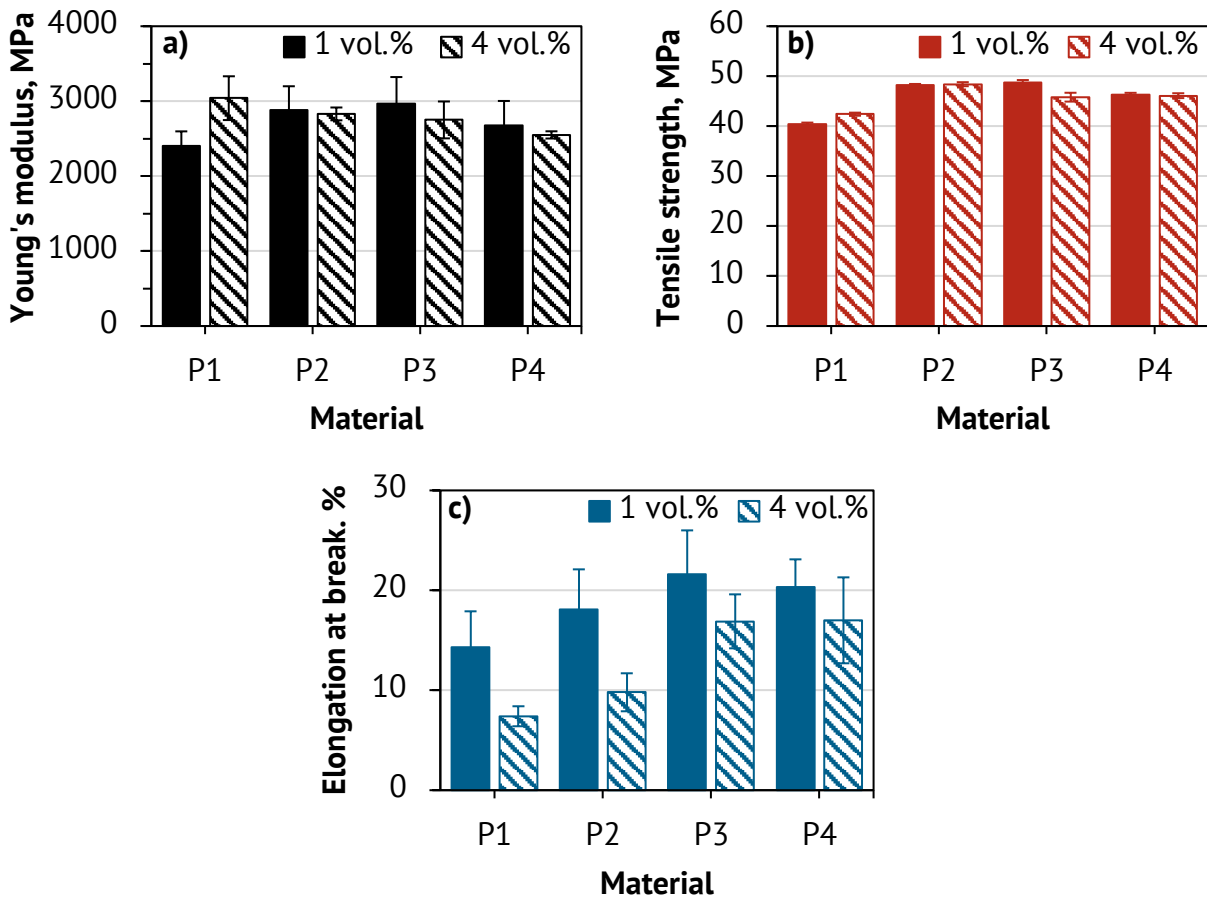
Figure 4.38:   (a) Young's modulus, (b) tensile strength, and (c) elongation at break of PLA/PBAT-based nanocomposites containing 1 vol.% and 4 vol.% nano-SiO_2.

5 Summary and Outlook

Summary

A parameter study of bioplastic-based nanocomposites was presented in terms of the process–structure–property relationships. This present work was focused on the effect of the difference in processing procedures on the morphology, thermal, rheological, and mechanical properties of the multi-phase polymer nanocomposites. PLA (matrix), PBAT (dispersed polymer), and nano-SiO$_2$ (dispersed nanofillers) were compounded using a co-rotating twin-screw extruder followed by an injection molding machine. Various blending sequences were investigated using PLA-based and PBAT-based nanocomposite masterbatches (MB-PLA and MB-PBAT).

The morphology investigation revealed that the processing strategy strongly influenced the nano-SiO$_2$ location. The nano-SiO$_2$ was exclusively located in its original polymer phase, in which the nanoparticles were introduced in the masterbatch process first, as well as at the interface between the blended polymers. By using a two-step process, the migration of nano-SiO$_2$ from the original phase to the polymer interface was observed, which was governed by its thermodynamic driving force.

The material conditions and processing history played an important role in the agglomerate size of nano-SiO$_2$. The nano-SiO$_2$ located in the PLA phase showed a significantly larger agglomerate size ($x_{50,2}$) when compared to the ones located in the PBAT phase due to the lower polymer viscosity. In addition, the agglomerate size of nano-SiO$_2$ in the PLA phase decreased with the two-step process because the forces were applied twice to break the agglomerates during compounding. In contrast, the nano-SiO$_2$ agglomerates in the PBAT phase were formed bigger with increasing residence time due to the limited area inside the PBAT droplets.

For the PBAT droplet analysis, the PLA/PBAT-based nanocomposites showed a slight increase in the number average diameter (D_n) compared to the neat PLA/PBAT blend. However, the volume average diameter (D_v) decreased significantly, leading to a marked decrease in the droplet size dispersity (d) in all the nanocomposites, especially in the one-step nanocomposite prepared by MB-PBAT (P3).

The results of the rheological properties showed that the viscosity of the neat PLA polymer was approximately ten times lower than that of the neat PBAT polymer. The incorporation of nano-SiO$_2$ increased the viscosity of all the nanocomposites. The yield point

behavior was observed, particularly in the one-step nanocomposite prepared by MB-PLA (P1), in which a large amount of nano-SiO_2 was dispersed in the PLA matrix.

The Han plot and van Gurp-Palmen plot were applied to investigate the miscibility behavior of the PLA/PBAT blend and its nanocomposites. The result revealed that the presence of nano-SiO_2 diminished the miscibility between the PLA and PBAT polymers. However, the nanocomposites P2 (two-step, MB-PLA) and P3 (one-step, MB-PBAT) exhibited better miscibility compared to the other studied nanocomposites.

The study of the thermal properties showed that the addition of nano-SiO_2 drastically facilitated the crystallization behavior of the PLA, as well as of the PBAT polymer. The synergistic effect between the dispersed PBAT polymer and the dispersed SiO_2 nanofillers improved the PLA crystallization. The best crystallization performance of PLA was obtained in the nanocomposite P2, which had the proper number and agglomerate size of nano-SiO_2 incorporated in the PLA phase. However, the simulation and fast scanning DSC data indicated that the crystallization behavior of the nanocomposites played an insignificant role in the final properties when the processing conditions of the injection molding machine that was used in this work were carried out.

To obtain the best compromise in the tensile properties, it is necessary to disperse nano-SiO_2 in the PBAT droplets and at the interface between the PLA and PBAT polymers. Accordingly, the one-step nanocomposite prepared by MB-PBAT (P3) is required. Furthermore, the agglomerate size of nano-SiO_2, the droplet size dispersity (d), and miscibility also play an essential role in balancing the stiffness/toughness ratio of the nanocomposite P3. Meanwhile, the impact properties were reduced with the presence of nano-SiO_2.

Upon increasing the nanoparticle content, a much larger nano-SiO_2 agglomerate was observed, resulting in the deterioration of the crystalline ability of PLA and the ductility of all the nanocomposites. Nevertheless, the nano-SiO_2 location remained unchanged.

Outlook

In this work, there is no information regarding the equilibrium state of nano-SiO_2 where the nanoparticles do not show further migration. More experimental studies are required to determine the amount of nano-SiO_2 at different polymer phases with increasing residence time. Based on this data, the correlation between the phase morphology (i.e., dispersion and distribution of nano-SiO_2) and material performance (i.e., mechanical properties) can be obtained.

To fully understand the mechanism of the nanofiller location in the PLA/PBAT-based nanocomposite system, the following aspects should be further investigated:

- Effect of viscosity ratio by using various molecular weights of PLA and PBAT polymers
- Effect of blending ratio between PLA and PBAT polymers
- Influence of nanofiller types (i.e., TiO_2, CNTs) and sizes
- Effect of shear rate in the twin-screw extruder (i.e., screw speed)
- Influence of compatibilizer (i.e., maleic anhydride)

The influence of the crystallization behavior depends crucially on the final processing conditions. Therefore, it would be interesting to study the different processing conditions (i.e., annealing)

According to the literature [6,179,180], there is great potential to apply PLA in 3D printing applications. It is worth transferring the knowledge related to the effect of processing procedures of PLA/PBAT-based nanocomposites and investigating the material performance using the 3D printing process.

6   References

[1]   Rhim, J.-W.; Park, H.-M.; Ha, C.-S.: Bio-nanocomposites for food packaging applications. Progress in Polymer Science 38(10–11), 1629–1652, 2013. DOI: 10.1016/j.progpolymsci.2013.05.008.

[2]   Jamshidian, M.; Tehrany, E.A.; Imran, M.; Jacquot, M.; Desobry, S.: Poly-lactic acid: Production, applications, nanocomposites, and release studies. Comprehensive Reviews in Food Science and Food Safety 9(5), 552–571, 2010. DOI: 10.1111/j.1541-4337.2010.00126.x.

[3]   Lasprilla, AJ.R.; Martinez, G.A.R.; Lunelli, B.H.; Jardini, A.L.; Filho, R.M.: Poly-lactic acid synthesis for application in biomedical devices − A review. Biotechnology Advances 30(1), 321–328, 2012. DOI: 10.1016/j.biotechadv.2011.06.019.

[4]   Lorenzo, M.L. Di; Androsch, R. eds: Industrial Applications of Poly(Lactic Acid). Springer, Cham, 2018. DOI: 10.1007/978-3-319-75459-8.

[5]   Nofar, M.; Sacligil, D.; Carreau, P.J.; Kamal, M.R.; Heuzey, M.-C.: Poly (lactic acid) blends: Processing, properties and applications. International Journal of Biological Macromolecules 125, 307–360, 2019. DOI: 10.1016/j.ijbiomac.2018.12.002.

[6]   Castro-Aguirre, E.; Iñiguez-Franco, F.; Samsudin, H.; Fang, X.; Auras, R.: Poly(lactic acid)−Mass production, processing, industrial applications, and end of life. Advanced Drug Delivery Reviews 107, 333–366, 2016. DOI: 10.1016/j.addr.2016.03.010.

[7]   Liu, H.; Zhang, J.: Research progress in toughening modification of poly(lactic acid). Journal of Polymer Science Part B: Polymer Physics 49(15), 1051–1083, 2011. DOI: 10.1002/polb.22283.

[8]   Zhao, X.; Hu, H.; Wang, X.; Yu, X.; Zhou, W.; Peng, S.: Super tough poly(lactic acid) blends: A comprehensive review. RSC Advances 10(22), 13316–13368, 2020. DOI: 10.1039/d0ra01801e.

[9]   Saiprasit, P.; Schlarb, A.K.: The effect of nanoparticle content and size on the morphology and crystallization behavior of poly(lactic acid)/silica nanocomposites. Zeitschrift Kunststofftechnik 15(5), 335–352, 2019. DOI: 10.3139/o999.01052019.

[10]   Maharana, T.; Pattanaik, S.; Routaray, A.; Nath, N.; Sutar, A.K.: Synthesis and characterization of poly(lactic acid) based graft copolymers. Reactive and Functional Polymers 93, 47–67, 2015. DOI: 10.1016/j.reactfunctpolym.2015.05.006.

[11]   Fu, S.; Sun, Z.; Huang, P.; Li, Y.; Hu, N.: Some basic aspects of polymer nanocomposites: A critical review. Nano Materials Science 1(1), 2–30, 2019. DOI: 10.1016/j.nanoms.2019.02.006.

[12]   Nazockdast, H.: Morphology and Structure of Polymer Blends Containing Nanofillers. In Isayev, A.I. (ed): Encyclopedia of Polymer Blends: Volume 3: Structure, Wiley-VCH Verlag GmbH & Co. KGaA, Weinheim, 2016. DOI: 10.1002/9783527653966.ch7.

[13]   Raquez, J.M.; Habibi, Y.; Murariu, M.; Dubois, P.: Polylactide (PLA)-based nanocomposites. Progress in Polymer Science 38(10–11), 1504–1542, 2013. DOI: 10.1016/j.progpolymsci.2013.05.014.

[14]   Wu, D.; Lin, D.; Zhang, J.; et al.: Selective localization of nanofillers: Effect on morphology and crystallization of PLA/PCL blends. Macromolecular Chemistry and Physics 212, 613–626, 2011. DOI: 10.1002/macp.201000579.

[15]   Dil, E.J.; Virgilio, N.; Favis, B.D.: The effect of the interfacial assembly of nano-silica in poly(lactic acid)/poly(butylene adipate-co-terephthalate) blends on morphology, rheology and mechanical properties. European Polymer Journal 85, 635–646, 2016. DOI: 10.1016/j.eurpolymj.2016.07.022.

[16]   Kumar, A.P.; Depan, D.; Singh Tomer, N.; Singh, R.P.: Nanoscale particles for polymer degradation and stabilization—Trends and future perspectives. Progress in Polymer Science 34(6), 479–515, 2009. DOI: 10.1016/j.progpolymsci.2009.01.002.

[17]   Bitinis, N.; Verdejo, R.; Maya, E.M.; Espuche, E.; Cassagnau, P.; Lopez-Manchado, M.A.: Physicochemical properties of organoclay filled polylactic acid/natural rubber blend bionanocomposites. Composites Science and Technology 72(2), 305–313, 2012. DOI: 10.1016/j.compscitech.2011.11.018.

[18]   Taguet, A.; Cassagnau, P.; Lopez-Cuesta, J.-M.: Structuration, selective dispersion and compatibilizing effect of (nano)fillers in polymer blends. Progress in Polymer Science 39(8), 1526–1563, 2014. DOI: 10.1016/j.progpolymsci.2014.04.002.

[19]   Li, W.; Karger-Kocsis, J.; Schlarb, A.K.: Dispersion of TiO2 particles in PET/PP/TiO2 and PET/PP/PP-g-MA/TiO2 composites prepared with different blending procedures. Macromolecular Materials and Engineering 294(9), 582–589, 2009. DOI: 10.1002/mame.200900123.

[20]   Fenouillot, F.; Cassagnau, P.; Majesté, J.-C.: Uneven distribution of nanoparticles in immiscible fluids: Morphology development in polymer blends. Polymer 50(6), 1333–1350, 2009. DOI: 10.1016/j.polymer.2008.12.029.

[21]   European Bioplastics: Bioplastics: Facts and Figures. https://www.european-bioplastics.org/news/publications/, 2020, accessed 22.6.2020.

[22]   Lyu, M.-Y.; Choi, T.G.: Research trends in polymer materials for use in lightweight

vehicles. International Journal of Precision Engineering and Manufacturing 16, 213–220, 2015. DOI: 10.1007/s12541-015-0029-x.

[23]   de Melo, E.G.; Klein, T.B.; Reinkober, S.; Gomes, J. de O.; Uhlmann, E.: Pocket milling of composite fibre-reinforced polymer using industrial robot. Procedia CIRP 85, 183–188, 2019. DOI: 10.1016/j.procir.2019.09.006.

[24]   Geyer, R.; Jambeck, J.R.; Law, K.L.: Production, use, and fate of all plastics ever made. Science Advances 3(7), e1700782, 2017. DOI: 10.1126/sciadv.1700782.

[25]   Siracusa, V.; Rocculi, P.; Romani, S.; Rosa, M.D.: Biodegradable polymers for food packaging: A review. Trends in Food Science and Technology 19(12), 634–643, 2008. DOI: 10.1016/j.tifs.2008.07.003.

[26]   Jabeen, N.; Majid, I.; Nayik, G.A.: Bioplastics and food packaging: A review. Cogent Food and Agriculture 1(1), 1117749, 2015. DOI: 10.1080/23311932.2015.1117749.

[27]   European Bioplastics: Environmental Benefits of Bioplastics. www.european-bioplastics.org, accessed 5.6.2020.

[28]   European Bioplastics: Accountability is Key: Environmental Communications Guide for Bioplastics. 2012.

[29]   Álvarez-Chávez, C.R.; Edwards, S.; Moure-Eraso, R.; Geiser, K.: Sustainability of bio-based plastics: General comparative analysis and recommendations for improvement. Journal of Cleaner Production 23(1), 47–56, 2012. DOI: 10.1016/j.jclepro.2011.10.003.

[30]   Mekonnen, T.; Mussone, P.; Khalil, H.; Bressler, D.: Progress in bio-based plastics and plasticizing modifications. Journal of Materials Chemistry A 1(43), 13379–13398, 2013. DOI: 10.1039/C3TA12555F.

[31]   European Bioplastics: Bioplastics Market Data. www.european-bioplastics.org, accessed 10.4.2020.

[32]   Babu, R.P.; O'Connor, K.; Seeram, R.: Current progress on bio-based polymers and their future trends. Progress in Biomaterials 2(8), 1–16, 2013. DOI: 10.1186/2194-0517-2-8.

[33]   Murariu, M.; Dubois, P.: PLA composites: From production to properties. Advanced Drug Delivery Reviews 107, 17–46, 2016. DOI: 10.1016/j.addr.2016.04.003.

[34]   Nampoothiri, K.M.; Nair, N.R.; John, R.P.: An overview of the recent developments in polylactide (PLA) research. Bioresource Technology 101(22), 8493–8501, 2010. DOI: 10.1016/j.biortech.2010.05.092.

[35]   Vink, E.T.H.; Rábago, K.R.; Glassner, D.A.; Gruber, P.R.: Applications of life cycle assessment to NatureWorks™ polylactide (PLA) production. Polymer Degradation and Stability 80(3), 403–419, 2003. DOI: 10.1016/S0141-3910(02)00372-5.

[36] Bonten, C.: Plastics Technology: Introduction and Fundamentals. Carl Hanser Verlag, Munich, 2019. DOI: 10.3139/9781569907689.004.

[37] Razavi, M.; Wang, S.-Q.: Why is crystalline poly(lactic acid) brittle at room temperature? Macromolecules 52(14), 5429–5441, 2019. DOI: 10.1021/acs.macromol.9b00595.

[38] Purac: PLA Serviceware in Asia. Bioplastics Magazine 8, 35, 2013.

[39] Mohan, A.M.: European Juice Packager Pioneers First Extrusion-Blown PLA Bottle. https://www.greenerpackage.com/bioplastics/european_juice_packager_pioneers_first_extrusion-blown_pla_bottle, accessed 29.7.2020.

[40] Mohan, A.M.: Danone First to Switch to PLA for Yogurt Cup in Germany. https://www.greenerpackage.com/bioplastics/danone_first_switch_pla_yogurt_cup_germany, accessed 29.7.2020.

[41] XINCHUANG BIO: PLA Mulch Film Eco Friendly Plant Ground Cover Transparent. https://www.xcbio.com/pla-mulch-film-eco-friendly-plant-ground-cover-transparent.html, accessed 28.7.2020.

[42] Xindao: ECO PLA Coffee Cup. https://www.xindao.com/en-gb/eco-pla-coffee-cup-red-p432.884, accessed 30.7.2020.

[43] TULPAR MEDICAL SOLUTIONS: Bio Absorbable Interference Screws. https://tulparmed.com/bio-absorbable-interference-screws/, accessed 28.7.2020.

[44] Jiang, L.; Wolcott, M.P.; Zhang, J.: Study of biodegradable polylactide/poly(butylene adipate-co-terephthalate) blends. Biomacromolecules 7(1), 199–207, 2006. DOI: 10.1021/bm050581q.

[45] Simões, C.L.; Viana, J.C.; Cunha, A.M.: Mechanical properties of poly(ε-caprolactone) and poly(lactic acid) blends. Journal of Applied Polymer Science 112(1), 345–352, 2009. DOI: 10.1002/app.29425.

[46] Deng, Y.; Thomas, N.L.: Blending poly(butylene succinate) with poly(lactic acid): Ductility and phase inversion effects. European Polymer Journal 71, 534–546, 2015. DOI: 10.1016/j.eurpolymj.2015.08.029.

[47] Shahlari, M.; Lee, S.: Mechanical and morphological properties of poly(butylene adipate-co-terephthalate) and poly(lactic acid) blended with organically modified silicate layers. Polymer Engineering and Science 52(7), 1420–1428, 2012. DOI: 10.1002/pen.23082.

[48] Girdthep, S.; Komrapit, N.; Molloy, R.; Lumyong, S.; Punyodom, W.; Worajittiphon, P.: Effect of plate-like particles on properties of poly(lactic acid)/poly(butylene adipate-co-terephthalate) blend: A comparative study between modified montmorillonite and graphene nanoplatelets. Composites Science and Technology 119, 115–123, 2015. DOI: 10.1016/j.compscitech.2015.10.005.

[49]   Nofar, M.; Heuzey, M.-C.; Carreau, P.J.; Kamal, M.R.: Effects of nanoclay and its localization on the morphology stabilization of PLA/PBAT blends under shear flow. Polymer 98, 353–364, 2016. DOI: 10.1016/j.polymer.2016.06.044.

[50]   Urquijo, J.; Aranburu, N.; Dagréou, S.; Guerrica-Echevarría, G.; Eguiazábal, J.I.: CNT-induced morphology and its effect on properties in PLA/PBAT-based nanocomposites. European Polymer Journal 93, 545–555, 2017. DOI: 10.1016/j.eurpolymj.2017.06.035.

[51]   Arrieta, M.P.; Fortunati, E.; Dominici, F.; Rayón, E.; López, J.; Kenny, J.M.: Multifunctional PLA–PHB/cellulose nanocrystal films: Processing, structural and thermal properties. Carbohydrate Polymers 107, 16–24, 2014. DOI: 10.1016/j.carbpol.2014.02.044.

[52]   Dil, E.J.; Favis, B.D.: Localization of micro- and nano-silica particles in heterophase poly(lactic acid)/poly(butylene adipate-co-terephthalate) blends. Polymer 76, 295–306, 2015. DOI: 10.1016/j.polymer.2015.08.046.

[53]   Harrats, C.; Thomas, S.; Groeninckx, G. eds: Micro- and Nanostructured Multiphase Polymer Blend Systems: Phase Morphology and Interfaces. Taylor & Francis, Florida, 2005. DOI: 10.1002/macp.200600584.

[54]   Robeson, L.M.: Polymer Blends: A Comprehensive Review. Carl Hanser Verlag, Munich, 2007.

[55]   Nara, S.; Oyama, H.T.: Effects of partial miscibility on the structure and properties of novel high performance blends composed of poly(p-phenylene sulfide) and poly(phenylsulfone). Polymer Journal 46, 568–575, 2014. DOI: 10.1038/pj.2014.21.

[56]   Gibbs, J.W.: A method of geometrical representation of the thermodynamic properties of substances by means of surfaces. Transactions of the Connecticut Academy of Arts and Sciences 2, 382–404, 1873.

[57]   Qian, C.; Mumby, S.J.; Eichinger, B.E.: Phase diagrams of binary polymer solutions and blends. Macromolecules 24(7), 1655–1661, 1991. DOI: 10.1021/ma00007a031.

[58]   Flory, P.J.: Thermodynamics of high polymer solutions. The Journal of Chemical Physics 10(1), 51–61, 1942. DOI: 10.1063/1.1723621.

[59]   Huggins, M.L.: Some properties of solutions of long-chain compounds. The Journal of Physical Chemistry 46(1), 151–158, 1942. DOI: 10.1021/j150415a018.

[60]   Saini, P.; Arora, M.; Kumar, M.N.V.R.: Poly(lactic acid) blends in biomedical applications. Advanced Drug Delivery Reviews 107, 47–59, 2016. DOI: 10.1016/j.addr.2016.06.014.

[61]   Xavier, S.F.: Properties and Performance of Polymer Blends. In Utracki, L.A. (ed): Polymer Blends Handbook, Kluwer Academic Publishers, Dordrecht, 2002. DOI: 10.1007/0-306-48244-4.

[62] Sundararaj, U.; Macosko, C.W.: Drop breakup and coalescence in polymer blends: The effects of concentration and compatibilization. Macromolecules 28(8), 2647–2657, 1995. DOI: 10.1021/ma00112a009.

[63] Macosko, C.W.: Morphology development and control in immiscible polymer blends. Macromolecular Symposia 149(1), 171–184, 2000. DOI: 10.1002/1521-3900(200001)149:1<171::AID-MASY171>3.0.CO;2-8.

[64] Pötschke, P.; Paul, D.R.: Formation of co-continuous structures in melt-mixed immiscible polymer blends. Journal of Macromolecular Science, Part C: Polymer Reviews 43(1), 87–141, 2003. DOI: 10.1081/MC-120018022.

[65] Li, K.; Peng, J.; Turng, L.-S.; Huang, H.-X.: Dynamic rheological behavior and morphology of polylactide/poly(butylenes adipate-co-terephthalate) blends with various composition ratios. Advances in Polymer Technology 30(2), 150–157, 2011. DOI: 10.1002/adv.20212.

[66] Deng, Y.; Yu, C.; Wongwiwattana, P.; Thomas, N.L.: Optimising ductility of poly(lactic acid)/poly(butylene adipate-co-terephthalate) blends through co-continuous phase morphology. Journal of Polymers and the Environment 26, 3802–3816, 2018. DOI: 10.1007/s10924-018-1256-x.

[67] Huang, S.; Bai, L.; Trifkovic, M.; Cheng, X.; Macosko, C.W.: Controlling the morphology of immiscible cocontinuous polymer blends via silica nanoparticles jammed at the interface. Macromolecules 49, 3911–3918, 2016. DOI: 10.1021/acs.macromol.6b00212.

[68] Willemse, R.C.; de Boer, A.P.; van Dam, J.; Gotsis, A.D.: Co-continuous morphologies in polymer blends: The influence of the interfacial tension. Polymer 40(4), 827–834, 1999. DOI: 10.1016/S0032-3861(98)00307-3.

[69] Épinat, C.: Morphology Development and Rheological Properties of Reactively Compatibilized Polyamide 6/High Density Polyethylene Blends. Université Claude Bernard - Lyon I, 2014.

[70] Laboratoire Polymère et Matériaux Avancés (LPMA) - Solvay: Heterogeneous Polymer Systems: Polymer Blends and Dispersion of Nano-Fillers, Blends. https://www.lpma-research.com/en/research/heterogeneous-polymer-systems/Blend_Article.html, accessed 18.9.2020.

[71] Willemse, R.C.; de Boer, A.P.; van Dam, J.; Gotsis, A.D.: Co-continuous morphologies in polymer blends: A new model. Polymer 39(24), 5879–5887, 1998. DOI: 10.1016/S0032-3861(97)10200-2.

[72] Macosko, C.W.; Guégan, P.; Khandpur, A.K.; Nakayama, A.; Marechal, P.; Inoue, T.: Compatibilizers for melt blending: Premade block copolymers. Macromolecules 29(17), 5590–5598, 1996. DOI: 10.1021/ma9602482.

[73] Scott, C.E.; Macosko, C.W.: Model experiments concerning morphology development during the initial stages of polymer blending. Polymer Bulletin 26, 341–348, 1991. DOI: 10.1007/BF00587979.

[74] Fortelný, I.; Kovář, J.; Stephan, M.: Analysis of the phase structure development during the melt mixing of polymer blends. Journal of Elastomers and Plastics 28(2), 106–139, 1996. DOI: 10.1177/009524439602800202.

[75] Tokita, N.: Analysis of morphology formation in elastomer blends. Rubber Chemistry and Technology 50(2), 292–300, 1977. DOI: 10.5254/1.3535144.

[76] Starý, Z.: Thermodynamics and Morphology and Compatibilization of Polymer Blends. In Thomas, S.; Grohens, Y.; Jyotishkumar, P. (eds): Characterization of Polymer Blends: Miscibility, Morphology and Interfaces, Wiley-VCH Verlag GmbH & Co. KGaA, Weinheim, 2015. DOI: 10.1002/9783527645602.ch03.

[77] Taylor, G.I.: The formation of emulsions in definable fields of flow. Proceedings of the Royal Society A: Mathematical, Physical and Engineering Sciences 146(858), 501–523, 1934. DOI: 10.1098/rspa.1934.0169.

[78] Grace, H.P.: Dispersion phenomena in high viscosity immiscible fluid systems and application of static mixers as dispersion devices in such systems. Chemical Engineering Communications 14(3–6), 225–277, 1982. DOI: 10.1080/00986448208911047.

[79] García-Masabet, V.; Pérez, O.S.; Cailloux, J.; et al.: PLA/PA bio-blends: Induced morphology by extrusion. Polymers 12(1), 10, 2020. DOI: 10.3390/polym12010010.

[80] de Bruijn, R.A.: Deformation and breakup of drops in simple shear flows. Technische Universiteit Eindhoven, 1989. DOI: 10.6100/IR318702.

[81] Utracki, L.A.; Shi, Z.H.: Development of polymer blend morphology during compounding in a twin-screw extruder. Part I: Droplet dispersion and coalescence – A review. Polymer Engineering and Science 32(24), 1824–1833, 1992. DOI: 10.1002/pen.760322405.

[82] Fortelný, I.; Jůza, J.: Description of the droplet size evolution in flowing immiscible polymer blends. Polymers 11(5), 761, 2019. DOI: 10.3390/polym11050761.

[83] Chesters, A.K.: The modelling of coalescence processes in fluid-liquid dispersions: A review of current understanding. Chemical Engineering Research and Design 69(A4), 259–270, 1991.

[84] Fortelný, I.; Jůza, J.; Dimzoski, B.: Coalescence in quiescent polymer blends with a high content of the dispersed phase. European Polymer Journal 48(7), 1230–1240, 2012. DOI: 10.1016/j.eurpolymj.2012.04.017.

[85] Shchipunov, Y.: Bionanocomposites: Green sustainable materials for the near future. Pure and Applied Chemistry 84(12), 2579–2607, 2012. DOI: 10.1351/PAC-

CON-12-05-04.

[86] Jiang, L.; Liu, B.; Zhang, J.: Properties of poly(lactic acid)/poly(butylene adipate-co-terephthalate)/nanoparticle ternary composites. Industrial and Engineering Chemistry Research 48(16), 7594–7602, 2009. DOI: 10.1021/ie900576f.

[87] Lee, T.-W.; Jeong, Y.G.: Enhanced electrical conductivity, mechanical modulus, and thermal stability of immiscible polylactide/polypropylene blends by the selective localization of multi-walled carbon nanotubes. Composites Science and Technology 103, 78–84, 2014. DOI: 10.1016/j.compscitech.2014.08.019.

[88] Yu, F.; Huang, H.-X.: Simultaneously toughening and reinforcing poly(lactic acid)/thermoplastic polyurethane blend via enhancing interfacial adhesion by hydrophobic silica nanoparticles. Polymer Testing 45, 107–113, 2015. DOI: 10.1016/j.polymertesting.2015.06.001.

[89] Cassagnau, P.: Melt rheology of organoclay and fumed silica nanocomposites. Polymer 49(9), 2183–2196, 2008. DOI: 10.1016/j.polymer.2007.12.035.

[90] Wen, X.; Zhang, K.; Wang, Y.; et al.: Study of the thermal stabilization mechanism of biodegradable poly(L-lactide)/silica nanocomposites. Polymer International 60(2), 202–210, 2011. DOI: 10.1002/pi.2927.

[91] Suksut, B.: Morphology and Morphology Formation of Injection Molded PP-Based Nanocomposites. Technische Universität Kaiserslautern, 2016.

[92] Ginzburg, V. V.: Nanoparticle/Polymer Blends: Theory and Modeling. In Isayev, A.I. (ed): Encyclopedia of Polymer Blends, Volume 1: Fundamentals, Wiley-VCH Verlag GmbH & Co. KGaA, Weinheim, 2010.

[93] Wu, J.-H.; Yen, M.-S.; Kuo, M.C.; Chen, B.-H.: Physical properties and crystallization behavior of silica particulates reinforced poly(lactic acid) composites. Materials Chemistry and Physics 142(2–3), 726–733, 2013. DOI: 10.1016/j.matchemphys.2013.08.031.

[94] Evonik Industries: Technical Information of Partcles Supplier, Silica and Metal Oxides. Hanau, Germany.

[95] Dorigato, A.; Sebastiani, M.; Pegoretti, A.; Fambri, L.: Effect of silica nanoparticles on the mechanical performances of poly (lactic acid). Journal of Polymers and the Environment 20, 713–725, 2012. DOI: 10.1007/s10924-012-0425-6.

[96] Lin, L.; Suksut, B.; Schlarb, A.K.: Process–Structure–Property Relationships in Semicrystalline Polymer-Based Nanocomposites. In Mittal, V. (ed): Manufacturing of Nanocomposites with Engineering Plastics, Woodhead Publishing, 2015. DOI: 10.1016/B978-1-78242-308-9.00012-4.

[97] Knör, N.; Haupert, F.; Schlarb, A.K.: Nanoverbundwerkstoffe-eine neue Materialklasse mit verbesserter Steifigkeit-/Zähigkeitsrelation. IVW Kolloquium 9–

23, 2008.

[98]   Saiprasit, P.; Schlarb, A.K.: The effect of the compounding procedure on the morphology and mechanical properties of PLA/PBAT-based nanocomposites. International Polymer Processing 36(2), 219–227, 2021. DOI: doi:10.1515/ipp-2020-4032.

[99]   Salehiyan, R.; Ray, S.S.: Tuning the conductivity of nanocomposites through nanoparticle migration and interface crossing in immiscible polymer blends: A review on fundamental understanding. Macromolecular Materials and Engineering 304(2), 1800431, 2019. DOI: 10.1002/mame.201800431.

[100]   Sumita, M.; Sakata, K.; Asai, S.; Miyasaka, K.; Nakagawa, H.: Dispersion of fillers and the electrical conductivity of polymer blends filled with carbon black. Polymer Bulletin 25(2), 265–271, 1991. DOI: 10.1007/BF00310802.

[101]   Heshmati, V.; Kamal, M.R.; Favis, B.D.: Cellulose nanocrystal in poly(lactic acid)/polyamide11 blends: Preparation, morphology and co-continuity. European Polymer Journal 98, 11–20, 2018. DOI: 10.1016/j.eurpolymj.2017.10.027.

[102]   Urquijo, J.; Dagréou, S.; Guerrica-Echevarría, G.; Eguiazábal, J.I.: Structure and properties of poly(lactic acid)/poly(ε-caprolactone) nanocomposites with kinetically induced nanoclay location. Journal of Applied Polymer Science 133(33), 43815, 2016. DOI: 10.1002/app.43815.

[103]   Persson, A.L.; Bertilsson, H.: Viscosity difference as distributing factor in selective absorption of aluminium borate whiskers in immiscible polymer blends. Polymer 39(23), 5633–5642, 1998. DOI: 10.1016/S0032-3861(98)00096-2.

[104]   Feng, J.; Chan, C.; Li, J.: A method to control the dispersion of carbon black in an immiscible polymer blend. Polymer Engineering and Science 43(5), 1058–1063, 2003. DOI: 10.1002/pen.10089.

[105]   Ojijo, V.; Malwela, T.; Ray, S.S.; Sadiku, R.: Unique isothermal crystallization phenomenon in the ternary blends of biopolymers polylactide and poly[(butylene succinate)-co-adipate] and nano-clay. Polymer 53(2), 505–518, 2012. DOI: 10.1016/j.polymer.2011.12.007.

[106]   Elias, L.; Fenouillot, F.; Majesté, J.C.; Martin, G.; Cassagnau, P.: Migration of nanosilica particles in polymer blends. Journal of Polymer Science Part B: Polymer Physics 46(18), 1976–1983, 2008. DOI: 10.1002/polb.21534.

[107]   Persson, A.L.; Bertilsson, H.: Morphological effects in SAN-PA6 blends induced by aluminum borate whiskers. Composite Interfaces 3(4), 321–332, 1995. DOI: 10.1163/156855495X00101.

[108]   NatureWorks: Technical Data Sheet, Ingeo™ Biopolymer 3251D. www.natureworksllc.com.

[109] BASF SE: Product Information, ecoflex F Blend C1200. www.basf.com.

[110] Evonik Industries: Product Information, AEROSIL R 8200. www.aerosil.com.

[111] van Krevelen, D.W.: Properties of Polymers. Elsevier, Amsterdam, 1997. DOI: 10.1016/B978-0-444-82877-4.50002-0.

[112] Auld, B.A.: Acoustic Fields and Waves in Solids. Wiley, New York, 1973.

[113] Carlotti, G.; Doucet, L.; Dupeux, M.: Elastic properties of silicon dioxide films deposited by chemical vapour deposition from tetraethylorthosilicate. Thin Solid Films 296(1–2), 102–105, 1997. DOI: 10.1016/S0040-6090(96)09346-7.

[114] Underwood, E.E.: Particle-Size Distribution. In DeHoff, R.T.; Rhines, F.N. (eds): Quantitative Microscopy, Mcgraw-Hill, New York, 1968.

[115] Owens, D.K.; Wendt, R.C.: Estimation of the surface free energy of polymers. Journal of Applied Polymer Science 13, 1741–1747, 1969. DOI: 10.1002/app.1969.070130815.

[116] Fowkes, F.M.: Determination of interfacial tensions, contact angles, and dispersion forces in surfaces by assuming additivity of intermolecular interactions in surfaces. The Journal of Physical Chemistry 66(2), 382, 1962. DOI: 10.1021/j100808a524.

[117] Dalal, E.N.: Calculation of solid surface tensions. Langmuir 3(6), 1009–1015, 1987. DOI: 10.1021/la00078a023.

[118] Brandrup, J.; Immergut, E.H. eds: Polymer Handbook: Third Edition. John Wiley and Sons, New York, 1989. DOI: 10.1002/actp.1990.010410614.

[119] Elias, L.; Fenouillot, F.; Majeste, J.C.; Cassagnau, P.: Morphology and rheology of immiscible polymer blends filled with silica nanoparticles. Polymer 48(20), 6029–6040, 2007. DOI: 10.1016/j.polymer.2007.07.061.

[120] Wu, S.: Polymer Interface and Adhesion. Taylor & Francis, Florida, 1982. DOI: 10.1201/9780203742860.

[121] Najafi, N.; Heuzey, M.C.; Carreau, P.J.: Crystallization behavior and morphology of polylactide and PLA/clay nanocomposites in the presence of chain extenders. Polymer Engineering and Science 53(5), 1053–1064, 2013. DOI: 10.1002/pen.23355.

[122] Zhou, H.; Green, T.B.; Joo, Y.L.: The thermal effects on electrospinning of polylactic acid melts. Polymer 47(21), 7497–7505, 2006. DOI: 10.1016/j.polymer.2006.08.042.

[123] Schawe, J.E.K.: Practical aspects of the Flash DSC 1: Sample preparation for measurements of polymers. Thermal Analysis UserCom 36, 17–24, 2012.

[124] Poel, G. Vanden; Istrate, D.; Magon, A.; Mathot, V.: Performance and calibration of

the Flash DSC 1, a new, MEMS-based fast scanning calorimeter. Journal of Thermal Analysis and Calorimetry 110, 1533–1546, 2012. DOI: 10.1007/s10973-012-2722-7.

[125] Sezen, M.: Focused Ion Beams (FIB) – Novel Methodologies and Recent Applications for Multidisciplinary Sciences. In Janecek, M.; Kral, R. (eds): Modern Electron Microscopy in Physical and Life Sciences, IntechOpen, 2016. DOI: 10.5772/61634.

[126] Ess, J.W.; Hornsby, P.R.: Twin-screw extrusion compounding of mineral filled thermoplastics: Dispersive mixing effect. Plastics and Rubber Processing and Applications 8(3), 147–156, 1987.

[127] Schlarb, A.K.: Perspektiven der Kunststofftechnik im Zusammenwirken von Werkstoff und Verarbeitung. Aachen, 2008.

[128] Hassinger, I.; Burkhart, T.: Multiple extrusion and dilution of nanocomposites and their effect on the mechanical properties. Journal of Thermoplastic Composite Materials 25(5), 573–590, 2011. DOI: 10.1177/0892705711412646.

[129] Hassinger, I.: Analyse und Entwicklung des Extrusionsprozesses zur Erhöhung der Dispersionsqualität von Nanopartikel-Polyamid 6-Verbundwerkstoffen. Technische Universität Kaiserslautern, 2013.

[130] von Smoluchowski, M.: Versuch einer mathematischen Theorie der Koagulationskinetik kolloider Lösungen. Zeitschrift für Physikalische Chemie 92U(1), 129–168, 1917. DOI: 10.1515/zpch-1918-9209.

[131] Nagarkar, S.; Velankar, S.S.: Rheology and morphology of model immiscible polymer blends with monodisperse spherical particles at the interface. Journal of Rheology 57(3), 901–926, 2013. DOI: 10.1122/1.4801757.

[132] Santos, R.M.; Vilaverde, C.; Cunha, E.; Paiva, M.C.; Covas, J.A.: Probing dispersion and re-agglomeration phenomena upon melt-mixing of polymer-functionalized graphite nanoplates. Soft Matter 12(1), 77–86, 2016. DOI: 10.1039/c5sm01366f.

[133] Ma, P.-C.; Mo, S.-Y.; Tang, B.-Z.; Kim, J.-K.: Dispersion, interfacial interaction and re-agglomeration of functionalized carbon nanotubes in epoxy composites. Carbon 48(6), 1824–1834, 2010. DOI: 10.1016/j.carbon.2010.01.028.

[134] Wu, D.; Zhang, Y.; Zhang, M.; Yu, W.: Selective localization of multiwalled carbon nanotubes in poly(ε-caprolactone)/polylactide blend. Biomacromolecules 10(2), 417–424, 2009. DOI: 10.1021/bm801183f.

[135] Elias, L.; Fenouillot, F.; Majesté, J.C.; Alcouffe, P.; Cassagnau, P.: Immiscible polymer blends stabilized with nano-silica particles: Rheology and effective interfacial tension. Polymer 49(20), 4378–4385, 2008. DOI: 10.1016/j.polymer.2008.07.018.

[136] Filippone, G.; Dintcheva, N.T.; La Mantia, F.P.; Acierno, D.: Using organoclay to

promote morphology refinement and co-continuity in high-density polyethylene/polyamide 6 blends - Effect of filler content and polymer matrix composition. Polymer 51(17), 3956–3965, 2010. DOI: 10.1016/j.polymer.2010.06.044.

[137] Hong, J.S.; Namkung, H.; Ahn, K.H.; Lee, SJ.; Kim, C.: The role of organically modified layered silicate in the breakup and coalescence of droplets in PBT/PE blends. Polymer 47(11), 3967–3975, 2006. DOI: 10.1016/j.polymer.2006.03.077.

[138] Harnby, N.; Edwards, M.F.; Nienow, A.W. eds: Mixing in the Process Industries. Butterworth-Heinemann, Oxford, 1997. DOI: 10.1016/B978-0-7506-3760-2.X5020-3.

[139] Wu, S.: A generalized criterion for rubber toughening: The critical matrix ligament thickness. Journal of Applied Polymer Science 35(2), 549–561, 1988. DOI: 10.1002/app.1988.070350220.

[140] Göttermann, S.; Standau, T.; Weinmann, S.; Altstädt, V.; Bonten, C.: Effect of chemical modification on the thermal and rheological properties of polylactide. Polymer Engineering and Science 57(11), 1242–1251, 2017. DOI: 10.1002/pen.24505.

[141] Al-Itry, R.; Lamnawar, K.; Maazouz, A.: Improvement of thermal stability, rheological and mechanical properties of PLA, PBAT and their blends by reactive extrusion with functionalized epoxy. Polymer Degradation and Stability 97(10), 1898–1914, 2012. DOI: 10.1016/j.polymdegradstab.2012.06.028.

[142] Arraiza, A.L.; Sarasua, J.R.; Verdu, J.; Colin, X.: Rheological behavior and modeling of thermal degradation of poly(ε-caprolactone) and poly(L-lactide). International Polymer Processing 22(5), 389–394, 2007. DOI: 10.3139/217.2067.

[143] Yan, S.; Yin, J.; Yang, J.; Chen, X.: Structural characteristics and thermal properties of plasticized poly(l-lactide)-silica nanocomposites synthesized by sol–gel method. Materials Letters 61(13), 2683–2686, 2007. DOI: 10.1016/j.matlet.2006.10.023.

[144] Huang, J.-W.; Hung, Y.C.; Wen, Y.-L.; Kang, C.-C.; Yeh, M.-Y.: Polylactide/nano and microscale silica composite films. I. Preparation and characterization. Journal of Applied Polymer Science 112(3), 1688–1694, 2009. DOI: 10.1002/app.29616.

[145] Cox, W.P.; Merz, E.H.: Correlation of dynamic and steady flow viscosities. Journal of Polymer Science 28(118), 619–622, 1958. DOI: 10.1002/pol.1958.1202811812.

[146] Rueda, M.M.; Auscher, M.-C.; Fulchiron, R.; et al.: Rheology and applications of highly filled polymers: A review of current understanding. Progress in Polymer Science 66, 22–53, 2017. DOI: 10.1016/j.progpolymsci.2016.12.007.

[147] Freitas, A.L.P. de L.; Filho, L.R.T.; Calvão, P.S.; de Souza, A.M.C.: Effect of montmorillonite and chain extender on rheological, morphological and biodegradation behavior of PLA/PBAT blends. Polymer Testing 62, 189–195, 2017.

DOI: 10.1016/j.polymertesting.2017.06.030.

[148] Nofar, M.; Maani, A.; Sojoudi, H.; Heuzey, M.C.; Carreau, P.J.: Interfacial and rheological properties of PLA/PBAT and PLA/PBSA blends and their morphological stability under shear flow. Journal of Rheology 59(2), 317–333, 2015. DOI: 10.1122/1.4905714.

[149] Jafari, S.H.; Hesabi, M.N.; Ali-Khonakdar, H.; Asl-Rahimi, M.: Correlation of rheology and morphology and estimation of interfacial tension of immiscible COC/EVA blends. Journal of Polymer Research 18(4), 821–831, 2011. DOI: 10.1007/s10965-010-9479-0.

[150] Zhao, J.; Li, X.; Pan, H.; et al.: Rheological, thermal and mechanical properties of biodegradable poly(lactic acid)/poly(butylene adipate-co-terephthalate)/poly(propylene carbonate) polyurethane trinary blown films. Polymer Bulletin 77, 4235–4258, 2020. DOI: 10.1007/s00289-019-02942-5.

[151] Mohammadi, M.; Yousefi, A.A.; Ehsani, M.: Thermorheological analysis of blend of high-and low-density polyethylenes. Journal of Polymer Research 19(2), 9798, 2012. DOI: 10.1007/s10965-011-9798-9.

[152] Zhao, Y.; Lang, X.; Pan, H.; et al.: Effect of mixing poly(lactic acid) with glycidyl methacrylate grafted poly(ethylene octene) on optical and mechanical properties of the blown films. Polymer Engineering and Science 55(12), 2801–2813, 2015. DOI: 10.1002/pen.24171.

[153] Hoseini, M.; Haghtalab, A.; Famili, M.H.N.: Rheology and morphology study of immiscible linear low-density polyethylene/poly(lactic acid) blends filled with nanosilica particles. Journal of Applied Polymer Science 134(46), 45526, 2017. DOI: 10.1002/app.45526.

[154] Salehiyan, R.; Ray, S.S.; Stadler, F.J.; Ojijo, V.: Rheology-microstructure relationships in melt-processed polylactide/poly(vinylidene fluoride) blends. Materials 11(12), 2450, 2018. DOI: 10.3390/ma11122450.

[155] Wen, X.; Lin, Y.; Han, C.; et al.: Thermomechanical and optical properties of biodegradable poly(L-lactide)/silica nanocomposites by melt compounding. Journal of Applied Polymer Science 114(6), 3379–3388, 2009. DOI: 10.1002/app.30896.

[156] Salehiyan, R.; Ray, S.S.: Influence of nanoclay localization on structure–property relationships of polylactide-based biodegradable blend nanocomposites. Macromolecular Materials and Engineering 303(7), 1800134, 2018. DOI: 10.1002/mame.201800134.

[157] Leoné, N.; Roy, M.; Saidi, S.; de Kort, G.; Hermida-Merino, D.; Wilsens, C.H.R.M.: Improving processing, crystallization, and performance of poly-l-lactide with an amide-based organic compound as both plasticizer and nucleating agent. ACS

Omega 4(6), 10376–10387, 2019. DOI: 10.1021/acsomega.9b00848.

[158] Crone, G.; Natansohn, A.: Compatibilization of poly(methyl acrylate) and polysterene through charge transfer interactions. Polymer Bulletin 27, 73–80, 1991. DOI: 10.1007/BF00296328.

[159] Kilic, N.T.; Can, B.N.; Kodal, M.; Ozkoc, G.: Compatibilization of PLA/PBAT blends by using Epoxy-POSS. Journal of Applied Polymer Science 136(12), 47217, 2019. DOI: 10.1002/app.47217.

[160] Androsch, R.; Schick, C.; Lorenzo, M.L. Di: Melting of conformationally disordered crystals (α′-phase) of poly(l-lactic acid). Macromolecular Chemistry and Physics 215(11), 1134–1139, 2014. DOI: 10.1002/macp.201400126.

[161] Zhang, J.; Tashiro, K.; Tsuji, H.; Domb, A.J.: Disorder-to-order phase transition and multiple melting behavior of poly(l-lactide) investigated by simultaneous measurements of WAXD and DSC. Macromolecules 41(4), 1352–1357, 2008. DOI: 10.1021/ma0706071.

[162] Saeidlou, S.; Huneault, M.A.; Li, H.; Park, C.B.: Poly(lactic acid) crystallization. Progress in Polymer Science 37(12), 1657–1677, 2012. DOI: 10.1016/j.progpolymsci.2012.07.005.

[163] Eling, B.; Gogolewski, S.; Pennings, A.J.: Biodegradable materials of poly(l-lactic acid): 1. Melt-spun and solution-spun fibres. Polymer 23(11), 1587–1593, 1982. DOI: 10.1016/0032-3861(82)90176-8.

[164] Cartier, L.; Okihara, T.; Ikada, Y.; Tsuji, H.; Puiggali, J.; Lotz, B.: Epitaxial crystallization and crystalline polymorphism of polylactides. Polymer 41(25), 8909–8919, 2000. DOI: 10.1016/S0032-3861(00)00234-2.

[165] Lin, Y.; Zhang, K.-Y.; Dong, Z.-M.; Dong, L.-S.; Li, Y.-S.: Study of hydrogen-bonded blend of polylactide with biodegradable hyperbranched poly(ester amide). Macromolecules 40(17), 6257–6267, 2007. DOI: 10.1021/ma070989a.

[166] Wen, X.: One-pot route to graft long-chain polymer onto silica nanoparticles and its application for high-performance poly(l-lactide) nanocomposites. RSC Advances 9, 13908–13915, 2019. DOI: 10.1039/c9ra01360a.

[167] Avalos, F.; Lopez-Manchado, M.A.; Arroyo, M.: Crystallization kinetics of polypropylene: 1. Effect of small additions of low-density polyethylene. Polymer 37(25), 5681–5688, 1996. DOI: 10.1016/S0032-3861(96)00429-6.

[168] Shi, H.; Chen, X.; Chen, W.; et al.: Crystallization behavior, heat resistance, and mechanical performances of PLLA/myo-inositol blends. Journal of Applied Polymer Science 134(16), 44732, 2017. DOI: 10.1002/app.44732.

[169] Avrami, M.: Kinetics of phase change. I General theory. The Journal of Chemical Physics 7(12), 1103–1112, 1939. DOI: 10.1063/1.1750380.

[170] Avrami, M.: Kinetics of phase change. II Transformation-time relations for random distribution of nuclei. The Journal of Chemical Physics 8(2), 212–224, 1940. DOI: 10.1063/1.1750631.

[171] Avrami, M.: Granulation, phase change, and microstructure kinetics of phase change. III. The Journal of Chemical Physics 9(2), 177–184, 1941. DOI: 10.1063/1.1750872.

[172] Lorenzo, A.T.; Arnal, M.L.; Albuerne, J.; Müller, A.J.: DSC isothermal polymer crystallization kinetics measurements and the use of the Avrami equation to fit the data: Guidelines to avoid common problems. Polymer Testing 26(2), 222–231, 2007. DOI: 10.1016/j.polymertesting.2006.10.005.

[173] Zhou, W.Y.; Duan, B.; Wang, M.; Cheung, W.L.: Crystallization kinetics of poly(L-lactide)/carbonated hydroxyapatite nanocomposite microspheres. Journal of Applied Polymer Science 113(6), 4100–4115, 2009. DOI: 10.1002/app.30527.

[174] Suksut, B.; Saiprasit, P.; Schlarb, A.K.: Isothermal crystallization of polypropylene/titanium dioxide nanocomposites by flash scanning calorimetry. Asia-Pacific Journal of Science and Technology 26(1), 1–7, 2021. DOI: 10.14456/10.14456/apst.2021.7.

[175] Yang, J.; Wang, C.; Shao, K.; Ding, G.; Tao, Y.; Zhu, J.: Morphologies, mechanical properties and thermal stability of poly(lactic acid) toughened by precipitated barium sulfate. Russian Journal of Physical Chemistry A 89(11), 2092–2096, 2015. DOI: 10.1134/S0036024415110242.

[176] Guo, J.; Chen, X.; Wang, J.; He, Y.; Xie, H.; Zheng, Q.: The influence of compatibility on the structure and properties of PLA/Lignin biocomposites by chemical modification. Polymers 12(1), 56, 2020. DOI: 10.3390/polym12010056.

[177] Lin, L.: Processing Controlled Properties of Thermoplastic-Based Nanocomposites. Technische Universität Kaiserslautern, 2013.

[178] Wu, D.; Wu, L.; Wu, L.; Xu, B.; Zhang, Y.; Zhang, M.: Nonisothermal cold crystallization behavior and kinetics of polylactide/clay nanocomposites. Journal of Polymer Science Part B: Polymer Physics 45(9), 1100–1113, 2007. DOI: 10.1002/polb.21154.

[179] den Eynde, M.; Van Puyvelde, P.: 3D Printing of Poly(Lactic Acid). In Di Lorenzo, M.L.; Androsch, R. (eds): Industrial Applications of Poly(Lactic Acid), Springer International Publishing, Cham, 2018. DOI: 10.1007/12_2017_28.

[180] Liu, Z.; Wang, Y.; Wu, B.; Cui, C.; Guo, Y.; Yan, C.: A critical review of fused deposition modeling 3D printing technology in manufacturing polylactic acid parts. The International Journal of Advanced Manufacturing Technology 102, 2877–2889, 2019. DOI: 10.1007/s00170-019-03332-x.

List of Publications

Publication in Peer-Reviewed Journals:

1. Saiprasit, P.; Schlarb, A. K.: The effect of the compounding procedure on the morphology and mechanical properties of PLA/PBAT-based nanocomposites. International Polymer Processing, 36(2), 219–227, 2021.

2. Suksut, B.; Saiprasit, P.; Schlarb, A. K.: Isothermal crystallization of polypropylene/titanium dioxide nanocomposites by flash scanning calorimetry. Asia-Pacific Journal of Science and Technology, 26(1), 1–7, 2021.

3. Saiprasit, P.; Schlarb, A. K.: The effect of nanoparticle content and size on the morphology and crystallization behavior of poly(lactic acid)/silica nanoparticles. Journal of Plastics Technology, 15(5), 335–352, 2019.

Conference Distribution/Other Publications:

1. Saiprasit, P.; Schlarb, A. K.: Process–structure–property relationships of PLA/PBAT/silica nanocomposites with melt blending sequence. 7th International Conference on Bio-based Polymers, Bangkok, Thailand, 11–13 November 2019.

Directed Thesis

1. Khalilov, T.; Preißendörder, K.: The effect of residence time in different compounding sequences on the crystallization behavior and the mechanical properties of PLA/SiO$_2$ nanocomposites. Student project 2020.
2. Timasius, R.: Analysis of the morphology and crystallization behavior of injection-molded plates of poly(lactic acid)/silica nanocomposites. Bachelor thesis 2019.
3. Baumgarten, A. M.: Study on the crystallization behavior of poly(lactic acid)/ poly(butylene adipate-co-terephthalate)/silica nanocomposites with different blending procedures. Diploma thesis 2019.

Appendix

A Ingeo™ Biopolymer 3251D (Technical Data Sheet)

NatureWorks

Ingeo™ Biopolymer 3251D Technical Data Sheet

Injection Molding Process Guide

Ingeo biopolymer 3251D is designed for injection molding applications. This polymer grade has a higher melt flow capability than other Ingeo resin grades currently in the marketplace. The higher flow capability allows for easier molding of thin-walled parts. It is designed for injection molding applications, both clear and opaque, requiring high gloss, UV resistance and stiffness.

Processing Information

Ingeo biopolymer 3251D can be processed on conventional injection molding equipment. The material is stable in the molten state, provided that the drying procedures are followed. Mold flow is highly dependent on melt temperature. In order to control melt temperature, it is recommended to balance screw speed, back pressure, and process temperature. Injection speed should be medium to fast.

Process Details

Startup and Shutdown

Ingeo biopolymer 3251D is not compatible with a wide variety of other resins, and special purging sequences should be followed:

1. Clean extruder and bring temperatures to steady state with low viscosity, general purpose polystyrene or polypropylene.

2. Vacuum out hopper system to avoid contamination.

3. Introduce Ingeo biopolymer into the extruder at the operating conditions used in step one.

4. Once Ingeo biopolymer has purged, reduce barrel temperatures to desired set points.

5. At shutdown, purge machine with high viscosity polystyrene or polypropylene.

Typical Material & Application Properties		
Physical Properties	**Ingeo 3251D**	**ASTM Method**
Specific Gravity	1.24	D792
MFR, g/10 min (210°C, 2.16kg)	80	D1238
MFR, g/10 min (190°C, 2.16kg)	35	D1238
Relative Viscosity	2.5	
Crystalline Melt Temperature (°C)	155-170	D3418
Glass Transition Temperature (°C)	55-60	D3418
Clarity	Transparent	
Mechanical Properties		
Tensile Yield Strength, psi (MPa)	9,000 (62)	D638
Tensile Elongation, %	3.5	D638
Notched Izod Impact, ft-lb/in (J/m)	0.3 (16)	D256
Flexural Strength (MPa)	15,700 (108)	D790
Notched Izod Impact, ft-lb/in (J/m)	0.3 (16)	D256
Heat Distortion Temperate (°C)	55	E2092

Note: These are starting points and may need to be optimized.

Processing Temperature Profile		
Melt Temp.	370-410°F	188-210°C
Feed Throat	70°F	20°C
Feed Temp.	330-350°F	166-177°C
Compression Section	360-380°F	182-193°C
Metering Section	370-400°F	188-205°C
Nozzle	370-400°F	188-205°C
Mold	75°F	25°C
Screw Speed	100-200 rpm	
Back Pressure	50-100 psi	
Mold Shrinkage	.004 in/in. +/-.001	

Ingeo Biopolymer 3251D Technical Data Sheet

Drying

Inline drying is recommended for Ingeo biopolymers. A moisture content of less than 0.010% (100 ppm) is recommended to prevent viscosity degradation. Polymer is supplied in foil-lined boxes or bags dried to<250 ppm. The resin should not be exposed to atmospheric conditions after drying. Keep the package sealed until ready to use and promptly dry and reseal any unused material. The drying curves for both amorphous and crystalline resins are shown to the right.

Note: Amorphous polymer must be dried below 120F (50C).

Drying Curve for Equilibrium Moisture Level Polylactide Pellets, Dryer set up: 0.25 cfm/lb pellets; Dewpoint = -40°C

- 210°F (100°C), Crystalline PLA
- 175°F (80°C), Crystalline PLA
- 140°F (60°C), Crystalline PLA
- 120°F (50°C), Amorphous PLA
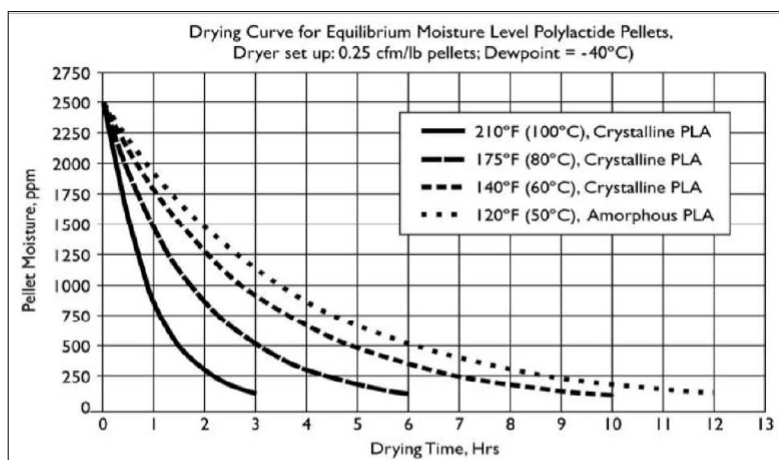
Food Packaging Status

U.S. Status

On January 3, 2002 FCN 000178 submitted by NatureWorks LLC to FDA became effective. This effective notification is part of list currently maintained on FDA's website at

http://www.fda.gov/food/ingredientspackaginglabeling/packagingfcs/notifications/default.htm

This grade of Ingeo biopolymer may therefore be used in food packaging materials and, as such, is a permitted component of such materials pursuant to section 201(s) of the Federal, Drug, and Cosmetic Act, and Parts 182, 184, and 186 of the Food Additive Regulations. All additives and adjuncts contained in the referenced Ingeo biopolymer formulation meet the applicable sections of the Federal Food, Drug, and Cosmetic Act. The finished polymer is approved for all food types and B-H use conditions. We urge all of our customers to perform GMP (Good Manufacturing Procedures) when constructing a package so that it is suitable for the end use.

European Status

This grade of Ingeo biopolymer complies with Plastics Regulation 10/2011 as amended. No SML's for the above referenced grade exist in Plastics Regulation 10/2011 as amended. NatureWorks LLC would like to draw your attention to the fact that the EU- Plastics Regulation 10/2011, which applies to all EU-Member States, includes a limit of 10 mg/dm^2 of the overall migration from finished plastic articles into food. In accordance with Plastics Regulation 10/2011 the migration should be measured on finished articles placed into contact with the foodstuff or appropriate food simulants for a period and at a temperature which are chosen by reference to the contact conditions in actual use, according to the rules laid down in Plastics Regulation 10/2011.

Please note that it is the responsibility of both the manufacturers of finished food contact articles as well as the industrial food packers to make sure that these articles in their actual use are in compliance with the imposed specific and overall migration requirements.

This grade as supplied meets European Parliament and Council Directive 94/62/EC of 20 December 1994 on packaging and packaging waste heavy metal content as described in Article 11.

Should you need further clarification, contact NatureWorks LLC.

Bulk Storage Recommendations

The resin silos recommended and used by NatureWorks LLC are designed to maintain dry air in the silo and to be isolated from the outside air. This design would be in contrast to an open, vented to atmosphere system that we understand to be a typical polystyrene resin silo. Key features that are added to a typical (example: polystyrene) resin silo to achieve this objective include a cyclone and rotary valve loading system and some pressure vessel relief valves. The dry air put to the system is sized to the resin flow rate out of the silo. Not too much dry air would be needed and there may be excess instrument air (-30°F dew point) available in the plant to meet the needs for dry air. Our estimate is 10 scfm for a 20,000 lb/hr rate resin usage. Typically, resin manufacturers specify aluminum or stainless steel silos for their own use and avoid epoxy-lined steel.

Ingeo Biopolymer 3251D Technical Data Sheet

Safety and Handling Considerations

Safety Data Sheets (SDS) for Ingeo biopolymers are available from NatureWorks. SDS's are provided to help customers satisfy their own handling, safety, and disposal needs, and those that may be required by locally applicable health and safety regulations. SDS's are updated regularly; therefore, please request and review the most current SDS's before handling or using any product.

The following comments apply only to Ingeo biopolymers; additives and processing aids used in fabrication and other materials used in finishing steps have their own safe-use profile and must be investigated separately.

Hazards and Handling Precautions

Ingeo biopolymers have a very low degree of toxicity and, under normal conditions of use, should pose no unusual problems from incidental ingestion or eye and skin contact. However, caution is advised when handling, storing, using, or disposing of these resins, and good housekeeping and controlling of dusts are necessary for safe handling of product. Pellets or beads may present a slipping hazard.

No other precautions other than clean, body-covering clothing should be needed for handling Ingeo biopolymers. Use gloves with insulation for thermal protection when exposure to the melt is localized. Workers should be protected from the possibility of contact with molten resin during fabrication.

Handling and fabrication of resins can result in the generation of vapors and dusts that may cause irritation to eyes and the upper respiratory tract. In dusty atmospheres, use an approved dust respirator.

Good general ventilation of the polymer processing area is recommended. At temperatures exceeding the polymer melt temperature (typically 175ºC), polymer can release fumes, which may contain fragments of the polymer, creating a potential to irritate eyes and mucous membranes. Good general ventilation should be sufficient for most conditions. Local exhaust ventilation is recommended for melt operations. Use safety glasses (or goggles) to prevent exposure to particles, which could cause mechanical injury to the eye. If vapor exposure causes eye discomfort, improve localized fume exhausting methods or use a full-face respirator.

The primary thermal decomposition product of PLA is acetaldehyde, a material also produced during the thermal degradation of PET. Thermal decomposition products also include carbon monoxide and hexanal, all of which exist as gases at normal room conditions. These species are highly flammable, easily ignited by spark or flame, and can also auto ignite. For polyesters such as PLA, thermal decomposition producing flammable vapors containing acetaldehyde and carbon monoxide can occur in almost any process equipment maintaining PLA at high temperature over longer residence times than typically experienced in extruders, fiber spinning lines, injection molding machines, accumulators, pipe lines and adapters. As a rough guideline based upon some practical experience, significant decomposition of PLA will occur if polymer residues are held at temperatures above the melting point for prolonged periods, e.g., in excess of 24 hours at 175°C, although this will vary significantly with temperature.

Combustibility

Ingeo biopolymers will burn. Clear to white smoke is produced when product burns. Toxic fumes are released under conditions of incomplete combustion. Do not permit dust to accumulate. Dust layers can be ignited by spontaneous combustion or other ignition sources. When suspended in air, dust can pose an explosion hazard. Firefighters should wear positive-pressure, self-contained breathing apparatuses and full protective equipment. Water or water fog is the preferred extinguishing medium. Foam, alcohol-resistant foam, carbon dioxide or dry chemicals may also be used. Soak thoroughly with water to cool and prevent re-ignition.

Disposal

DO NOT DUMP INTO ANY SEWERS, ON THE GROUND, OR INTO ANY BODY OF WATER. For unused or uncontaminated material, the preferred option is to recycle into the process otherwise, send to an incinerator or other thermal destruction device. For used or contaminated material, the disposal options remain the same, although additional evaluation is required. Disposal must be in compliance with Federal, State/Provincial, and local laws and regulations.

Environmental Concerns

Generally speaking, lost pellets, while undesirable, are benign in terms of their physical environmental impact, but if ingested by wildlife, they may mechanically cause adverse effects. Spills should be minimized, and they should be cleaned up when they happen. Plastics should not be discarded into the environment.

Product Stewardship

NatureWorks has a fundamental duty to all those that use our products, and for the environment in which we live. This duty is the basis for our Product Stewardship philosophy, by which we assess the health and environmental information on our products and their intended use, and then take

Ingeo Biopolymer 3251D Technical Data Sheet

appropriate steps to protect the environment and the health of our employees and the public.

Customer Notice

NatureWorks encourages its customers and potential users of its products to review their applications from the standpoint of human health and environmental quality. To help ensure our products are not used in ways for which they were not intended or tested, our personnel will assist customers in dealing with ecological and product safety considerations. Your sales representative can arrange the proper contacts. NatureWorks literature should be consulted prior to the use of the company's products.

NOTICE:
No freedom from infringement of any patent owned by NatureWorks LLC or others is to be inferred. No information in this publication can be considered a suggestion to infringe patents.

The technical information, recommendations and other statements contained in this document are based upon tests or experience that NatureWorks believes are reliable, but the accuracy or completeness of such information is not guaranteed. Many factors beyond NatureWorks control can affect the use and performance of a NatureWorks product in a particular application, including the conditions under which the product is used and the time and environmental conditions in which the product is expected to perform. Since these factors are uniquely within the user's knowledge or control, it is essential that the user evaluate the NatureWorks product to determine whether it is fit for a particular purpose and suitable for the user's method of application. In addition, because use conditions are outside of NatureWorks control and applicable laws may differ from one location to another and may change with time, Customer is solely responsible for determining whether products and the information in this document are appropriate for Customer's use and for ensuring that Customer's workplace, use and disposal practices are in compliance with applicable laws and regulations. NatureWorks LLC assumes no obligation or liability for the information in this document.

NATUREWORKS MAKES NO WARRANTY, EXPRESS OR IMPLIED, REGARDING THE INFORMATION CONTAINED HEREIN OR ITS PRODUCTS, INCLUDING BUT NOT LIMITED TO ANY WARRANTY AS TO ACCURACY OR COMPLETENESS OF INFORMATION, OR ANY IMPLIED WARRANTY OF MERCHANTABILITY OR FITNESS FOR A PARTICULAR PURPOSE.

NOTICE REGARDING PROHIBITED USE RESTRICTIONS: Unless specifically agreed to in writing by NatureWorks, NatureWorks LLC will not knowingly sell or sample any product into any of the following commercial or developmental applications (i) components of or packaging for tobacco products, (ii) components of products intended for human or animal consumption, (iii) any application that is intended for any internal contact with human body fluids or body tissues, (iv) as a critical component in any medical device that supports or sustains human life, (v) in any product that is designed specifically for ingestion or internal use by pregnant women, (vi) in any application designed specifically to promote or interfere with human reproduction, (vii) in microbeads, including those used in personal care/cosmetic applications, or (vii) to manufacture bottles or bottle pre-forms in North America.

For additional information please contact NatureWorks via our website on the tab called FAQ's or by clicking here.

🌿 NatureWorks
15305 Minnetonka Blvd., Minnetonka, MN 55345

B ecoflex® F Blend C1200 (Product Information)

Biodegradable Polymers

Product Information

Version 1.0
January 2013
G-PMS/B

ecoflex® F Blend C1200

Biodegradable polyester for compostable film

® = ecoflex is a registered trademarks of BASF SE;
Lupolen is a registered trademark of
Lyondell Basell group companies

Product description

ecoflex® F Blend C1200 is our biodegradable, statistical, aliphatic-aromatic copolyester based on the monomers 1.4-butanediol, adipic acid and terephthalic acid in the polymer chain. ecoflex® F Blend C1200 will biodegrade to the basic monomers 1.4-butanediol, adipic acid and terephthalic acid and eventually to carbon dioxide, water and biomass when metabolized in the soil or compost under standard conditions.

ecoflex® F Blend C1200 has properties similar to PE-LD because of its high molecular weight and its long chain branched molecular structure.

BASF
The Chemical Company

- Transparent to translucent, semi-crystalline structure with DSC melting point in the range of PE-LD: 110-120°C
- High ultimate elongation at break and high failure energy (dart drop)
- High, but controllable water vapour transmission rate (WVTR)
- MVR (190°C, 2.16 kg): 2.5-4.5 ml/10 min
- Good thermostability up to 230°C
- regular predrying of pellets
- Good processability on blown film lines
- Down gaging to 10 µm possible
- Weldable and printable

ecoflex® F Blend C1200 fulfils the requirements of the European standard DIN EN 13432, the US standard ASTM D 6400 and the Japanese GreenPla standard for compostable and biodegradable polymers, because it can be degraded by micro-organisms. The biodegradation process in soil depends on the specific environment (climate, soil quality, population of micro-organisms).

ecoflex® F Blend C1200 is one of the few biodegradable plastics, which complies in its composition with the European and American food stuff legislation for food contact: EU Directive 2002/72/EC (as amended) and US food contact notification FCN 907. Specific limitations and more details are given on request. The converter or packer has to check the suitability of the article for the application.

Form supplied and storage

ecoflex® F Blend C1200 is supplied as lens shaped pellets in 1 t big bags or bulk containers. Temperatures during transportation and storage may not exceed 70°C at any time. Storage time of unopened bags may not surpass 12 month at room temperature (23°C).

Quality Control

ecoflex® F Blend C1200 is produced as a standard material in a continuous production process according to DIN EN ISO 9001:2000. The melt volume rate, MVR, at 190°C, 2.16 kg, according to ISO 1133 has been defined as specified parameter for quality control. A certificate can be provided with each lot number (10 t) upon request. In order to obtain a high accuracy for the MVR measurement the granules should be dried for 30 minutes at 70°C using e.g. an electronic moisture analyser (e.g. Brabender Aquatrac plus). Other data given in our literature are typical values, which are not part of our product specification for ecoflex® F Blend C1200.

Applications

ecoflex® F Blend C1200 has been developed for the conversion to flexible films using a blown film or cast film process. Typical applications are packaging films, agricultural films and compost bags. In view of numerous factors influencing functionality and shelf life of ecoflex® films and finished articles made thereof these parameters have to be tested by the converters before utilisation.

We supply technical service information concerning the blown or cast film process with ecoflex® F Blend C1200 on demand.

Product Information ecoflex® F Blend C 1200

Intellectual Property

It is the responsibility of those to whom we supply our products to en-sure that any proprietary rights and existing laws and legislation are ob-served. Some uses of ecoflex® and product obtained by use of ecoflex® are subject of intellectual property rights. Purchase of ecoflex® does not entitle the buyer or any third to produce, offer or use any blends of ecoflex® protected under property rights and all their equivalents as listed here:

- EP-B 1656423
- EP-B 937120
- EP-B 950689
- EP-B 1838784
- EP-B 947559
- EP-B 965615

Typical basic material properties of ecoflex® F Blend C1200

Property	Unit	Test Method	ecoflex® F Blend C1200	Lupolen® 2420 F
Mass density	g/cm³	ISO 1183	1.25 - 1.27	0.924
Melt flow rate MFR 190°C, 2.16 kg	g/10 min	ISO 1133	2.7 - 4.9	0.6 - 0.9
Melt volume rate MVR 190°C, 2.16 kg	ml/10 min	ISO 1133	2.5 - 4.5	0.8 - 1.2
Melting point	°C	DSC	110 - 120	111
Shore D hardness	–	ISO 868	32	48
Vicat VST A/50	°C	ISO 306	91	96

Typical properties of ecoflex® F Blend C1200 blown film, 50 µm

Property	Unit	Test Method	ecoflex® F Blend C1200	Lupolen® 2420 F
Transparency	%	ASTM D 1003	82	89
Tensile strength	N/mm²	ISO 527	35/44	26/20
Ultimate strength	N/mm²	ISO 527	36/45	–
Ultimate Elongation	%	ISO 527	560/710	300/600
Failure Energy (Dyna Test)	J/mm	ISO 53373	24	5.5
Permeation rates:				
Oxygen (23°C, dry)	cm³/(m²·d·bar)	ASTM D 3985	1200	2900
Water vapour (23°C, 85% r.h.)	[g/(m²·d)]	ASTM F-1249	135	1.7

Note

The information submitted in this document is based on our current knowledge and experience. In view of the many factors that may affect processing and application, these data do not relieve processors of the responsibility of carrying out their own tests and experiments; neither do they imply any legally binding assurance for a special purpose. It is the responsibility of those to whom we supply our products to ensure that any proprietary rights and existing laws and legislation are observed.

C   AEROSIL® R 8200 (Product Information)

AEROSIL®

Product information

AEROSIL® R 8200

Hydrophobic fumed silica

Characteristic physico-chemical data

Properties and test methods	Unit	Value
Specific surface area (BET)	m^2/g	135 - 185
pH value in 4% dispersion		≥ 5.0
Loss on drying* 2 hours at 105 °C	%	≤ 0.5
C content	%	2.0 - 4.0
Tamped density* ISO 787-11, modified	g/l	approx. 140
SiO_2 content based on ignited material	%	≥ 99.8

* ex plant
The data represents typical values (no product specification).

Registrations (substance or product components)

AEROSIL® R 8200

CAS-No.	68909-20-6
REACH (Europe)	exempted
TSCA (USA)	registered
DSL (Canada)	registered
AICS (Australia)	registered
ENCS (Japan)	registered
KECI (Korea)	registered
IECS (China)	registered
PICCS (Philippines)	registered

AEROSIL® R 8200 is a structure modified with hexamethyldisilazane aftertreated fumed silica.

Applications and properties

Applications

- Silicone rubber
- Adhesives and Sealants
- Defoamers
- Toner

Properties

- Low thickening effect and excellent processability enable high loading levels of polymer systems
- Excellent reinforcing properties in silicone rubber applications at high filler loading levels (e.g. self-levelling RTV-1, RTV-2, LSR)
- Well suited for transparent systems
- Free-flow aid for powders

Safety and handling

Information concerning the safety of this product is listed in the corresponding Safety Data Sheet, which will be sent with the first delivery or upon updating. Such information is also available from Evonik Resource Efficiency GmbH, Product Safety Department, E-MAIL sds-hu@evonik.com or can be downloaded from our homepage www.aerosil.com. We recommend to read carefully the safety data sheet prior to the use of our product.

Packaging and storage

AEROSIL® R 8200 is supplied in multiple layer 15 kg bags. We recommend to store the product in closed containers under dry conditions and to protect the material from volatile substances. AEROSIL® R 8200 should be used within 2 years after production.

Customer Service

Europe/ Middle-East/ Africa/ Latin America
Evonik Resource Efficiency GmbH
Business Line Silica
PB 010-A410
Rodenbacher Chaussee 4
63457 Hanau-Wolfgang
Germany
PHONE +49 6181 59 12532
FAX +49 6181 59 712532
aerosil@evonik.com
www.aerosil.com

North America
Evonik Corporation
Business Line Silica
299 Jefferson Road
Parsippany, NJ 07054-0677
USA
PHONE +1 800-233-8052
FAX +1 973-929-8502
aerosil@evonik.com
www.aerosil.com

Asia (excluding Japan)
Evonik (SEA) Pte. Ltd.
Business Line Silica
3 International Business Park
Nordic European Centre, #07-18
Singapore 609927
PHONE +65 6809-6877
FAX +65 6809-6677
aerosil@evonik.com
www.aerosil.com

Japan
NIPPON AEROSIL CO., LTD.
Marketing & Sales Division
P.O. Box 7015
Shinjuku Monolith 13F
3-1, Nishi-Shinjuku 2-chrome
Shinjuku-ku, Tokyo
163-0913 Japan
PHONE +81 3 3342-1789
FAX +81 3 3342-1761
infonac@evonik.com
www.aerosil.jp

Technical Service

Europe/ Middle-East/ Africa/ Latin America
Evonik Resource Efficiency GmbH
Business Line Silica
HPC 911-221 A
Rodenbacher Chaussee 4
63403 Hanau-Wolfgang
Germany
PHONE +49 6181 59-3936
FAX +49 6181 59 4489
technical.service.aerosil@evonik.com
www.aerosil.com

North America
Evonik Corporation
Business Line Silica
2 Turner Place
Piscataway, NJ 08855-0365
USA
PHONE +1 888 SILICAS
PHONE +1 732 981-5000
FAX +1 732 981-5275
technical.service.aerosil@evonik.com
www.aerosil.com

Asia (excluding Japan)
Evonik Specialty Chemicals (Shanghai) Co.,Ltd
Business Line Silica
55 Chundong Road
Xinzhuang Industry Park
Shanghai 201108
P.R. China
PHONE +86 21 6119-1065
FAX +86 21 6119-1075
technical.service.aerosil@evonik.com
www.aerosil.com

Japan
NIPPON AEROSIL CO., LTD.
Applied Technology Group
3 Mita-Cho
Yokkaichi, Mie
510-0841 Japan
PHONE +81 59 345-5270
FAX +81 59 346-4657
infonac@evonik.com
www.aerosil.jp

Evonik.Power to create.

EVONIK
INDUSTRIES

D   Design of Screw Extruder (Data Sheet)

GFA-2-20-30	
GFA-2-20-30	Zyl-0/MC
GFA-2-30-30	
GFA-2-30-30	Zyl-1/MC Vakuum
GFA-2-30-30	
KB 4-2-15-90°	
KB 4-2-15-90°	
KB 4-2-15-90°	Zyl-0/MC
LEX Leihgabe KB 4-2-15-60°-Re	
GFA-2-20-30	
KB 4-2-15-90°	
KB 4-2-15-60°-Re	Zyl-1/MC Verschlossen
KB 4-2-15-60°-Re	
GFA-2-20-15	
GFA-2-30-30	
GFA-2-30-30	Zyl-1/MC Verschlossen
	opt. Atm. Entl.
KB 4-2-15-30°-Li	
KB 4-2-15-30°-Re	
GFA-2-20-15	
KB 4-2-15-60°-Re	Zyl-0/MC
KB 4-2-15-30°-Re	
KB 4-2-15-30°-Re	
GFA-2-30-30	
GFA-2-30-30	Zyl-S/MC (LSB 17) Füllstoff
LEX Leihgabe KB 4-2-15-90°	
KB 4-2-15-90°	
KB 4-2-15-60°-Re	
GFA-2-20-15	Zyl-0/MC
KB 4-2-15-90°	
KB 4-2-15-60°-Re	
KB 4-2-15-30°-Re	
GFA-2-30-15	
GFA-2-30-30	Zyl-B/MC Verschlossen
GFF-2-30-30-M	Wärmesperre
GFF-2-30-30-A	Zyl-E Polymer / Additive
GFF-2-20-30-A	

Figure 4.39:   Design of screw extruder (ZSE18MAXX40D).

Table 4.7:   Information of the screw design

Importiert von ZSE 18 MAXX – SIGMA ME.mas	
Maschinenbezeichnung	ZSE 18 MX
Drehrichtung	Links
Nenndurchmesser	19 mm
Achsabstand	15 mm
Rastermaß	19 mm
max. Antriebsleistung	10 kW
...bei Drehzahl	1200 1/min
Dornlängen [mm]	
Kommentar	
Available machine configurations on request	
Maschinenbaukasten	
Zylinderelemente	
Elementtyp 'Zylinder-Adapter':	
Wärmesperre	(1 / -)
Elementtyp 'Zylinder-0':	
Zyl-0/MC	(4 / -)
Elementtyp 'Zylinder-1/1G':	
Zyl-1/MC	(3 / -)
Elementtyp 'Zylinder-E/EG/B/S':	
Zyl-B/MC	(1 / -)
Zyl-E	(1 / -)
Zyl-S/MC (LSB 17)	(1 / -)
Scheibenelemente	
Elementtyp 'MB':	
MB-3-5-90-30	(- / -)
MB-3-5-90-30-L	(- / -)

Maschinenbaukasten

Gewindeelemente

Elementtyp 'GFA':

GFA-2-20-15	(3 / -)
GFA-2-20-15-L	(- / -)
GFA-2-20-30	(3 / -)
GFA-2-20-30-A	(1 / -)
GFA-2-30-15	(1 / -)
GFA-2-30-30	(8 / -)

Elementtyp 'GFF':

GFF-2-30-30-A	(1 / -)
GFF-2-30-30-E	(- / -)
GFF-2-30-30-M	(1 / -)

Elementtyp 'GFM & SME':

GFM-2-20-30	(- / -)
GFM-2-20-30-L	(- / -)
SME-2-20-30	(- / -)
SME-2-20-30-L	(- / -)

Gewindeelemente

Elementtyp 'KB':

KB 4-2-15-30°-Li	(1 / -)
KB 4-2-15-30°-Re	(4 / -)
KB 4-2-15-60°-Re	(6 / -)
KB 4-2-15-90°	7 / -)

E   Schwartz-Saltykov Correction

Figure 4.40 shows the relationship between limiting section diameters on a single sphere, which shows related parameters using for the correcting equation. Based on equations (3.4) and (3.5), the number average diameter (D_n) and volume average diameter (D_v) can be corrected via Schwartz-Saltykov method, as described in the following equations [114]:

$$D_n = \frac{\sum_i (N_V)_j D_{i,PB}}{\sum_i (N_V)_j} \tag{4.14}$$

$$D_v = \frac{\sum_i (N_V)_j D_{i,PB}^4}{\sum_i (N_V)_j \, D_{i,PB}^3} \tag{4.15}$$

where N_V is the number of particles per unit volume, which is given as:

$$N_V(j) = \frac{\alpha(i)N_A(i) - \alpha(i+1)N_A(i+1) - \alpha(i+2)N_A(i+2) - \cdots - \alpha(k)N_A(k)}{\Delta} \tag{4.16}$$

where N_A is the number of sections per unit area and Δ defines as the ratio of the maximum diameter D_{max} to the number of groups k ($\Delta = D_{max}/k$). k value is recommended between 7 to 15. The definition of terms used in correction is shown in Table 4.8. α is the coefficient value, which is given by Table 4.9.
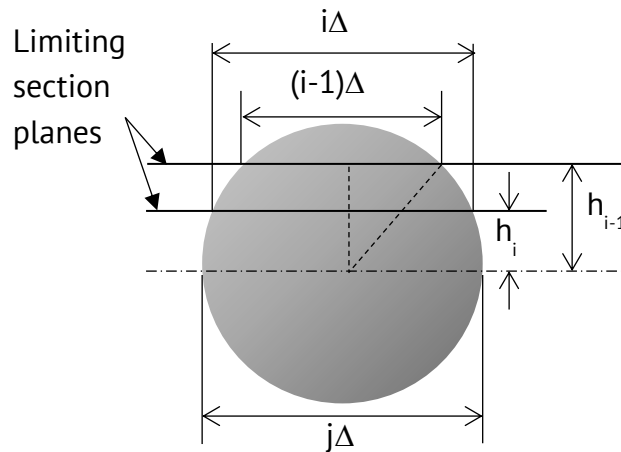
Figure 4.40:   Relationship between limiting section diameters on a single sphere [adapted from [114]].

Table 4.8:   Definition of terms used in Schwartz-Saltykov method [114]

Number of the group	Diameter	Number per unit volume
Particles (j)		
1	Δ	$N_V(1)$
2	2Δ	$N_V(2)$
3	3Δ	$N_V(3)$
j	$j\Delta$	$N_V(j)$
k	$k\Delta$	$N_V(k)$

Number of the group	Diameter	Number per unit area
Section (i)		
1	0 to Δ	$N_A(1)$
2	Δ to 2Δ	$N_A(2)$
3	2Δ to 3Δ	$N_A(3)$
i	$(i-1)\Delta$ to $i\Delta$	$N_A(i)$
k	$(k-1)\Delta$ to $k\Delta$	$N_A(k)$

Table 4.9:   Saltykov's table of coefficients for calculating particle distributions from diameters [114]

Coefficients, $\alpha[i,j]$

	N$_A$(1)	N$_A$(2)	N$_A$(3)	N$_A$(4)	N$_A$(5)	N$_A$(6)	N$_A$(7)	N$_A$(8)	N$_A$(9)	N$_A$(10)	N$_A$(11)	N$_A$(12)	N$_A$(13)	N$_A$(14)	N$_A$(15)
N$_V$(1)	+1.0000	0.1547	0.0360	0.0130	0.0061	0.0033	0.0020	0.0013	0.0009	0.0006	0.0005	0.0004	0.0003	0.0002	0.0001
N$_V$(2)		+0.5774	0.1529	0.0420	0.0171	0.0087	0.0051	0.0031	0.0021	0.0015	0.0010	0.0009	0.0006	0.0006	0.0004
N$_V$(3)			+0.4472	0.1382	0.0408	0.0178	0.0093	0.0057	0.0037	0.0026	0.0018	0.0013	0.0010	0.0007	0.0007
N$_V$(4)				+0.3779	0.1260	0.0386	0.0174	0.0095	0.0058	0.0038	0.0027	0.0020	0.0016	0.0012	0.0009
N$_V$(5)					+0.3333	0.1161	0.0366	0.0168	0.0094	0.0059	0.0040	0.0028	0.0021	0.0016	0.0013
N$_V$(6)						+0.3015	0.1081	0.0346	0.0163	0.0091	0.0058	0.0041	0.0028	0.0022	0.0016
N$_V$(7)							+0.2773	0.1016	0.0329	0.0155	0.0090	0.0057	0.0040	0.0029	0.0022
N$_V$(8)								+0.2582	0.0961	0.0319	0.0151	0.0088	0.0056	0.0039	0.0028
N$_V$(9)									+0.2425	0.0913	0.0301	0.0146	0.0085	0.0055	0.0039
N$_V$(10)										+0.2294	0.0872	0.0290	0.0140	0.0083	0.0054
N$_V$(11)											+0.2182	0.0836	0.0280	0.0136	0.0080
N$_V$(12)												+0.2085	0.0804	0.0270	0.0132
N$_V$(13)													+0.2000	0.0776	0.0261
N$_V$(14)														+0.1925	0.0750
N$_V$(15)															+0.185
N$_V$	1.0000	0.4227	0.2583	0.1847	0.1433	0.1170	0.0988	0.0856	0.0753	0.0672	0.0610	0.0553	0.0511	0.0472	0.0441

F　　　Residence Time in the Twin-Screw Extruder

The residence time in the twin-screw extruder is measured as a function of feeding rate or throughput, while the screw speed is fixed during compounding (see Figure 4.41). PLA polymer (~0.5g) with a red pigment is dropped in the screw at the feeding zone, afterward the residence time, in which red PLA was spending in the extruder, were measured.
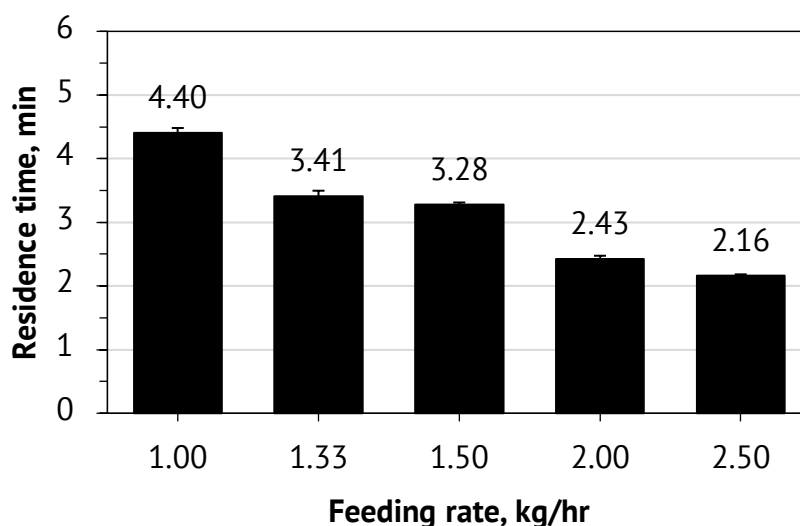
Figure 4.41:　Residence time as a function of feeding rate in the twin-screw extruder used in this work.

G　　　Degree of Crystallinity

Table 4.10:　Degree of crystallinity in the PLA phase ($X_{c,PL}$) of all studied materials

Material	$X_{c,PL}$, %
PLA	7.4 ± 1.7
PLA-S1	31.9 ± 1.2
PLA/PBAT-S0	13.4 ± 1.9
PLA/PBAT-S1-P1	42.4 ± 0.6
PLA/PBAT-S1-P2	51.6 ± 0.4
PLA/PBAT-S1-P3	21.8 ± 0.3
PLA/PBAT-S1-P4	10.9 ± 0.1

H   Isothermal Crystallization Thermograms

Figure 4.42:   Isothermal crystallization thermograms of neat PLA (PL), PLA-S1 (PL1), PLA/PBAT blend (S0), and PLA/PBAT-based nanocomposites (S1-P1, S1-P3, S1-P4) at different crystallization temperatures.

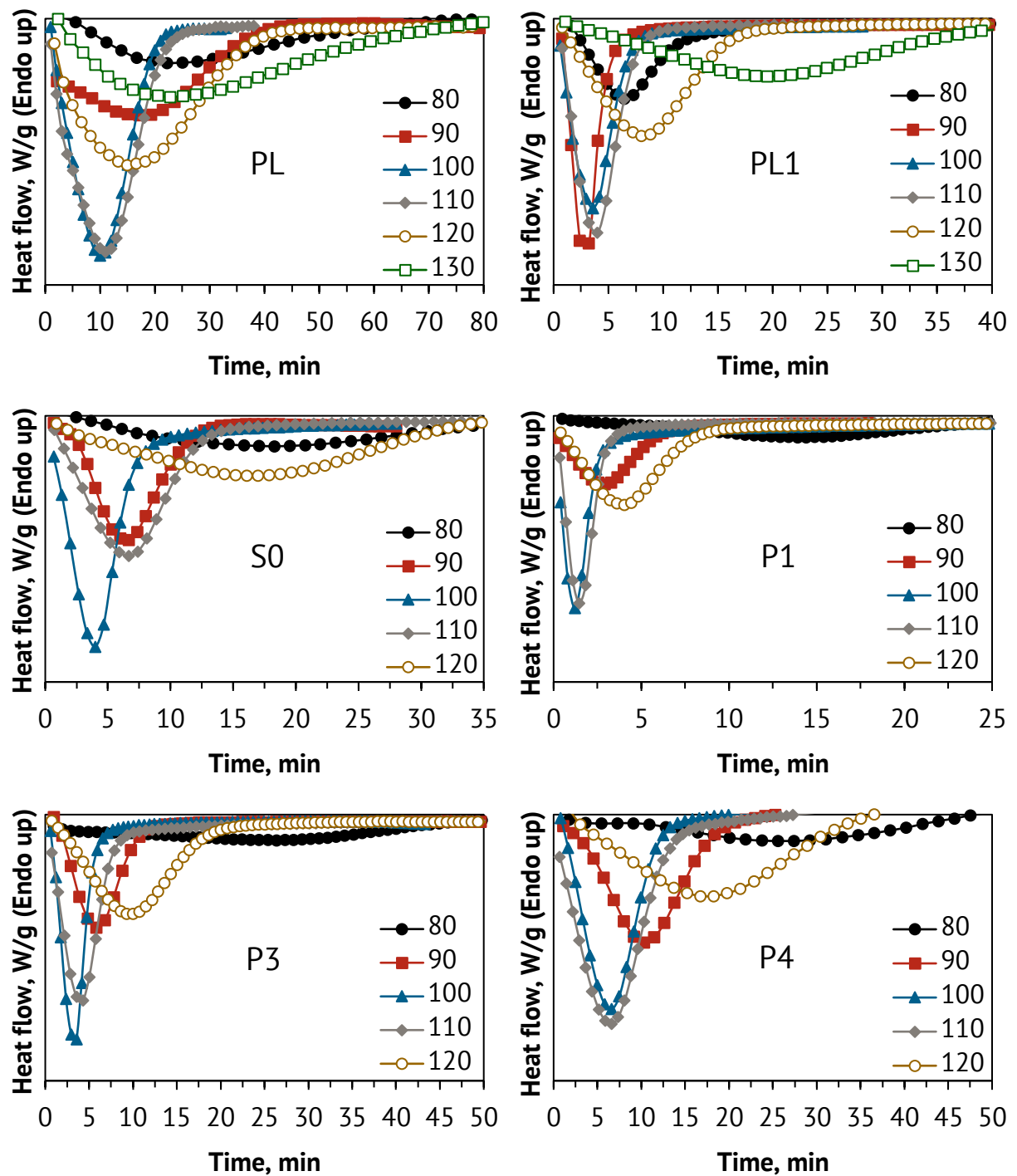Figure 4.43: Relative crystallinity (X_t) as a function of crystallization time: neat PLA (PL), PLA-S1 (PL1), PLA/PBAT blend (S0), and PLA/PBAT-based nanocomposites (S1-P1, S1-P3, S1-P4) at different crystallization temperatures.
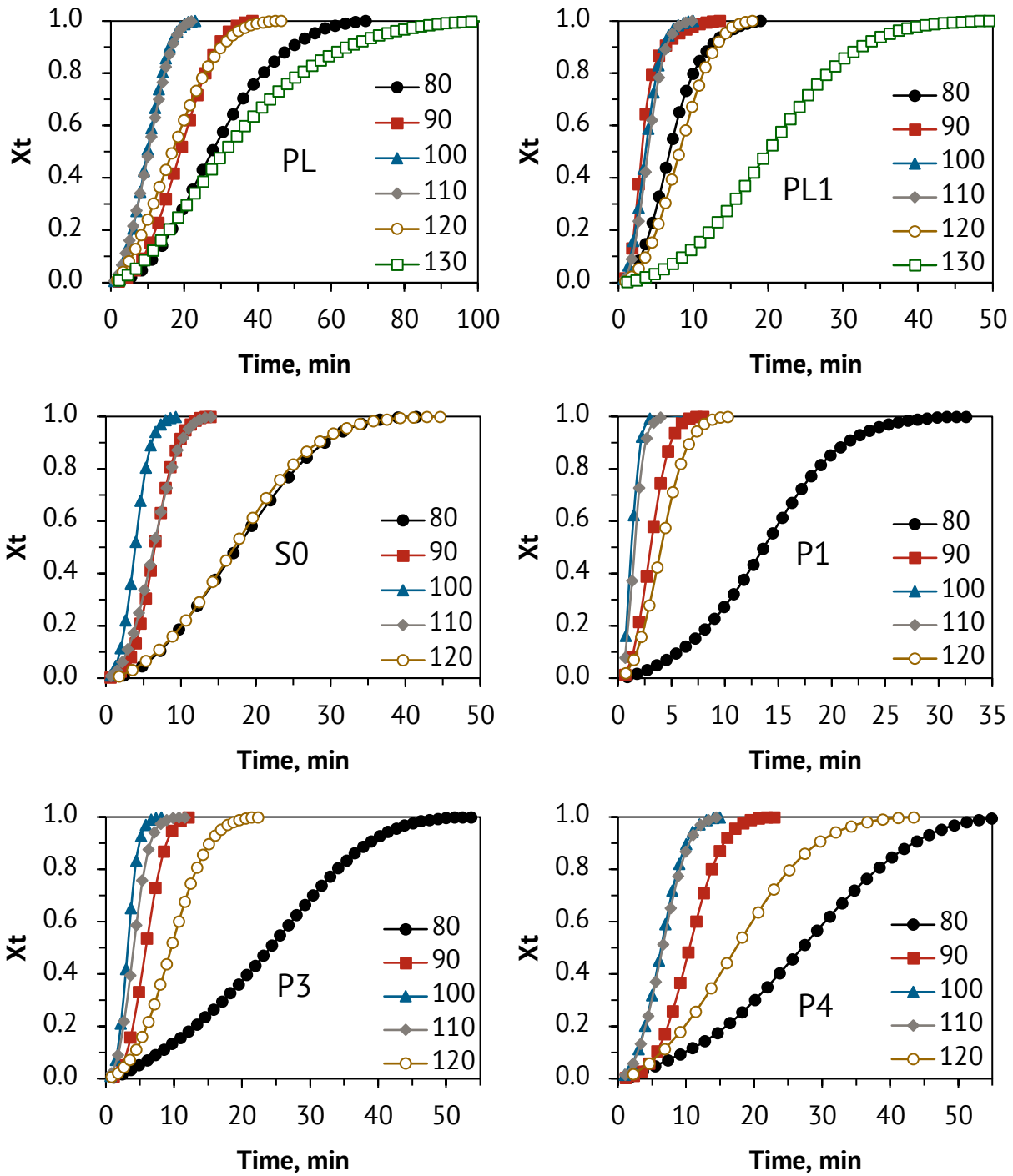
I Tensile Properties

Table 4.11:   Young's modulus, tensile strength and elongation at break of all studied materials

Material	Young's modulus, MPa	Tensile strength, MPa	Elongation at break, %
	Injection direction (MD)		
PLA	3680 ± 200	73.6 ± 0.8	4.8 ± 1.1
PLA-S1	3610 ± 134	68.9 ± 0.9	4.2 ± 0.8
PLA/PBAT-S0	2230 ± 41	43.5 ± 0.7	28.8 ± 2.8
PLA/PBAT-S1-P1	2400 ± 197	40.4 ± 0.3	14.3 ± 3.6
PLA/PBAT-S1-P2	2880 ± 319	48.2 ± 0.3	18.1 ± 4.0
PLA/PBAT-S1-P3	2970 ± 352	48.7 ± 0.5	21.6 ± 4.4
PLA/PBAT-S1-P4	2680 ± 323	46.3 ± 0.4	20.3 ± 2.8
PLA/PBAT-S4-P1	3040 ± 292	42.4 ± 0.3	7.4 ± 1.0
PLA/PBAT-S4-P2	2830 ± 86	48.4 ± 0.4	9.8 ± 1.9
PLA/PBAT-S4-P3	2750 ± 246	45.8 ± 0.9	16.9 ± 2.7
PLA/PBAT-S4-P4	2550 ± 48	46.1 ± 0.5	17.0 ± 4.3
	Transverse direction (TD)		
PLA/PBAT-S0	2210 ± 26	39.7 ± 0.3	3.0 ± 0.2
PLA/PBAT-S1-P1	2390 ± 39	42.0 ± 0.4	8.8 ± 2.6
PLA/PBAT-S1-P2	2770 ± 94	47.2 ± 0.5	11.1 ± 1.8
PLA/PBAT-S1-P3	3010 ± 145	51.7 ± 0.4	13.3 ± 2.2
PLA/PBAT-S1-P4	2670 ± 72	46.7 ± 0.5	12.3 ± 3.1

J   Impact Properties

Table 4.12:   Charpy notched impact strength of all studied materials

Material	Notched impact strength, kJ/m^2
PLA	2.46 ± 0.38
PLA-S1	2.28 ± 0.45
PLA/PBAT-S0	7.50 ± 1.57
PLA/PBAT-S1-P1	7.74 ± 1.14
PLA/PBAT-S1-P2	6.03 ± 0.74
PLA/PBAT-S1-P3	6.17 ± 0.85
PLA/PBAT-S1-P4	6.66 ± 0.70

Curriculum Vitae

Personal Data

Family Name:	Saiprasit
Name:	Praphakorn
Nationality :	Thai

Education

05/2012 – 05/2014:	Master of Science, Polymer Science, The Petroleum and Petrochemical College, Chulalongkorn University, Thailand
06/2008 – 04/2012:	Bachelor of Science, Industrial Chemistry, King Mongkut's Institute of Technology Ladkrabang, Thailand
05/2005 – 03/2008:	High School Diploma (Science - Mathematics), Saraburiwitthayakhom School, Thailand

Professional Experience

10/2021 – present:	Research Associate, Chair of Composite Engineering, Technische Universität Kaiserslautern, Germany
10/2016 – 09/2021:	Wissenschaftliche Hilfskraft (HiWi), Chair of Composite Engineering, Technische Universität Kaiserslautern, Germany
10/2014 – 04/2015:	Research and Development Chemist, Selic Corp Co. Ltd., Thailand
04/2011 – 05/2011:	Laboratory Assistant (Internship), SK Polymer Co. Ltd., Thailand

Scholarship

10/2018 – 09/2021:	OPTIMAS Doctoral Scholarships, Technische Universität Kaiserslautern, Germany
10/2015 – 09/2018:	Research Grants - Doctoral Programmes in Germany, Deutscher Akademischer Austauschdienst (DAAD), Germany